Optical remote sensing technique for the generation of meandering river channel topography and sediment size

Sho Harada

A Thesis
In
The Department
Of
Building, Civil and Environmental Engineering

Presented in Partial Fulfilment of the Requirements
For the Degree of Master of Applied Science in Civil Engineering at
Concordia University

September 2017

© Sho Harada, 2017

CONCORDIA UNIVERSITY

School of Graduate Studies

This is to certify that the thesis prepared

By Sho Harada

Entitled: Optical remote sensing technique for the generation of meandering river channel topography and sediment size

and submitted in partial fulfillment of the requirements for the degree of

Master of Applied Science (Civil Engineering)

complies with the regulations of the University and meets the accepted standards with respect to originality and quality.

Signed by the final Examining Committee:

_____ Chair

Dr. Catherine Mulligan

_____ Examiner

Dr. Ai Nazemi

_____ Examiner

Dr. Marius Paraschivoiu

_____ Supervisor

Dr. Samuel Li

Approved by _____

Dr. Ashutosh Bagchi, Chair of Department or Graduate Program Director

_____ 2017 _____

Dr. Amir Asif, Dean of Faculty

ABSTRACT

Optical remote sensing technique for the generation of meandering river channel topography and sediment size

Sho Harada

Traditional techniques for river cross-section surveys are costly, time-consuming, and difficult to implement. They are also limited by logistical constraints. The practical limitation in the spacing and frequency of survey points restricts ground-based surveys to those of reach scale. This research has demonstrated the potential of generating river topography and sizing bed materials within complex shallow channels, using high-resolution multispectral and stereo images. The demonstration uses a 13-km long reach of meandering, alluvial river (the Goulais River in Ontario). Fluvial remote sensing provides a complimentary alternative to field surveys, in which a detailed synoptic view of the river may be acquired. The presented technique generates a river topography model (RTM) by combining the bathymetry map (the channel-bed to the free surface) and digital elevation map (the free surface and above). The former is generated from the depth-to-brightness ratio that is empirically estimated by correlating available field survey points to the digital numbers of the image. The latter is generated through a photogrammetric analysis of stereo images. A challenge arises in combining the maps when the images used to derive the bathymetry map and the digital elevation map are captured at different times (or at different stages). The difficulty is overcome by applying gradually-varied flow type technique (one-dimensional conservation of mass, energy and momentum) to resolve the discrepancy in the stages per cross section. The resulting RTM is a continuous digital terrain that encompasses the channel-bed, floodplains, and the dry terrain features. Qualitative observations of the RTM indicate a correct placement of geomorphic features, including pool-riffle zones, and point bars. The RTM is used as a model domain for simulations of depth-averaged two-dimensional hydrodynamics in order to estimate the boundary shear stress corresponding to the formative discharge. The median sediment diameter in the riffle zones derived from the simulated boundary shear stress compares well with field observations. The method presented offers a promising complimentary tool for river dynamics analysis and river management.

ACKNOWLEDGEMENT

I would like to thank my supervisor, Dr. Samuel Li, for his guidance, encouragement, and the academic freedom that he had entrusted in me. Your expertise in hydraulics and numerical modelling was invaluable in advancing this research to where it is today.

This research project would not have been possible without the financial support received from the Natural Sciences and Engineering Research Council of Canada through the Discovery Grants held by Dr. Samuel Li.

I would also like to express my appreciation for all the support and guidance given by Dr. Michel Lapointe. I extend my gratitude for sharing the data with me and taking the time to brainstorm and discuss the project. Thank you for sharing your passion for fluvial geomorphology/salmon ecology with me, I learned so much from you.

I would like to thank Fabien Hughe for kindly assisting me in the remote sensing aspect of the project. Your guidance and advice pointed me in the right direct when I was lost.

I would like to thank Daniel Stubbs for his patience in helping me compile the numerical solver codes on the Calcul Quebec supercomputer.

Last but not the least, I would like to thank my family for supporting me through this academic journey.

TABLE OF CONTENTS

LIST OF FIGURES

LIST OF TABLES

LIST OF SYMBOLS

a	Exposure coefficient
A	Cross sectional area
b	Static friction coefficient
c_f	Friction coefficient
d	Depth of penetration
D_s	Particle sediment diameter
DN	Digital number
DN_0	Downwelling digital number at air-water interface
dx	Mesh size
dt	Time step
e	Base of natural logarithm
F^f	Friction force
FS	Free surface elevation
g	Gravitational acceleration
GCI	Grid convergence ratio
h	Flow depth
h_e	Energy loss due to eddies
$\bar{h}$	Average flow depth
I	Light intensity
I_0	Downwelling light intensity at air-water interface
IC	Initial condition
k	Turbulent kinetic energy
L	Reach length
$L_B(\lambda)$	Bottom reflected spectral radiance
$L_C(\lambda)$	Water column spectral radiance
$L_P(\lambda)$	Path spectral radiance
$L_S(\lambda)$	Surface-reflected radiance

$L_T(\lambda)$	Total spectral radiance
n	Manning's roughness
p	Fluid pressure
P	Time-averaged fluid pressure
P_t	Production of turbulent kinetic energy
P_{kv}	Vertical shear due to turbulent kinetic energy
$P_{k\varepsilon}$	Vertical shear due to rate of turbulent dissipation
P	Wetted perimeter
po	Order of convergence
Pr	Richardson extrapolate
Q	Discharge
r	Mesh refinement ratio
R	Hydraulic radius
S	Longitudinal channel slope
T	Top width
u	Velocity
u_*	Friction velocity
$\bar{u}$	Depth-averaged velocity
U	Time-averaged velocity
$\overline{U}$	Time and depth averaged velocity
v	Velocity parallel to boundary surface
$\bar{v}$	Cross sectional average velocity
y	Normal distance from boundary
Y	Total flow depth
y_0	Normal distance from boundary where $v = 0$
z	Bed elevation
α	Energy coefficient
β	Diffuse attenuation coefficient
β_{eff}	Effective diffuse attenuation coefficient

γ	Specific weight of water
δ_{ij}	Kronecker delta
Δh	Stage gap
ε	Rate of turbulent dissipation
θ	Channel angle
κ	Von-Karman constant
υ	Kinematic viscosity
υ_e	Effective viscosity
υ_t	Turbulent viscosity
ρ_s	Density of substrate
ρ_w	Density of water
$\overline{\tau_0}$	Average boundary shear stress
τ_0	Boundary shear stress
$\tau_{bankfull}$	Bankfull flow boundary shear stress
τ_c	Critical shear stress
τ_c^*	Non-dimensional Shields parameter
τ_{ij}	Reynold's tensor
ϕ	Numerical solution

1.0 INTRODUCTION

1.1 Background

In fluvial sciences, there are two broad categories of scale at which rivers are studied. In the regional/watershed scale, studies primarily focus on the incoming and outgoing volume of water and the timing of wave propagation. Such scales tend to sacrifice spatial density of information for greater spatial coverage. In local/hydraulic scales, the primary focus is on the detail hydrodynamics such as flow depth, velocity profiles, turbulence and boundary shear stress, often requiring high spatial density of information in a relatively small spatial extent. What is often missing is the intermediary scale, which covers sufficiently large extent while maintaining the spatial density of information. In this study, the author attempts to achieve this intermediary scale by combining small set of field survey data and remote sensing techniques.

It is often advantageous to have a synoptic view of a river in assessing the nature of the system. In the context of sediment transport and channel morphology, a river must be analyzed from the headwaters to the estuary to characterize the sediment caliber distribution, sediment transport rate/capacity, and the resulting channel aggradation/degradation [1]. From an ecological stand point, the identification of the major determinants of biota composition, i.e. the sedimentary links [2], the various in-stream habitat zones and their longitudinal and lateral connectivity [3] requires a large-scale understanding of the river.

Despite the need for large-scale assessment of rivers, traditional terrestrial survey methods have been limited in spatial extent. Conventional field surveys (i.e. cross-sectional measurements, sonar, and patch sampling) are time consuming, costly, and logistically constrained. In addition, sequential data measurements are prone to error due to the changing environmental variables (imagine making measurements downstream of a peaking dam over a day). Consequently, there is considerable difficulty in achieving field surveys with sufficient spatial extent, spatial density, and frequency of resurvey. In the recent decade, there has been an increasing trend in employing aerial and satellite data to overcome the above-mentioned constraints set by traditional data collection methods.

In this study, a digital representation of the river terrain will be generated at a relatively fine resolution, using remote sensing imagery and small set of field measurements. To demonstrate the use for such product, grain size will be predicted in the riffles of the Goulais River, Ontario, using the digital terrain as an input for a hydrodynamic simulation. The simulated boundary shear

stress corresponding to the bankfull flow will be used to predict the grain size along the river bed. An overview of the study workflow is illustrated in Figure 1.

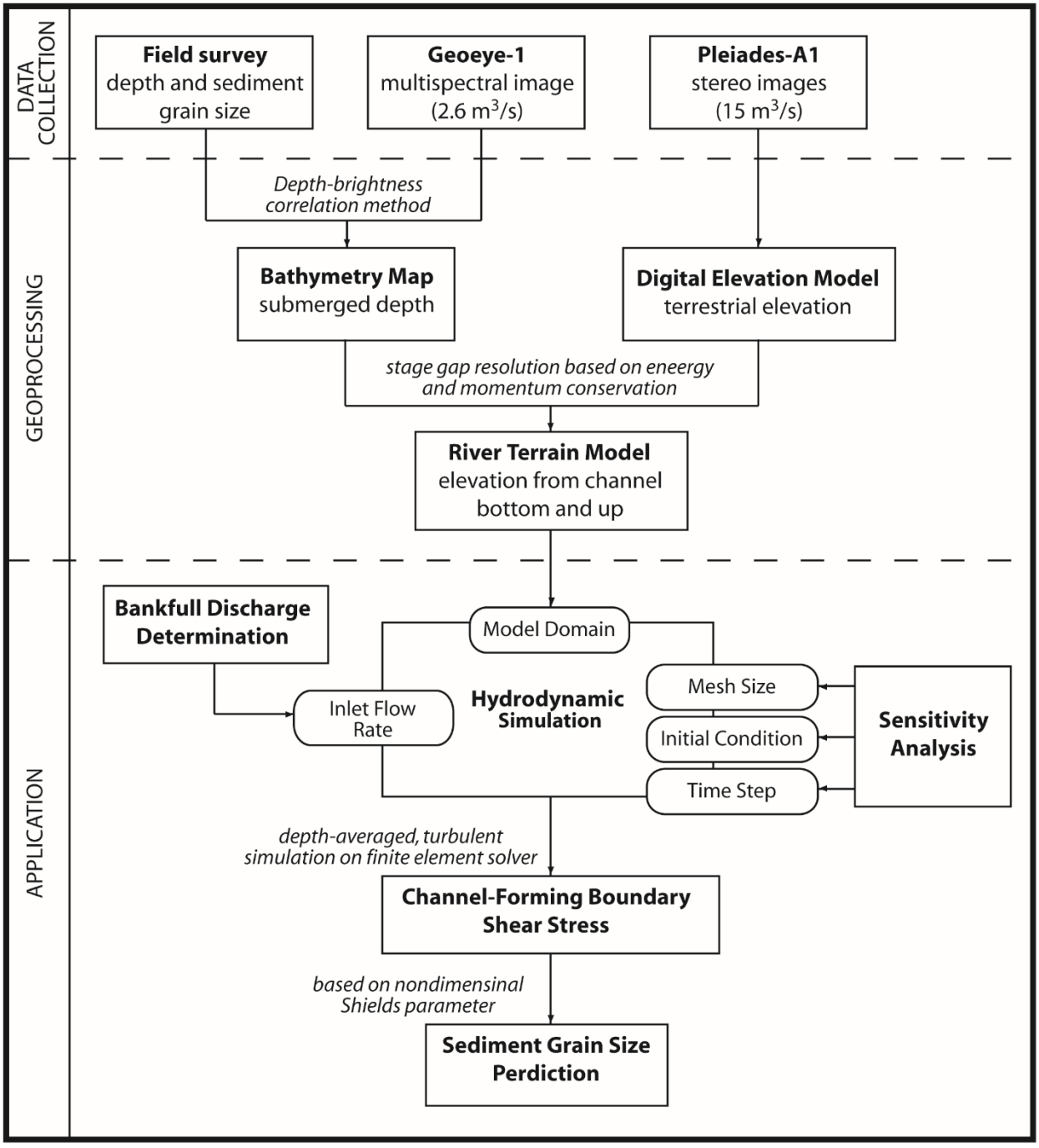

Figure 1 Flowchart of project workflow

This research work was initially inspired by a casual discussion between fluvial geomorphologist and salmon ecologist, Dr. Michel Lapointe [4], from McGill University and the author about a quick and simple way to estimate grain sizes in rivers. Knowledge of the grain size distribution along a river is a valuable information for those assessing salmon habitats and planning habitat restoration since the specie prefers to spawn on oxygen rich riffles with a specific range of grain sizes. They are picky about the spawning grain size because if the sizes are too fine, the eggs suffocate, and if the sizes are too large, the eggs become dislodged. In order to minimize the time spent on site surveying and collecting data, we decided to focus on remote sensing. Since Dr. S. Samuel Li specialises in hydraulic engineering and numerical simulation, we decided to base the grain size prediction on the result of hydrodynamic simulations. Thus, came about the present interdisciplinary collaborative research.

1.2 Scope of research work

The contents of this thesis are organised into five chapters. In the remaining part of this chapter, an outline of the research objectives is given in Section 1.3, and highlights of research contributions are described in Section 1.4. A review of the pertinent literature is provided in Chapter Two. This review covers three major topics: remote sensing, sediment dynamics, and computational fluid dynamics. Discussions begin with background knowledge of remote sensing and sediment dynamics. This is followed by discussions of the research progress in remote sensing bathymetry and grain size predictions. The methodologies developed and used in this research are presented in Chapter Three. Considerations include field survey, geoprocessing, grain size prediction, and hydrodynamic simulation techniques. The results of geoprocessing, hydrodynamics and grain size predictions are presented and discussed in Chapter Four. Conclusions are drawn in Chapter Five.

1.3 Research objectives

The objectives of this study are:

- to retrieve bathymetric information from a multispectral satellite image using small collection of field surveyed calibration depth data (32 locations)

- to generate a river terrain model (RTM), which includes the channel, floodplain, and the surrounding terrestrial topography, by combining the satellite-derived bathymetry map and digital elevation model (DEM)
- to assess the grain size predictive ability in a meandering river based on finite-element hydrodynamic simulation result

1.4 Main contributions

This study has contributed to the innovative growth of river engineering by:

- demonstrating the relative ease of generating a large, high-resolution RTM
- presenting a potential method for producing a RTM from bathymetry map and DEM generated from images captured on different days at different stages. This is achieved by performing a procedure similar to a 1-D backwater calculation.
- presenting comprehensive hydrodynamic simulations of a relatively long reach (13 km) of a meandering river, and exploring the dependence of solutions to various initial conditions, mesh sizes, and time step sizes.

2.0 REVIEW OF LITERATURE

2.1 Remote sensing

Since the launch of LANDSAT 1 in 1972, the first of many earth-observing satellites, availability and accessibility to remote sensing data has improved exponentially due to the number of earth-observing satellites launched and the improvements in data storage and transfer technology [5]. Application of remote sensing in aquatic environments initiated in the coastal sciences with the primary aim to remotely obtain costal bathymetry. In the past two decades, the river science community has adopted techniques developed for the coastal analysis to drive research in fluvial information extraction from remotely sensed data (i.e. bathymetry, substrate types, turbidity, flow characteristics, in-stream habitat, large woody debris, water temperature). A background knowledge of remote sensing and three major techniques for extracting water depth from remotely sensed data are reviewed in the following sections.

2.1.1 What is remote sensing?

Remote sensing technology, initially developed for military intelligence collection, is utilised in many earth science disciplines such as hydrology, ecology, oceanography, atmospheric science, glaciology, and geology. In essence, remote sensing involves detection of information without having to come in direct contact with the object of interest. Remote sensing can be broadly divided into two categories: active and passive remote sensing [5]. Active sensing involves emittance and detection of signals from the carrier (i.e. LiDAR, RADAR), often analyzing the signal return time to estimate altimetry. Active remote sensing is advantageous because of low-frequency signals which are not interfered by atmospheric obstacles (i.e. clouds) and its ability to operate day and night [6]. Passive remote sensing simply detects reflected radiance (most often this is solar reflectance from the surface of the earth). In this study, remote sensing refers to the specific practice of passive remote sensing of earth-reflected solar radiation from a satellite.

2.1.2 Remote sensing resolutions

Remote sensing data may be evaluated using the concepts of resolution. Resolution reflects the way in which continuum information, such as the radiance measured by the sensors, is discretized into discrete and recordable form of information. In remote sensing, there are four resolutions of interest: spatial, temporal, spectral and radiometric [7].

Just as a TV screen or a polaroid photograph is made up of smaller, discrete components (pixels) to represent a continuous image, remote sensing data is stored as regularly gridded cells called rasters. The spatial resolution refers to the size of the individual cells. The higher the spatial resolution, smaller the cell size and more smooth and seamless an image may appear.

Temporal resolution is the frequency of recapture of a specific site of interest. This resolution is dependent on the revisit frequency of the satellite and the frequency of the data collection. For example, sun-synchronous satellites such as the Geoeye-1 returns to the same location every two days, while a geo-stationary satellite such as the Fengyun-2 (China) stays above a specific location on the earth at all times, limiting its temporal resolution by the data transfer speed between the satellite and ground data receiving station.

Spectral resolution refers to the range of wavelength for which the data is collected. A polaroid film has a relatively large spectral resolution since the sensor (the film) is designed to detect radiance in the visible light range (390 nm - 700 mm). Most remote sensing satellites collect data in multiple channels of wavelengths, called bands. For example, the Landsat-7 satellite has 8 bands: blue, green, red, near infrared, shortwave infrared, thermal, shortwave infrared #2 and panchromatic bands. Separating detection in different bands improves object identification since objects in remotely sensed images are identified by examining the spectral reflectance response and matching the response to spectral signature of known objects. For example, when leaves of healthy vegetation reflect solar radiation, there is little reflectance in the red and the blue wavelengths but significant reflectance in the green wavelength, and very high reflectance in the near infrared. In order to accurately represent this continuous radiometric property, one must detect reflectance in red, blue and green bands separately. Consequently, the number of available bands in an image greatly improves the accuracy of representation of spectral response, and thus the object identification ability. Recently, there has been satellites capable of delivering very high-spectral resolution images called hyperspectral images. For example, the Hyperion earth observing instrument is capable of resolving 220 bands at 30 m resolution.

It should be noted that spatial resolution and spectral resolution cannot be increased together [5]. If spatial resolution is increased, the individual sensors (each sensor representing a raster cell in the image) must be reduced in size. This reduces the surface area available for the sensor to detect the radiance. Since there is a threshold value for the sensor to detect radiance, the spectral resolution must be reduced (allow detection of radiance in a wider range of wavelengths)

to compensate for the reduced radiance detection due to reduced surface area. For this reason, spatial resolution and spectral resolution are inversely related.

Radiometric resolution is the way radiance is discretized into digital signals called digital numbers. For a given band, the detected radiance is quantized into discrete bins. This is analogous to filling a bucket (bins) with water (radiance), and once the first bucket is full then the second bucket gets filled, then the third and so on. The radiometric resolution may be considered as the accuracy of the detection in the sense that it determines the smallest interval at which the radiance is detected. Radiometric resolutions are expressed as bit numbers. For example, the Landsat 5 Thematic Mapper has a radiometric resolution of 8-bit ($2^8 = 256$, digital numbers range from 0-256).

2.1.3 Fluvial radiative transfer

This brief introduction to fluvial radiative transfer is based on Cabonneau and Piegay [8] and their book should be referred to for further details. The radiative transfer of solar radiation in fluvial environment is complicated due to the radiometric interactions in the atmosphere and in the river. First definitions of radiometric quantities will be discussed. In passive remote sensing, one is interested in measuring the reflected solar energy to gain information. This energy is termed the radian energy and it has the unit of Joule. The rate of radian energy transferred per unit time is termed the radiant flux and it has the unit of Watt. A related quantity is the rate at which the radian energy is delivered to a surface, or the radiant flux density, termed irradiance and it has a unit of Watt per square meter. In order to account for the directional structure of 3-D light field, the irradiance is normalized by the solid angle (3-D angular measurement) to form radiance. Radiance has a unit of Watt per square meter per steradians, and unlike irradiance, radiance along a beam of light is constant over distance [9]. This means that radiance is independent of distance, geometric effects, illumination, and viewing angles. Effectively, radiance measurements made from difference ranges, different illuminations and angles can be compared. For this reason, radiance is the radiometric property measured by remote sensors. In the case of passive sensors, the radiance is further normalised by a unit wavelength to arrive at the fundamental radiometric quantity called the spectral radiance.

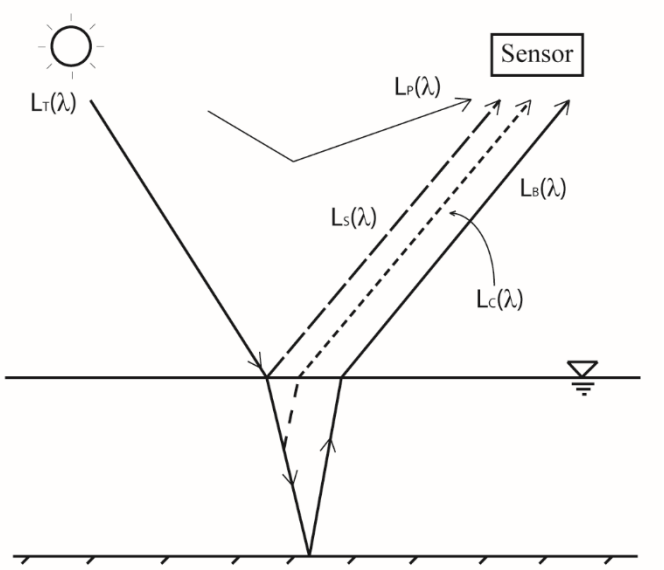

Figure 2. Energy pathways commonly encountered in passive remote sensing

The diverse energy pathways in the fluvial environment can be decomposed into four components (Figure 2) as

$$L_T(\lambda) = L_B(\lambda) + L_C(\lambda) + L_S(\lambda) + L_P(\lambda) \quad (1)$$

where $L_T(\lambda)$ is the total spectral radiance; $L_B(\lambda)$ is the bottom reflected spectral radiance, which consists of photons that have interacted with the stream bed and the portion of the photons that are internally reflected; $L_C(\lambda)$ is the spectral radiance from the water column, which consists of photons that entered the water column but was scattered into the upward hemisphere before reaching the stream bed; $L_S(\lambda)$ is the surface-reflected spectral radiance, which consists of photons that, due to specular reflection at the air-water interface, never reached the water column; $L_P(\lambda)$ is the path spectral radiance, which consists of photons that, due to atmospheric scattering, never reached the air-water interface. To infer bathymetric information from passive remote sensors, one needs to isolate the bottom-reflected radiance. This task is complicated by the complex stochastic nature of scattering photons and require sophisticated radiative transfer models and sufficient understanding of the site (bed material, turbidity, types of suspended sediments, atmospheric condition) to resolve based on fundamental physical laws. Research in remote sensing bathymetric retrieval has established three major techniques to overcome this obstacle, namely: the physically-based technique, correlation based technique and the photogrammetric technique.

2.2. Bathymetric remote sensing

2.2.1 Physically-based technique

Physically based technique is based on physics of optics and employ atmospheric and subaquatic radiative transfer models to resolve the components of detected radiance to isolate the bottom-reflected radiance [10]. Legleiter et al. [11] simulated aquatic radiative transfer using the Hydrolight [12] to determine the effect of water depth, substrate type, suspended sediment concentration and turbulence on the bottom reflectance in the Soda Butt-Pebble Creek confluence, U.S. Legleiter et al. [13] use the optimal band ratio analysis algorithm and radiative transfer model to retrieve bathymetry for the Soda Butt Creek and the Lamar River, WY, USA with a r^2 of 0.79-0.98. The physically based techniques have shown the capacity to be accurate, yet the complexity of the radiative transfer models seems to deter user. In addition, accuracy and precision of depth estimates vary depending on the channel morphology, thus it is not advisable to rely solely on the technique [14].

2.2.2 Correlation technique

Correlation technique employs a regression between the brightness of the image (pixels) and the field depth measurement at the same location to estimate the effective attenuation coefficient of the water column as a function of depth. It is the simplest of the techniques and most commonly used. Gilvear et al. [15] correlated field depth measurement to bins of linearly stretched spectral histogram to create a depth map of the Faith River, AK, USA, with a spatial resolution of 1.3m. Winterbottom and Gilvear [16] used reflectance-measured depth linear function proposed by Lyzenga [17] for the three bands of the Multi Spectral Scanner (band 5, 6, 8) and aerial panchromatic image to map the depth of the River Tummel, Scotland, with a spatial resolution of 2m and 0.8m and r^2 of 0.67 and 0.55 respectively. Fonstad and Marcus [18] developed and demonstrated the Hydraulically Assisted Bathymetry (HAB) model that combined the linear regression of depth-brightness ratio and open channel hydraulics principles to iteratively determine the bathymetry of the Brazos River, TX, USA, with a spatial resolution of 1m and an r^2 of 0.77. Later, Legleiter [19] replaced the Matching Know Discharge (MKD) method used in the HAB model by the Channel Aspect Ratio (CAR) algorithm and demonstrated improvement in the depth mean error from 0.069 m (MKD) to 0.02 m (CAR). Gilvear et al. [20] regressed field measured reflectance, eliminating the dependence of bottom substrate on the bottom reflectance, and image

brightness to obtain a reflectance-depth ratio of the Fourth Estuary, U.K., with spatial resolution of 0.66m and r^2 (of the regression) of 0.81-0.87. Williams et al. [21] combined terrestrial laser scanning, non-metric aerial photography, and surface modelling technique to generate a 0.5 m DEM of the Rees River, New Zealand, using correlation between surveyed depths and blue/red band ratio. Lejot et al. [22] applied the depth-brightness ratio to very high-resolution aerial images obtained by paraglider drone to reconstruct the bathymetry of the Rhone River, France with spatial resolution of 14 cm and r^2 of 0.86. Marcus et al. [23] used 128-band hyperspectral image, in conjunction with principal component analysis, have been used to successfully identify bathymetry and other channel characteristics such as substrate types and woody debris. Legleiter et al. [24] used 288-band hyperspectral image and observed 0.16-0.17 m depth error in the Snake River, WY, USA, while higher depth error of 0.24-0.32 m was found in the Blue/Colorado River, CO, USA, due to higher turbidity.

2.2.3 Photogrammetric technique

Photogrammetric technique is based on stereoscopy and utilizes a pair of stereo images and stereo matching algorithm (identifying identical ground points on the two images) to reconstruct the water depth. Westaway et al. [25] used unsupervised stereo matching algorithm of ERDAS Imaging Software with high-resolution aerial photo scans of the North Ashburton River, New Zealand, to retrieve bathymetry with spatial resolution of 37.1 cm and mean error of 36 cm. Lane et al. [26] combined photogrammetric technique and depth-brightness modelling in the inundated zones to reconstruct the South Saskatchewan River, Canada, with spatial resolution of 4 cm and mean error of -25 cm to 18 cm. Accuracy of through-water photogrammetric depth retrieval have been shown to improve through correlation for refractive index of water [25, 27, 28]. In the recent years, computer vision algorithms such as Structure-from-Motion (SfM) [29, 30] and Multiview-Stereo (MVS) have been incorporated into the geoprocessing workflow, improving the accuracy of the photogrammetric bathymetry. These algorithms have opened up the possibility to using consumer-grade cameras to generate 3D models [31, 32].

Photogrammetric technique requires image resolution in the centimeter ranges, since submerged stereo points can only be matched at a spatial resolution fine enough to resolve the texture of the channel bottom. Consequently, such technique often requires custom low flying

surveys (i.e. planes and drones), which limit the temporal resolution of the site image (availability of historical records) and increase cost.

In this study, depth-brightness correlation technique was used to reconstruct the water depth map from 0.5 m Geoeye-1 multispectral image. The dry land DEM was reconstructed by the vendor using a pair of 0.5 m stereo images from Pleiades-A1. The depth map and the dry land DEM were combined to create a River Terrain Model (RTM), a channel bottom-and-up digital representation of the riverine landscape. As an example of RTM application, digitally reconstructed river was used as a model domain to simulate a bankfull flow in a 2-D hydrodynamic model. Subsequently the simulated bed shear stress was compared against the field sampled sediment caliber in the riffle zone to assess the feasibility of predicting sediment caliber distribution from an image-derived RTM.

2.2.4 Future of bathymetric remote sensing

Surface Water Ocean Topography (SWOT) mission is a continental hydrology and oceanography satellite mission in development, designed for accurate mapping and monitoring of global surface water topography, based on synthetic aperture radar (SAR) interferometry [33].The mission is a joint development among National Aeronautics and Space Administration (U.S.A.), Centre National d'Etudes Spatiales (France) and Canadian Space Agency. The payload is scheduled for launch in 2021 [34]. In this review, the discussion of SWOT mission will be focused solely on the hydrological aspect of the endeavor. The main objectives of the mission are to provide a global inventory of surface water bodies, to measure global storage change in water bodies, and to estimate river discharges up to sub-monthly time scale [33]. Unlike its predecessors, such as altimeters which use Ku-, C-bands and SAR imaging missions that use L-, C- or X-bands, the SWOT mission will carry a Ka-band radar interferometer (KaRIN). The advantages of Ka-band are enhanced spatial resolution and improved estimation of saturated soil surface elevation and snow volume variations [35], while one drawback is the sensitivity to rain rates greater than 3 mm/hr [36]. The KaRIN instrument will have a swath of 140 km with 20 km gap in the middle, the along-track resolution will be 5 m and the cross-track resolution will range between 10-60 m for far range to near range respectively [37]. The orbit will be non-sun synchronous with a repeat period of 21 days [36]. The specifications goals for the mission are reported by Rodriquez [36] and they include altimetric accuracy of less than 10 cm and less than 25 cm for water area greater

than 1 km^2 and greater than 1 km^2 respectively, slope accuracy of 1.7 cm/km for river reaches with water area >1 km^2, and relative error on water areas <15% to name a few. Some of the level-2 (post-processed) products will include vector-format water mask, 1-D vector product of estimated discharge in rivers greater than 50 m and cross sectional map of all observed water bodies. The bathymetry will be derived from varying river/lake stage observed throughout the mission lifetime to contour the topography and it will be updated annually. For this reason, the initial discharge and bathymetry estimates will only be available after one seasonal cycle [36].

In light of the developing SWOT mission, the author advocates that the presented methodologies for combining image-derived bathymetry map and DEM to generate river terrain model will remain as a relevant tool for river scientist even after the lunch of the SWOT payload. First, the spatial accuracy (horizontal) of SWOT-derived water mask and the bathymetric contours will be limited by the spatial resolution of the instrument (5 x 10 m and 5 x 60 m in the far and near). On the other hand the spatial accuracy (horizontal) of the presented method may be controlled based on available images to suit the needs of the users (current limit of airborne imaging is in the centimeter resolution offered by drone imagers). Second, the presented method allows generation of historical river terrain from archival images (i.e. if one requires a bathymetry contour pre 2022). Third, the proposed time-averaging method of SWOT-based bathymetric contour generation may be problematic in ice covered rivers where varying stage information is lost for majority of the year. This difficulty may be overcome by using the method from the present study, so long as there are days in the year where low-stage surface water is visible to the satellite. Finally, the author has no doubt that the SWOT will provide unprecedented volume of information (discharge, water mask, water body slope, bathymetry), at a spatial and temporal scale unmatched by any water related satellite missions. This will most likely propel research in spatial and temporal scales associated in hydrology, climatology and oceanography in the coming years. In particular the author believes that the SWOT data will befit studies in spatial/temporal downscaling of global-scale models, an important step in integrating the local scale effects into global-scale models. That being said, it is questionable whether bathymetry derived from SWOT will be adequate for use in hydraulic engineering where greater detail of channel geometry (spatial resolution) is required.

2.3 Sediment dynamics and meandering river characteristics

The following sections are dedicated to exploration of background theory that relate hydrodynamics to sediment transport, particularly the initiation of sediment entrainment. Literature review of previous works entailing grain size prediction is presented towards the end.

2.3.1 Shear Stress

2.3.1.1 Shear stress in an open channel

In steady uniform flow condition, the total boundary drag in a channel may be expressed as a force balance of down slope component of the weight of block of water and the total drag on the wetted boundary (Figure 3) as

$$A \cdot L \cdot \rho_w \cdot g \cdot \sin(\theta) = P \cdot L \cdot \overline{\tau_0} \quad (2)$$

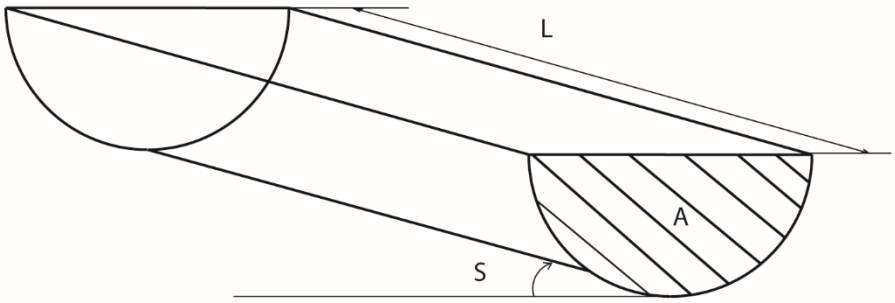

Figure 3. Depth slope product used to estimate the mean boundary shear stress exerted by body of water

where A is the cross sectional area; L is the reach length; ρ_w is the density of water; g is the acceleration sue to gravity; θ is the angle of the channel; $\overline{\tau_0}$ is the average boundary shear stress. For majority of higher order streams, the slope is small enough to approximate $\sin(\theta) \approx S$, and the channel width is much greater than the depth to approximate $R = \frac{A}{P} \approx h$ which simplifies equation 1 to

$$\gamma \cdot \bar{h} \cdot S = \overline{\tau_0} \quad (3)$$

where γ is the specific weight of water; $\bar{h}$ is the mean depth; S is the longitudinal slope of the channel. Equation 2 is often referred to as the depth-slope product. The expression illustrates proportional relationship between mean boundary shear stress and flow depth for flows that are

much wider than its depth ($R \approx \bar{h}$). The relationship between the mean boundary shear stress and cross sectional average velocity may be derived from Manning's law as

$$(4) \qquad \overline{\tau_0} = \frac{\gamma n^2 \bar{v}^2}{R^{1/3}}$$

where n is the Manning's roughness constant; $\bar{v}$ is the cross sectional average velocity. The expression illustrates that the mean boundary shear stress is proportional to square of average velocity and bed roughness.

2.3.1.2 Distribution of shear stress in a river channel

Shear stress distributions in natural river channels are non-uniform and non-symmetric due to the complex and irregular channel shapes. Within a cross section, there may be deep and shallow zones (pool-riffle system). Longitudinally, as flow approaches alluvial bars the flow may transition from deep to shallow. The substrate type and substrate composition may also play a role in the channel form (ie dunes and ripples in sand bed river, pool-riffle systems in gravel bed river, stepped pools in high gradient cobble-boulder reaches).

Qualitatively, one may assess the drag exerted by a flow by looking at the proximity of the isovels to the boundary in a velocity contour plot (Figure 4).

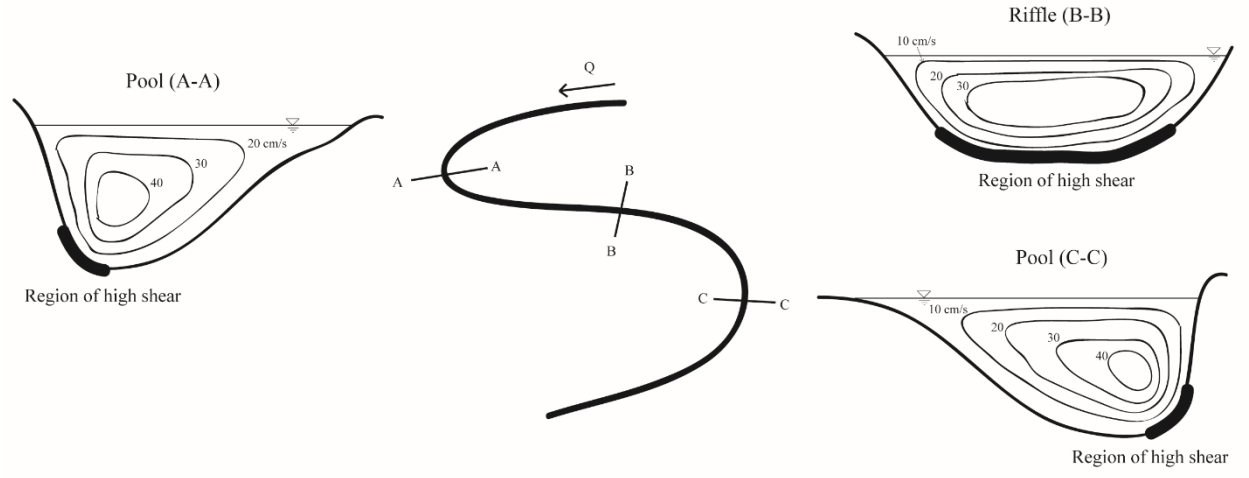

Figure 4. Cross sectional velocity patterns (isovels) and their influence on the boundary shear stress

Understanding the cross sectional velocity distribution will provide a preliminary assessment of the boundary drag distribution. Since the zero-velocity condition applies to the fluid packet right at the boundary the boundary shear stress is expressed as a function of velocity gradient perpendicular to the boundary surface. This increase in velocity along the surface norm is described by the Karman-Prandtl logarithmic law of the wall [38] as

$$(5) \qquad v(y) = \frac{u_*}{\kappa} \ln\left(\frac{y}{y_0}\right)$$

where v is the velocity parallel to the boundary surface; κ is the Von-Karman constant; y is the distance from the boundary; y_0 is the height where the law predicts the velocity to be zero (depends on the local roughness); u_* is the friction velocity. The friction velocity is a velocity scale representative of velocities close to a solid boundary and is defined as

$$(6) \qquad u_* = \sqrt{\frac{\tau_0}{\rho_w}}$$

where τ_0 is the local boundary shear stress. The depth-averaged velocity may be expressed as integral of the logarithmic velocity profile evaluated from the bed to the free surface as

$$(7) \qquad \bar{u} = \frac{1}{Y}\int_o^Y u(y)dy \cong \frac{u_*}{\kappa} \ln\left(\frac{Y}{ey_0}\right)$$

where $\bar{u}$ is the depth-averaged velocity, Y is the free surface depth; e is the base of natural logarithm. It is interesting to note that equation 7 supports the widely accepted practice of approximating average velocity as measurement made at 40% of the total depth (reciprocal of base of natural logarithm is equal to 0.37).

The relationship between average velocity and boundary shear stress based on the logarithmic profile may be expressed by squaring equation 5 and substituting the square of equation 7 to arrive at

$$(8) \qquad \tau_0 = \frac{\bar{u}^2 \rho \kappa^2}{\ln^2\left(\frac{Y}{ey_0}\right)}$$

The drag relationships derived from logarithmic law of the wall (equation 8) and Manning's (equation 4) equation are in agreement; they imply that boundary shear stress increases with;

increasing average velocity ($\bar{u}^2$), decreasing flow depth (Y and R), and increasing bed roughness (y_0 and n).

2.3.2 Initiation of sediment transport

Critical shear stress is defined as the threshold shear stress level required to entrain sediments of given size. The critical shear stress may be analyzed for channel bed comprising of homogeneous or heterogeneous sediments particle diameter.

2.3.2.1 Critical shear stress in homogenous bed

For a homogenous bed (Figure 5), a simple force balance of total drag on the particle and mechanical resistance to dislodgement may be expressed as

$$\tau_c a D_s^{\,2} = (\rho_s - \rho_w) g D_s^{\,3} b \quad (9)$$

where τ_c is the critical shear stress; a is the exposure coefficient; D_s is the sediment particle diameter; ρ_s is the sediment density; b is the static friction coefficient.

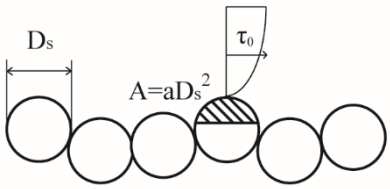

Figure 5 Channel-bed of homogeneous sediments

Simplification of equation (9) yields the following proportional relationship as

$$\tau_c \propto D_s \quad (10)$$

given the coefficients a and b are constant (Figure 6). Shields [39] conducted series of experiments in laboratory flume to show that the ratio of b and a is indeed constant for sediment particle diameter greater than 5 mm as

$$\frac{\tau_c}{(\rho_s - \rho_w) g D_s} = \tau_c^{\,*} = \frac{b}{a} \approx 0.06 \quad (11)$$

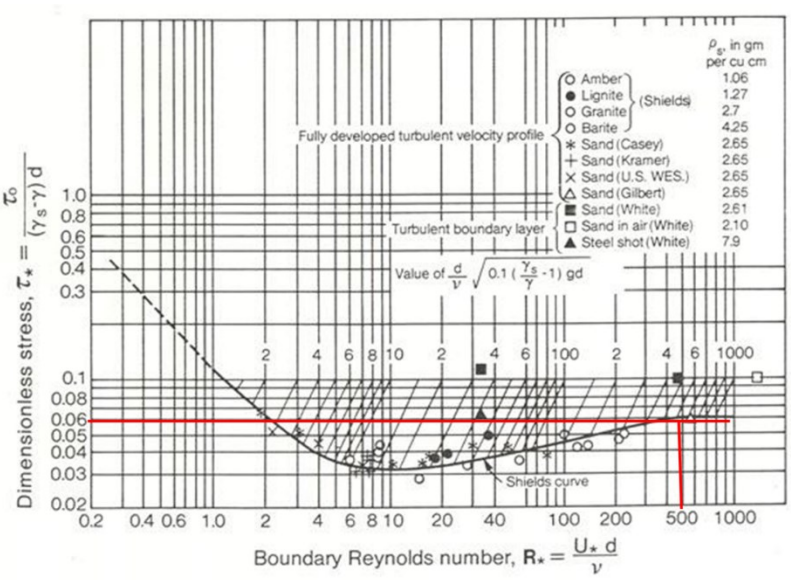

Figure 6. Shields' curve representing the relationship between critical shear stress and the grain size ([*8*])

where τ_c^* is the non-dimensional Shield's parameter. For particles finer than 5 mm, the ratio is increased beyond 0.06 due to the fine particles being embedded in the viscous sub-layer, wherein the particles are less exposed to turbulent drag, requiring greater shear to initiate entrainment. Additionally, as the particle size decreases beyond 5 mm, the electrostatic forces begin to play a significant role in holding the particles together (cohesion). Equation 10, can be rearranged to arrive at

$$\tau_c = 0.06(\rho_s - \rho_w)gD_s \quad (12)$$

This form of the Shield's equation illustrates that for sediment particle diameter greater than 5 mm the boundary shear stress is proportional to sediment particle diameter.

2.3.2.2 Critical shear stress in heterogeneous bed

Heterogeneous bed, such as a gravel-cobble river bed, are comprised of interlocking particles of mixture of sizes (Figure 7). The variability in particle size gives rise to hiding and over exposure of particles due to relative size effects.

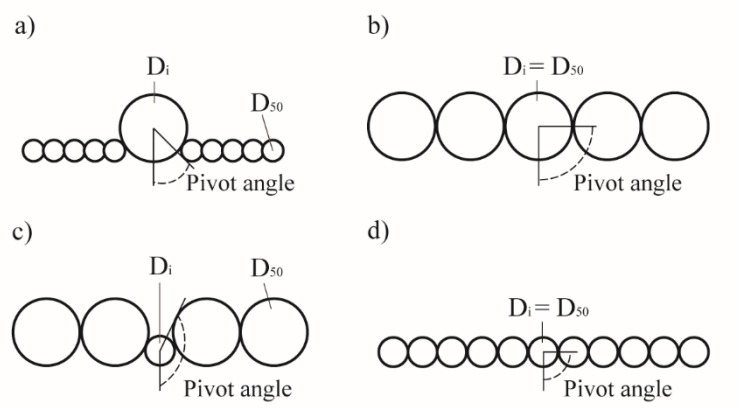

Figure 7. Mechanical advantage/disadvantage of dislodgement due to pivot angles in heterogeneous beds a) large grain Di among smaller D_{50}, b) homogeneous bed of large grains b) small grain Di among larger D_{50}, b) homogeneous bed of small grains

If a particle of size D_i exists among D_{50} that is much smaller, the particle (D_i) will be over-exposed and experience greater stresses compared to if it existed among particles of the same size. In addition, an over exposed particle will have smaller pivot angle compared to if it was surrounded by particles of its own size, resulting in less stress required to dislodge it. Conversely, if particle of size D_i exists among D_{50} that is much larger, the particle (D_i) will be hidden, it will have larger pivot angle, and it will require greater flow stress to dislodge it from the interstice. These effects are collectively termed the size-selective effect (Figure 8) and tend to partially equalize the critical shear stress of mixture of grain sizes on a heterogeneous bed surfaces [40].

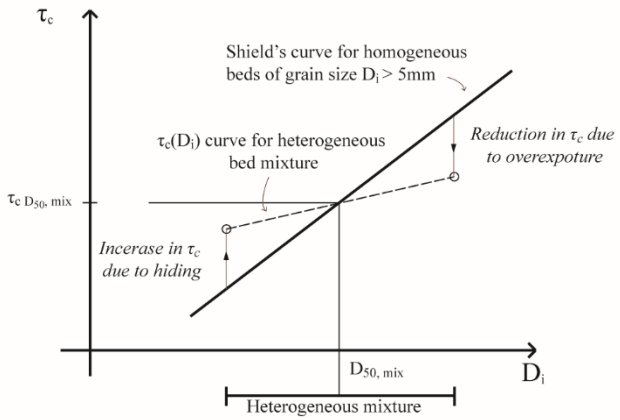

Figure 8. Selective size effect equalizing the critical shear stress in a homogeneous bed

The effect of mixture of sizes on heterogeneous river bed illustrated in Figure 9 show that the same size class D_1 can have higher τ_c when mixed with coarser sediments and lower τ_c when mixed with finer sediments.

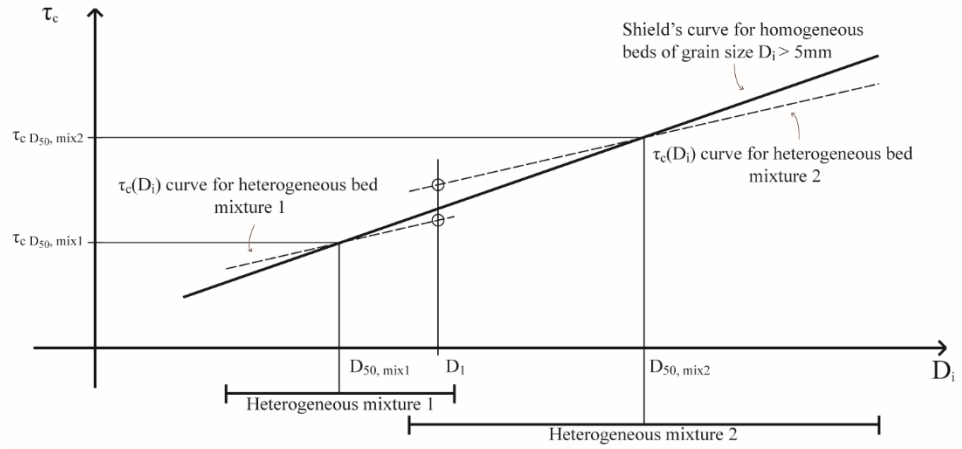

Figure 9. Grain of size, D1, having different critical shear stress due to variable bed compositions

This phenomenon is observed in natural heterogeneous rivers beds and forms a pattern of over exposed coarse sediment and hidden fine sediment called the pavement/armour. Although the extreme grain sizes of the distribution are affected by the over/under exposure effects, the median grain size (D_{50}) are unaffected. Due to the lack of information on the sediment size distribution corresponding to the simulated flow, it is not possible to quantize the size-selective effects in this study. For this reason, the median grain size will be predicted for this study.

2.4 Grain size prediction

Grain size prediction has been a topic of interest for fluvial geomorphologists and ecologists because river bed grain size controls the morphology of the channel and the suitability of spawning habitat for fish species. Majority of the methods explored so far is based on solving the non-dimensional Shield's parameter (equation 10) as

$$(13) \quad \tau_c^* = \frac{\tau_c}{(\rho_s - \rho_w)gD_s} = \frac{\rho_w ghS}{(\rho_s - \rho_w)gD_s}$$

where τ_c is replaced by the depth-slope product ($\tau_c = \rho g h S$) under steady uniform flow assumption; ρ_s is the density of sediment, assumed to equal the density of quarts.

Buffington et al. [41] used DEM and field data collected from gravel-bed, Pacific Northwest mountain rivers of the U.S.A. to show the influence of hydraulic roughness on the bed grain size. They incorporated an empirical power law relationship between the critical Shield's parameter and the critical boundary shear stress based on previously collected field data [42] and extracted slope directly from the DEM. The empirical constants associated with the relationship vary depending on channel morphologies. Unfortunately, their grain size prediction was not validated against field measurement. Gorman et al. [43] used DEMs and hydrologic modeling to estimate channel grain size for a bankfull flow in the streams of Northeast Ohio (R^2=0.45). Their study was based on a previous study by Whiting et al. [44] where power-relationship (R^2=0.82) between median grain size (D_{50}) and bankfull stream power (Ω) was found for 23 grave-bed streams in northern Idaho. Snyder et al. [45] made slight adjustments to Buffington et al.'s [41] method by assuming a constant critical Shield's parameter ($\tau_c^* = 0.04$) and estimating the cross sectional average bankfull flow depth using the Manning's equation. The critical Shield's parameter was determined from a previous study in which painted bed-load particles were monitored in the same streams [46], and a constant Manning's roughness ($n = 0.035$) was assumed based on Barnes' report [47]. Snyder et al. [46] compared the grain size predictive ability of his own, Buffington et al. [41] and Gorman et al.'s [43] methods against field measured grain size in the rivers of the Pleasant, Sheepscot and Narraguagus watershed in ME, U.S.A., and found that the three methods yielded similar predictive ability (70% overall, 80% for grain sizes greater than 16mm). They conclude that all three methods are feasible for predicting grain size at the reach scale. However, they also acknowledge the limitations where (1) the models tend to overestimate grain size in the depositional reaches where the slope transitions from high to low. (2) Local variation in the hydraulic roughness, channel type, sediment supply and land use history may further introduce uncertainty. Most recently, Pfeiffer and Finnegan [48] introduced a new method ($RMSE = 0.025m$) based on Buffington et al.'s [41] method, where the bankfull shear stress is decomposed into its constituents and only fraction of the total shear ($\chi = \frac{\tau_c}{\tau_{bankfull}}$) is considered as the critical boundary shear stress. In addition, a slope-dependent critical Shield's number is

introduced based on Lamb et al.'s [49] data from laboratory flume and natural streams. The equations solved to predict the median grain size by the various authors are listed in Table 1.

Based on this literature review, the grain size prediction methods explored thus far has focused on longitudinal variation but lack the ability to predict in the lateral direction. In this author's opinion, the ability to discern lateral variation in boundary shear stress, and thus the lateral variation in the grain size would be significant and necessary when applying these techniques in meandering rivers. Meandering rivers, depending on their sinuosity, have significant lateral velocity variation as the velocity maxima oscillates from one bend to another. This makes the use of depth-slope product to approximate boundary shear stress a 1-D problem, which is unrealistic. In this study, a finite element numerical solver was used to solve the depth-averaged Navier-Stokes equations to capture the 2-D hydrodynamics of the river flow.

Table 1. Variations of Shield's equation used to predict median sediment diameter by authors presented in the literature review

Buffington et al. (2004)	$D_{50} = \frac{\rho h S}{(\rho_s - \rho_w)\cdot \tau_c^*}$, $\tau_c^* = k(\rho g h S)^m$, $k = const.$, $m = const.$
Gorman et al. (2011)	$D_{50} = 1.88 \cdot (\rho g Q_{bankfull} S)^{0.39}$
Snyder et al. (2012)	$D_{50} = \frac{\rho n^{3/5} Q_{2year}^{3/5} w^{-3/5} S^{7/10}}{(\rho_s - \rho_w)\cdot \tau_c^*}$, $\tau_c^* = 0.04$
Pfeiffer and Finnegan (2016)	$D_{50} = \frac{\chi \rho h S}{(\rho_s - \rho_w)\cdot g \cdot \tau_c^*}$, $\tau_c^* = 0.15 S^{0.25}$

3.0 METHODOLOGIES

3.1 Study site and field survey

The Goulais River (Figure 10) is an eastern tributary of Lake Superior, located 30 km north of Salute Ste. Marie, Ontario. It drains an area of approximately 2000 km^2 into the Goulais Bay. It is an unregulated alluvial river, with well-developed meanders for many kilometers upstream of its mouth. The study site is a 13-km reach situated 3.5 km downstream from the township of Searchmont. Its characteristic pool-riffle system is accompanied by alternating point bars and mid channel bars. There are numerous meander cutoffs evident by clearly identifiable oxbow lakes in the satellite images. The floodplain is densely forested with much of the banks covered by tree canopy. The channel width ranges between 20 m and 100 m and width transitions occur smoothly.

Figure 10. Satellite image of the Goulais River; the river flows from the town of Searchmont (top right), the study site (red box), and drains to the Goulais Bay (bottom left)

A field survey was conducted between 2011 and 2012 by NSERC HydroNet, a national research network comprising of academic scientist/researchers, scientists from Fisheries and Oceans Canada, and hydroelectric companies (Manitoba Hydro and BC Hydro). The research program strives to improve the understanding and develop tools to better assess and mitigate the effects of hydroelectric projects on fish and other ecology. Flow depth and patch sediment size distribution was measured at 35 locations along the river. The patch measured 60 m (L) x 5 m (W) and their long edges were oriented parallel to the mean stream flow (Figure 11). The patch locations were alternated between inner and outer banks successively.

Flow depths were measured at 10 random points within each patch along three lines (3 shore, 4 middle, 3 outer edge). Flow depths of a given patch was estimated as the median of the 10 measurements. Median values were used instead of averages to minimize the influence of anomalous measurements.

Sediment size composition was measured at the same 10 points within the patches. A 50cm quadrat was centered around each of the 10 points in the patches. Width measurement (medium axis) were made on 50 randomly picked sediments per quadrat and classified based on the modified Wolman grain size classification(clay & silt <0.06mm, sand 0.06-2mm, gravel 2-32mm, pebble 32-64mm, cobble 64-250mm, boulders 250-1000mm, metric boulders >1000mm). The sediment size distribution for the 10 quadrats (within a patch) was averaged to estimate the average patch sediment size distribution. D_{50} was graphically estimated as the median of the distribution curb.

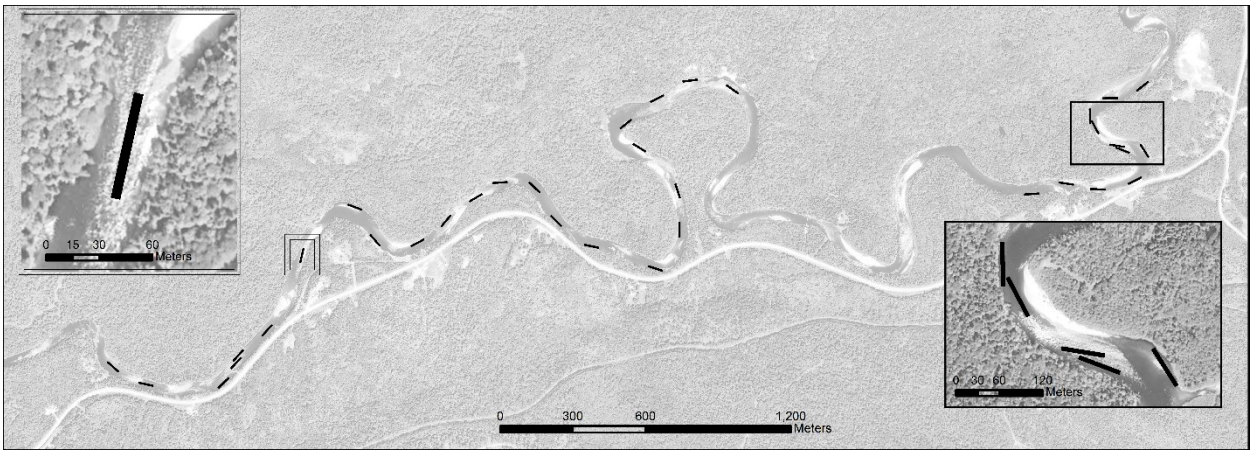

Figure 11. Locations of field survey patches

3.2 Geoprocessing

3.2.2 Bathymetry Retrieval

The bathymetry of the reach was estimated using a 200cm, 4-band (Blue: 450 – 510 nm, Green: 510 – 580 nm, Red: 655 – 690 nm, Near Infrared: 780 – 920 nm) multispectral image captured by Geoeye-1 (Figure 13, Figure 14) on June 04, 2012, at a discharge of 2.6 m^3/s measured at the upstream gauging station (Station #: 02BF002). The image was a new tasking (image captured to order). The timing of the image acquisition was determined to best satisfy the following conditions: to capture the river at low flow depth (shallow enough to detect the bottom reflected radiance),

during noon (maximize solar azimuth to minimize occlusion by specular reflection at the free surface), and during clear sky (minimize occlusion by clouds).

The bathymetry was retrieved from the multispectral image by correlating the field measured flow depth with the image derived reflectance at the corresponding geographical location. The technique is based on the Beer-Lambert law, which describes the exponential attenuation of light through a medium with minimal scattering as a function of penetration depth as

$$(14) \quad I = I_0 e^{-\beta d}$$

where I is the intensity of light at some distance; I_0 is the intensity of light immediately before entering the river; β is the diffuse attenuation coefficient for given wavelength; z is the depth of penetration. When applying equation 14 in remote sensed data, the light intensity is replaced by the digital number as

$$(15) \quad DN = DN_0 e^{-\beta d}$$

where DN is the digital number. Digital number is the discrete unit of measurement which corresponds to the radiance detected by the sensors on the satellites. The radiometric resolution of the Geoeye-1 image is 32-bit (2^{32}). The ratio of equation 14 for red and green band are taken to eliminate the unknown variable, DN_0, as

$$(16) \quad \frac{DN_{red}}{DN_{green}} = \frac{DN_0}{DN_0} \frac{e^{-\beta_{red} d}}{e^{-\beta_{green} d}} = e^{(\beta_{green} - \beta_{red}) d} = e^{\beta_{eff} d}$$

where β_{eff} is the effective diffuse attenuation coefficient defined as the difference between the green and red diffuse attenuation coefficient of water. The natural logarithm of equation 15 is taken to arrive at the linear relationship of depth and the natural log of the digital numbers as

$$(17) \quad \ln\left(\frac{DN_{red}}{DN_{green}}\right) = \beta_{eff} d$$

The effective diffuse attenuation coefficient is empirically estimated by fitting a line on the plot between the field measured flow depths and the natural logarithm of band ratio of the corresponding pixels in the multispectral image (Figure 12). Once the effective diffuse attenuation coefficient is estimated, equation (17) is applied to the rest of the wetted-pixels to derive the flow depth at the time of the image capture.

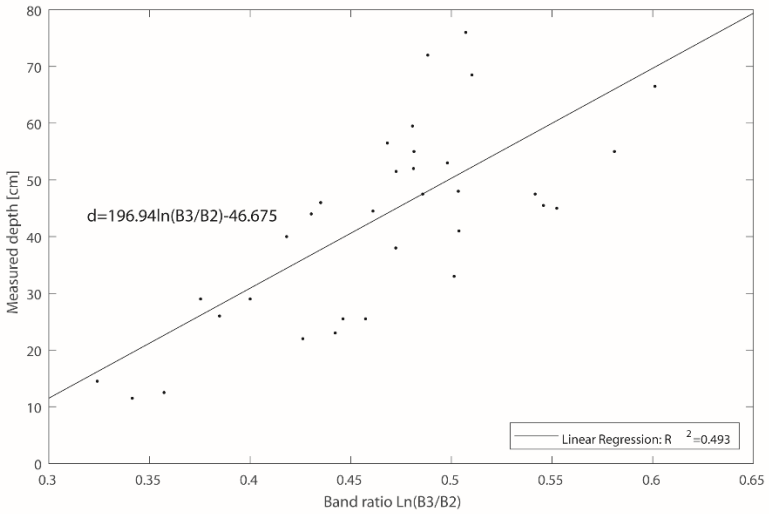

Figure 12. Correlation between natural log of band ratio and measured depth to estimate the effective diffuse attenuation coefficient

The Goulais presented two sources of occlusion which made bathymetry retrieval difficult. The first one is the surface occlusion due to specular reflection (sun glint), particularly in riffles where the unsteady free surface deformation is expected to occur. The second region is the side banks where tree canopies obstructed the view of the border between the water and the land. Pixels affected by the specular reflections are selected by setting a threshold radiance value (since 100% of the downwelling radiance is reflected to upwelling radiance). The identified pixels are removed and interpolated using minimum curvature spline technique. The wet pixels obstructed by the vegetation are manually selected based on the banks that are present downstream or downstream of the canopy. The vegetation pixels are deleted and interpolated as the reflected pixels.

3.2.3 Digital Elevation Model (DEM)

Dry-land topographical information was photogrammetrically estimated using a pair of 200cm, 4-band (Blue: 430 – 550 nm, Green: 490 – 610 nm, Red: 600 – 720 nm, Near Infrared: 750 – 950 nm) multispectral images captured by Pleiades-1A (Figure 13, Figure 15) on June 14, 2016, at a discharge of 15 m^3/s measured at the upstream gauging station (Station #: 02BF002). The images were archival. The images were selected to best match the flow rate of the Geoeye-1 image while minimizing cloud coverage.

The DEM was generated by the vendor using stereo-matching algorithm and principles of stereo parallax to triangulate the distances between the sensor and the features. Further details of the image processing details can be found in the User's Guide [50].

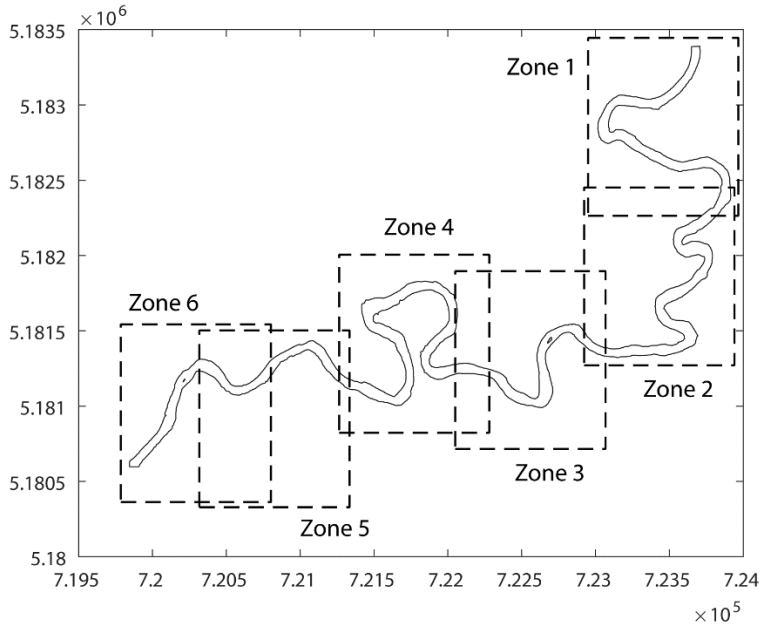

Figure 13. Goulais River zones

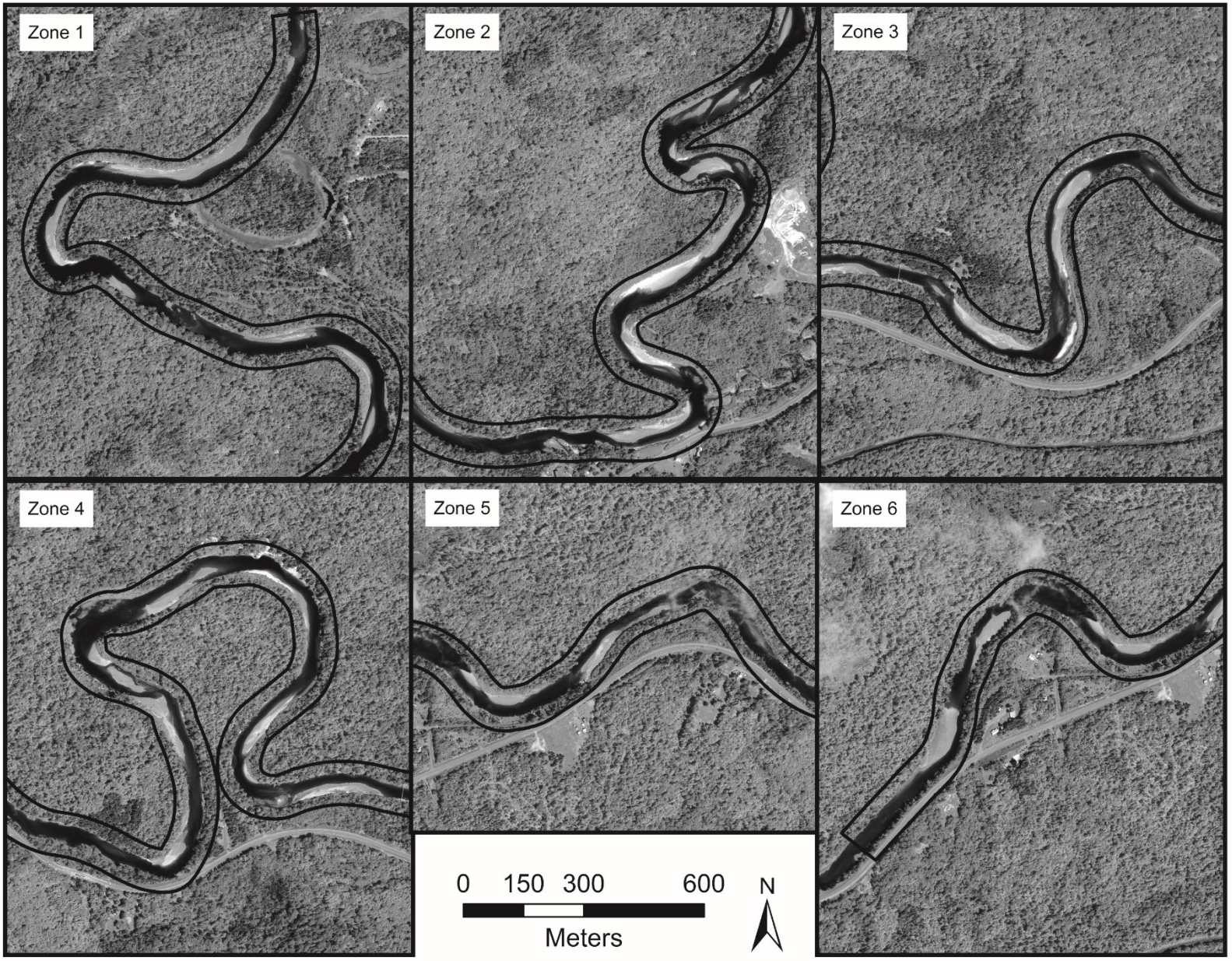

Figure 14. Multiband satellite image of Goulais captured by Geoeye-1 on June 04, 2012

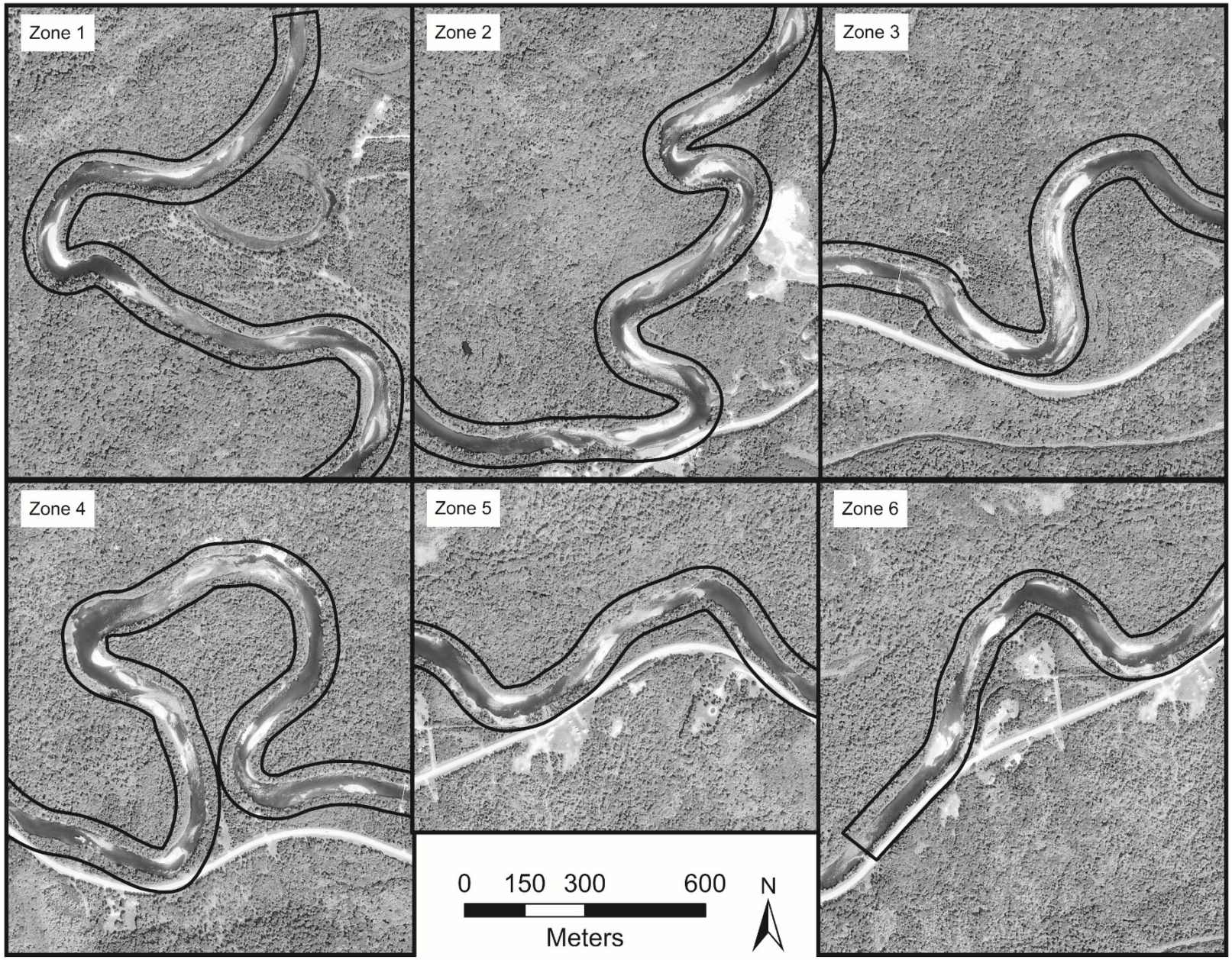

Figure 15. Multiband stereo image of Goulais captured by Peiades-1A on june 14,2016

3.2.4 Combining the Bathymetry Map and the DEM

In order to realize a bed-to-floodplain digital representation of the study site, the wetted-region and dry-region must be combined. It should be noted that the Geoeye-1 image (bathymetry map) had been captured approximately four summers before the Pleiades images (DEM). Nonetheless, it is assumed that minimal channel evolution took place during these four years, based on the assumption that morphological time scale is significantly greater. This assumption was visually verified from 6 publicly available satellite images of the site between 2012 and 2016 (Google Earth). Executing the join, is complicated since the images used to generate the bathymetry map and the DEM were captured on different days with different discharges, leaving a stage gap, Δh, between the top of the bathymetry map and the bottom of the DEM (Figure 16). The 2.6 m^3/s flow of the Geoeye-1 image and the 15 m^3/s flow of Pleiades-A1 images will hence forth be referred to as low and high flow respectively.

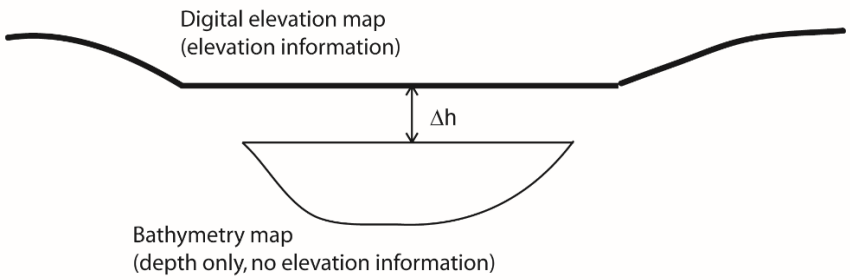

Figure 16. Schematic representation of stage gap

A significant sensitivity of various Δh treatment methods on hydrodynamic simulation results (flow depth, friction velocity) has been identified by a series of sensitivity analyses. Two methods were explored to account for the stage gap: (1) constant Δh and (2) Δh that varies per cross section.

3.2.4.1 Constant stage gap method

The former and the simpler method assigns a constant Δh along the entire reach. The sensitivity of the choice of constant Δh on the numerical solution of bankfull flow was conducted for Δh =0, 0.1, 0.25, 0.4, 0.75 m. Flow depths and friction velocities (function of x and y velocity component) were compared for the 32 sub-patches (approximately 5 nodal values averaged within the 5m x 5m sub-patch). Detail results of the sensitivity analysis are tabulated in Appendix I. The

sub-patch flow depths increased monotonically as the Δh is increased. This is expected as higher values of Δh result in steeper side banks and narrowing of the channel for a given flow depth (Figure 17).

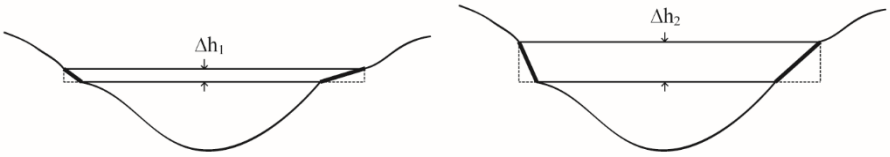

Figure 17. Effect of stage gap on the side slope of the resultant topography

Under the assumptions that 1) the streamwise velocity dominates the lateral velocity, 2) channel is wide enough with $R \approx h$, and 3) flow is normal, a simple ratio of manning equation illustrates that mean velocity decreases as Δh increases as the ratio of Manning's equations, $\frac{v_{\Delta h_1}}{v_{\Delta h_2}} = \frac{n_{\Delta h_2}}{n_{\Delta h_1}} \left(\frac{h_{\Delta h_1}}{h_{\Delta h_2}} \right)^{2/3} \left(\frac{S_{\Delta h_1}}{S_{\Delta h_2}} \right)^{1/2}$ simplifies to $\frac{v_{\Delta h_1}}{v_{\Delta h_2}} = \left(\frac{h_{\Delta h_1}}{h_{\Delta h_2}} \right)^{2/3}$ and show that $\frac{v_{\Delta h_1}}{v_{\Delta h_2}} > 1$, where constant stage gaps $\Delta h_1 < \Delta h_2$. Since the friction velocity is a function of x and y velocity components (later in equation (38)), it should decrease as Δh is increased. Nonetheless the sensitivity analysis show that the sub-patch friction velocity does not necessarily decrease monotonically as Δh is increased. In response to increase in Δh, 19/32 sub-patches show monotonic decrease in friction velocity, 3/32 sub-patches show monotonic increase in friction velocity, and 10/32 sub-patches show nonmonotonic variation of friction velocity. The mixed response of the friction velocity is theorized as a result of the simulated flow artificially spilling over to the floodplain in certain reaches, thereby decreasing the main channel velocity and the friction velocity. In order to determine whether the floodplain flow is realistic required knowledge of the site and the morphology of the river. Based on these results and the site-specific nature of the method, the constant Δh method was deemed unfavorable as a general stage gap resolution technique.

3.2.4.2 Variable stage gap method

The variable Δh method uses 1D continuity, energy, and ratio of Manning's equations for low and high flows to iteratively solve for the Δh per cross section.

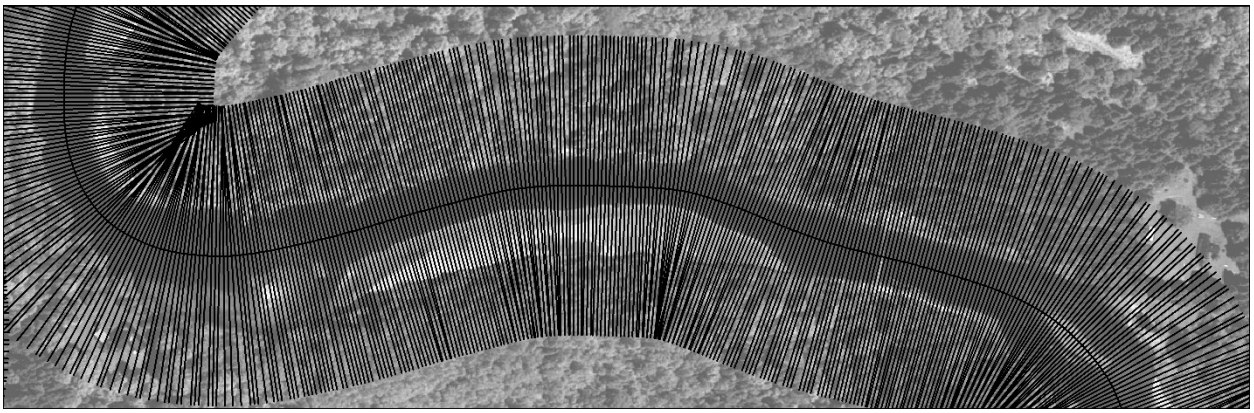

Figure 18. Transects generated perpendicular to centerline

Cross sections are constructed at 2 m interval by generating perpendicular lines (Figure 18) to the manually digitized centerline.The ratio is expressed as

$$(18)\quad \frac{Q_L}{Q_H} = \left(\frac{n_H}{n_L}\right)\left(\frac{A_L^i}{A_H^i}\right)^{5/3}\left(\frac{P_H^i}{P_L^i}\right)^{2/3}\left(\frac{S_L^i}{S_H^i}\right)^{1/2}$$

where subscripts H and L denote high and low flow respectively; superscript i denotes the cross section number counted starting from the upper most cross section downstream; Q is the discharge; P is the wetted perimeter.

A constant Manning's roughness factor of 0.425 was adopted for the entire reach, based on Chow's [51] recommendation for a natural river with top width greater than 30ft. The Manning's roughness was assumed to remain constant with change in stage. Although it has been demonstrated by Chow [51] that the roughness decreases with increasing stage due to less effective resistance provided by the side banks, it is assumed that the Δh is small enough that the change in the roughness is insignificant in this study.

The cross-sectional geometry for low flow (A_L^i and P_L^i) can be computed by discretizing the transect by the edge length of the pixel (200 cm) and linearly interpolating between the points to arrive at finite number of simplified geometries. The cross-sectional geometry for the high flow is decomposed and expressed as the sum of cross sectional geometry for low flow and the remainder as

$$(19)\quad A_H^i = A_L^i + \Delta A^i$$

$$(20)\quad P_H^i = P_L^i + \Delta P^i$$

It was assumed that the missing cross-sectional area, ΔA, could be represented by a trapezoid (Figure 17). Under such assumption, the missing cross-sectional area and missing cross sectional wetted perimeter, ΔP, may be expressed as a function of top widths, and stage gap as

$$(21)\quad \Delta A^i = f(T_L^i, T_H^i, \Delta h^i) = \frac{(T_L^i + T_H^i)\Delta h^i}{2}$$

$$(22)\quad \Delta P^i = f(\Delta T_{right}^i, \Delta T_{left}^i, \Delta h^i) = \sqrt{\left(\Delta T_{right}^i\right)^2 + \left(\Delta h^i\right)^2} + \sqrt{\left(\Delta T_{left}^i\right)^2 + \left(\Delta h\right)^{i\,2}}$$

where T is the top width; ΔT is the difference between the top widths at low and high flow at the respective sides of the bank if one were to face in the downstream direction. The energy slope of the low flow was estimated by applying the energy equation between the cross sections (Figure 19) as

$$(23)\quad h_L^i + \alpha^i \frac{\left(Q_L\right)^2}{2g\left(A_L^i\right)^2} + z^i - \frac{1}{2}\Delta x S_L^i + h_e = h_L^{i+1} + \alpha^{i+1} \frac{\left(Q_L\right)^2}{2g\left(A_L^{i+1}\right)^2} + z^{i+1} + \frac{1}{2}\Delta x S_L^{i+1}$$

where α is the energy coefficient to account for the non-uniform cross-sectional velocity distribution; z is the bed elevation; h_e is the eddy loss associated with energy loss at the exit.

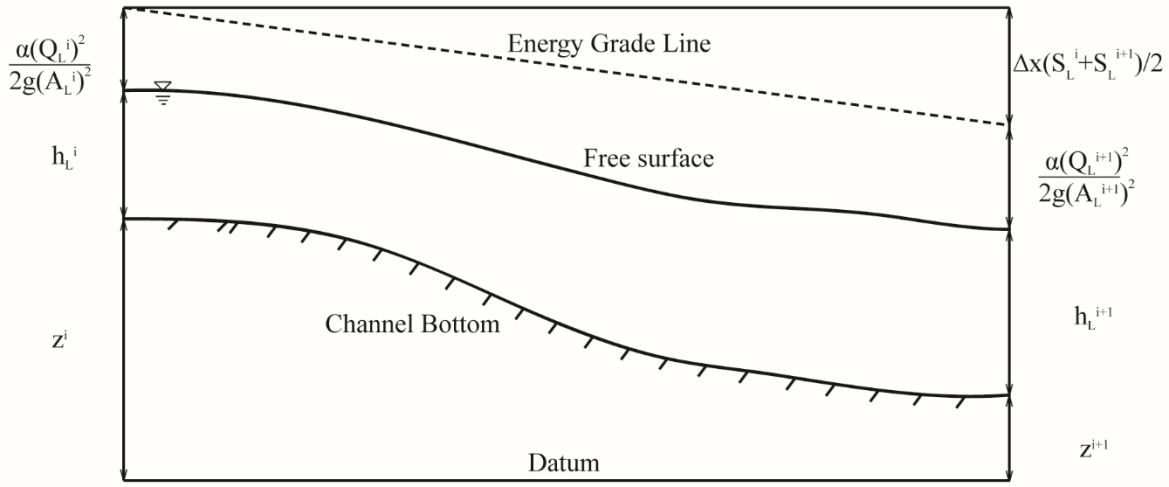

Figure 19. Graphical representation of the energy conservation equation (equation 23)

To simplify the problem, it is assumed that the energy coefficient is equal to unity for all cross sections and the eddy loss was neglected because the change in successive cross-sectional area was small. Since elevation information is absent in the bathymetry map, the bed elevation was replaced by an expression as a function of Δh as

$$z^i = FS^i - h_L^i - \Delta h^i \quad (24)$$

where FS is the free surface elevation of the high flow (DEM, Figure 20).

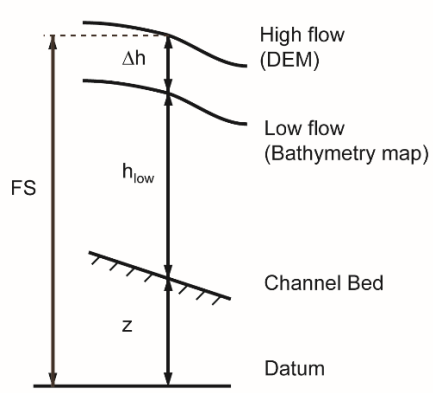

Figure 20. Relationship between DEM free surface elevation (FS), stage gap (Δh), flow flow depth (hlow), and bed elevation (z)

The final form of energy equation as a function of upstream and downstream energy slope and stage gap is

$$FS^i + \frac{\left(Q_L\right)^2}{2g\left(A_L^i\right)^2} - \Delta h^i - \frac{1}{2}\Delta x S_L^i = FS^{i+1} + \frac{\left(Q_L\right)^2}{2g\left(A_L^{i+1}\right)^2} - \Delta h^{i+1} + \frac{1}{2}\Delta x S_L^{i+1} \quad (25)$$

The energy equation is solved from downstream towards upstream since the flow is well in the subcritical regime. The lower most cross section is located in a straight section (Figure 21) of the reach where the assumption of normal flow may be justified.

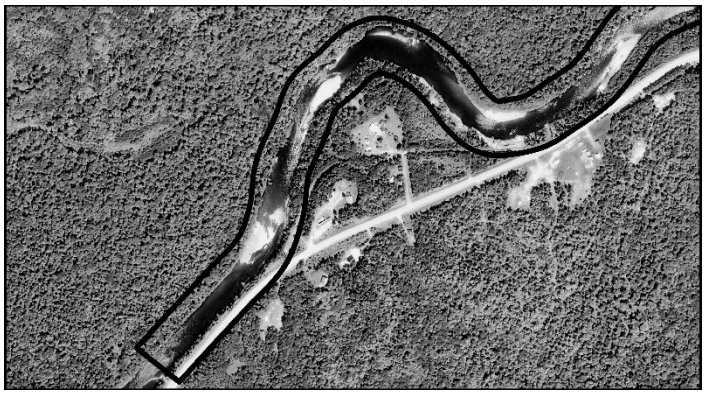

Figure 21. Location of the outlet

Under such assumption, the downstream slope (simply the slope of the channel) and stage gap (using Manning's equation with the slope of channel) can be computed and used as boundary condition to start the backwater calculation. Equations (18) and (25) are solved simultaneously and iteratively to yield stage gaps that vary from one cross section to another.

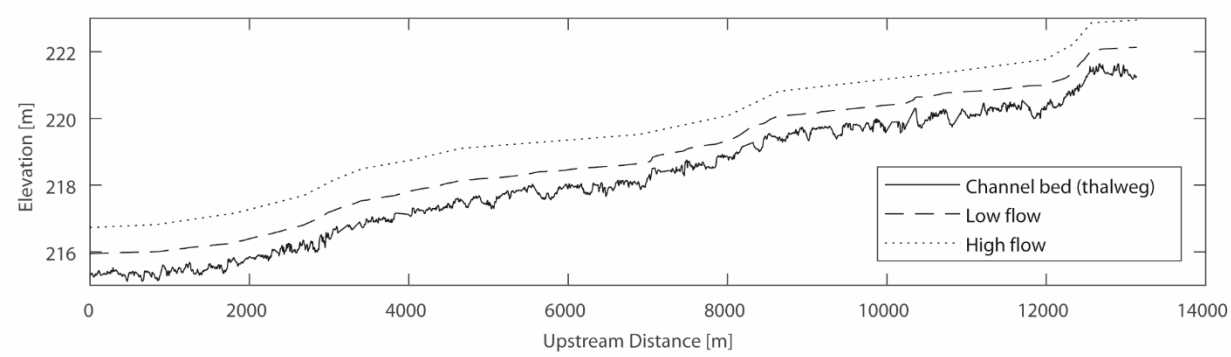

Figure 22. Long profile of low flow and high flow resolved using variable stage map method

The cross-sectional bathymetry is offset appropriately with the stage gap and combined with the DEM to provide elevation information in the wetted region (Figure 22). The elevation information in the void between the outer bank of the low flow and high flow is interpolated using a 2D minimum curvature spline technique. The resultant river topography map will be referred to as the River Terrain Model (RTM).

3.2.5 Delineation of bankfull discharge and bankfull depth

The concept of bankfull discharge, also known as formative discharge, is often used in fluvial geomorphology to refer to the dominant discharge influencing sediment transport, surface grain size, and channel morphology in many alluvial rivers [52, 53, 54, 55].The bankfull discharge is a channel forming discharge, often considered of having a recurrence interval of 1-2 years [56, 57, 58]. There are variety of definitions related to "bankfull", here we define bankfull as the discharge at which the flow just spills over the side banks.

The bankfull discharge was estimated through ensemble of statistical and graphical methods. Frequency analysis was conducted on 47-years of peak annual discharge data obtained from the upstream gauging station (Figure 23, station code: 02BF002). Annual peak discharge with a 1.6-year recurrence was chosen as a suitable representation of the bankfull discharge. Log-

Pearson Type III distribution was used as recommended by the Flood Flow Frequency Guideline [59]. The bankfull discharge was estimated to be 134 m^3/s.

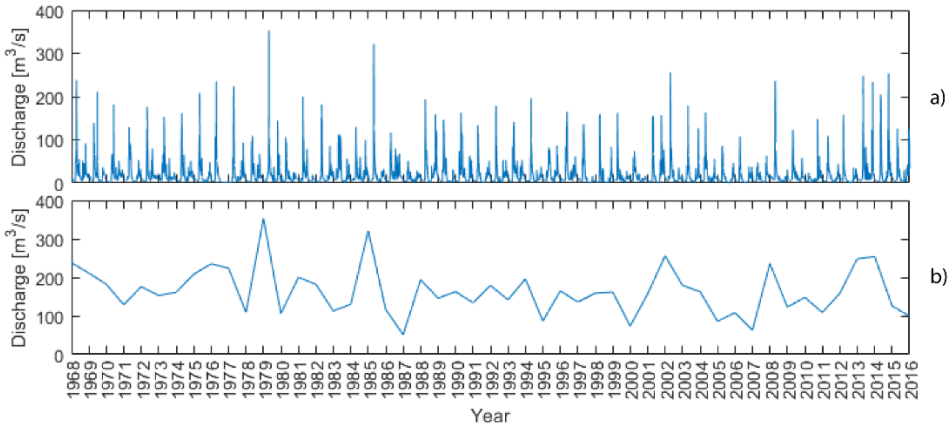

Figure 23. Hydrographs recorded at the upstream gauging stations a) daily discharge measurement, b) annual extreme discharge

Subsequently, 9 plots of width-depth ratio against stage was constructed for cross sections close to the downstream boundary.

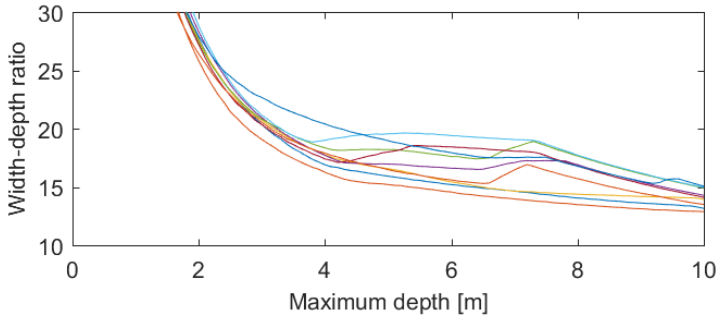

Figure 24. Width-depth ratio v.s. flow depth measured from thalweg for cross sections located within 500m of the outlet

The stages of multiple cross sections corresponding to the minimum slope of the width-depth ratio (Figure 24) was averaged to determine the bankfull stage. Assuming normal flow, the bankfull discharge was estimated as 70 m^3/s using the Manning's equation. The average of the two methods yielded a bankfull discharge of 102 m^3/s.

3.3 Sediment Transport: Relationship between shear stress and median sediment size

The computed bed shear stress is related to sediment particle diameter based on critical entrainment shear stress for an incipient motion problem. Accordingly, the principles and techniques for rigid-boundary hydraulics are respected. Assuming a homogeneous patch, Shields' experiments suggested a dimensionless Shields parameter that is a function of the critical shear stress, and geometrical properties (equation (11)). Equation (11) becomes applicable to heterogeneous bed when grain size in is replaced by median grain size (D_{50}) to eliminate size selective effects. The critical boundary shear stress is assumed to equal the boundary shear stress at bankfull flow (variable to be numerically modeled). For grain size greater than 5mm, the critical Shield's parameter is assumed to have a constant value of 0.06 based on Shield's experiments [39]. The critical Shield's parameter values are read off the Shields' curve [39] for grain size smaller than 5 mm. The density of sediments is assumed to equal the density of quartz (2560 kg/m^3). The grain size is predicted by solving the following modified Shield's equation as

$$(26) \quad D_{50} = \frac{\tau_{bankfull}}{(\rho_s - \rho_w)\tau_c^*}$$

where $\tau_{bankfull}$ is the boundary shear stress corresponding to a bankfull flow.

3.4 Hydrodynamic Simulation

3.4.1 Governing equations

The present study deals with 2D depth-averaged open channel flow. The model equations are solved with finite element solver, Open-TELEMAC 2D, developed by the Research and Development Directorate of the French Electricity Board (EDF-R&D). A brief overview of the governing equations solved in the suite is described in the following section. A more complete and comprehensive documentation on the solver may be found in Hervouet's book [60].

The spatial direction indices i and j present in the expressions hereafter are subject to Einstein's summation convention, where subscript repeated twice in any product or quotient of terms is summed over the entire range of values of that subscript.

The depth-averaged model equations are based on the principles of continuity and momentum for an incompressible fluid as

$$(27)\quad \frac{\partial u_i}{\partial x_j} = 0$$

$$(28)\quad \frac{\partial u_i}{\partial t} + u_j \frac{\partial u_i}{\partial x_j} = -\frac{1}{\rho}\frac{\partial p}{\partial x_i} + \frac{\partial}{\partial x_j}\left[\upsilon\left(\frac{\partial u_i}{\partial x_j} + \frac{\partial u_j}{\partial x_i}\right)\right] + F_i^f + g_i$$

where spatial direction indices i and j vary between 1 and 2, denoting the longitudinal (east to west) and latitudinal (south to north) components of the projected coordinates respectively; u is the velocity; p is the fluid pressure, υ is the fluid kinematic viscosity; F^f is the friction force. Turbulence is taken into account by applying Reynolds decomposition and averaging to the variables in the continuity (equation (29)) and momentum (equation 30)) equations as

$$(29)\quad \frac{\partial U_i}{\partial x_i} = 0$$

$$(30)\quad \frac{\partial U_i}{\partial t} + U_j \frac{\partial U_i}{\partial x_j} = -\frac{1}{\rho}\frac{\partial \mathrm{P}}{\partial x_i} + \frac{\partial}{\partial x_j}\left[\upsilon_e\left(\frac{\partial U_i}{\partial x_j} + \frac{\partial U_j}{\partial x_i}\right)\right] - \frac{\partial \tau_{ij}}{\partial x_j} + F_i^f + g_i$$

$$(31)\quad \upsilon_e = \upsilon + \upsilon_t$$

where U is the time-averaged velocity component, P is the time-averaged pressure, υ_e is the effective viscosity, τ_{ij} is the Reynold's tensor resulting from interaction of i and j component of velocity fluctuations; υ_t is the turbulent viscosity.

The Reynold's tensor introduces three additional terms (in 2D) which are modelled collectively assuming isometric turbulence. The system of equations is closed based on the Bossinesq hypothesis which expresses Reynolds tensor as a function of mean deformation rate as

$$(32)\quad \tau_{ij} = \upsilon_t\left(\frac{\partial \overline{U_i}}{\partial x_j} + \frac{\partial \overline{U_j}}{\partial x_i}\right) - \frac{2}{3}k\delta_{ij}$$

where k is the turbulent kinetic energy; δ_{ij} is the Kronecker delta, with $\delta_{ij} = 1$ when $i = j$ and $\delta_{ij} = 0$ when $i \neq j$.

Turbulent viscosity is expressed as a function of turbulent kinetic energy and rate of turbulent dissipation according to Kolmogorov as

$$(33)\quad \upsilon_t = c_\mu \frac{k^2}{\varepsilon}$$

where ε is the rate of turbulent dissipation; the constant $c_\mu = 0.09$. The governing equations for the turbulent kinetic energy and rate of dissipation are expressed as

$$(34)\quad \frac{\partial k}{dt} + \overline{U_j}\frac{\partial k}{\partial x_j} = \frac{1}{h}\frac{\partial}{\partial x_j}(h\frac{\upsilon_t}{\sigma_k}\frac{\partial k}{\partial x_j}) + P_t - \varepsilon + P_{kv}\mathrm{k}$$

$$(35)\quad \frac{\partial \varepsilon}{dt} + \overline{U_j}\frac{\partial \varepsilon}{\partial x_j} = \frac{1}{h}\frac{\partial}{\partial x_j}(h\frac{\upsilon_t}{\sigma_\varepsilon}\frac{\partial \varepsilon}{\partial x_j}\varepsilon) - \frac{\varepsilon}{k}\left(c_{1\varepsilon}P - c_{2\varepsilon}\varepsilon\right) + P_{\varepsilon v}$$

where ε is the rate of dissipation; constants $\sigma_k = 1.0$, $\sigma_\varepsilon = 1.3$, $c_{1\varepsilon} = 1.44$, $c_{2\varepsilon} = 1.92$. The first terms on the right hand sides of equation (34) and (35) are the diffusion terms. The production term, which, by definition, is always positive, is expressed as a product of mean deformation rate and mean strain rate as

$$(36)\quad P_t = \upsilon_t\left(\frac{\partial \overline{U_i}}{\partial x_j} + \frac{\partial \overline{U_j}}{\partial x_i}\right)\frac{\partial \overline{U_i}}{\partial x_j}$$

where P_t is the production of turbulent kinetic energy. The remaining terms on the right hand side of equation (34) and (35) are the vertical shear terms resulting from turbulent fluctuations expressed as a function of friction velocity as

$$(37)\quad P_{kv} = \frac{1}{\sqrt{c_f}}\frac{u_0^3}{h}$$

$$(38)\quad P_{k\varepsilon} = 3.6\frac{c_{2\varepsilon}\sqrt{c_\mu}}{c_f^{3/4}}\frac{u_0^4}{h^2}$$

$$(39)\quad u_* = \sqrt{\frac{\tau_0}{\rho}} = c_f\sqrt{\overline{U_1}^2 + \overline{U_2}^2}$$

where P_{kv} is the vertical shear term for the turbulent kinetic energy; $P_{k\varepsilon}$ is the vertical shear term for the rate of dissipation; c_f is the friction coefficient; τ_b is the bed shear stress. The friction coefficient is estimated from Manning equation as

$$(40)\quad c_f = \frac{gn^2}{h^{1/3}}$$

where $n = 0.0425$ is the Manning roughness constant. The Reynolds averaged continuity (equation (29)) and momentum (equation (30)) equations are spatially averaged by integrating over the flow depth as

$$(41)\quad \frac{\partial h}{\partial t} + \overline{U_1}\frac{\partial h}{\partial x_j} + h\frac{\partial \overline{U_1}}{\partial x_j} = 0$$

$$(42)\quad \frac{\partial \overline{U_i}}{\partial t} + \overline{U_j}\frac{\partial \overline{U_i}}{\partial x_j} = -g\frac{\partial z}{\partial x_i} + \frac{1}{h}\frac{\partial}{\partial x_j}(h\upsilon_e\frac{\partial \overline{U_i}}{\partial x_j}) + F_i^f$$

$$(43)\quad F_i^f = -\frac{U_i}{\cos(\alpha)}\frac{gn^2}{h^{4/3}}\sqrt{\overline{U_1}^2 + \overline{U_2}^2}$$

where $\overline{U}$ is the time and depth averaged velocity component; z is the bed elevation; $\frac{1}{\cos(\alpha)}$ is the norm of the vector normal to the steepest point at the bottom.

3.4.2 Sensitivity analysis

Solutions of systems of non-linear equations such as the Navier-Stokes equations are intrinsically sensitive to initial conditions and spatial and temporal discretization. For this numerical study, solution sensitivity to mesh size (3 level), time step size (3 level) and initial conditions (Figure 25, 3 types) were examined. The edge length of triangular mesh (dx) was successively refined by half, resulting in 2 m, 1 m, and 0.5 m meshes, each producing element count of 562067, 2248243 and 8992938 respectively. Details of the mesh statistics can be found in Appendix II. The time step (dt) examined were 0.25, 0.1, 0.05 seconds. The initial conditions (IC) considered were: constant water surface elevation, constant water depth, and 1D flow depth. These initial conditions are the most common types of initial conditions found in hydrodynamic simulation suites such as HEC-RAS, Open-TELEMAC, Delft-3D. The 1D flow depth was pre-computed using standard step method with normal flow downstream boundary condition in HEC-RAS.

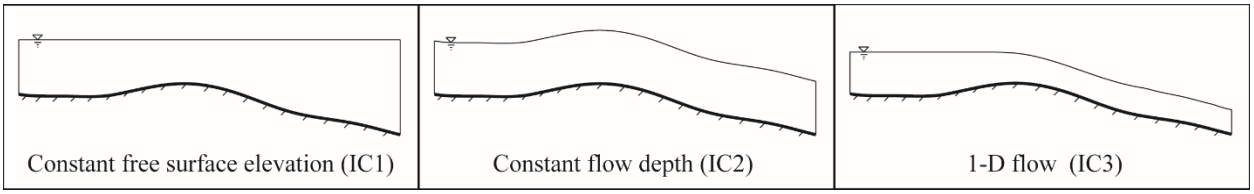

Figure 25. Three types of initial conditions

Flow depth and friction velocity was chosen as the two solution variables for comparison. Friction velocity was chosen since it is the parameter through which boundary shear stress is estimated. In addition, friction velocity is a good overall representation of the hydrodynamics since it is a function of x and y velocity components (refer to equation (39)). For each run flow depths and friction velocities were sampled in 5 m x 5 m sub-patches (Figure 26), which coincided with the centroids and their edges parallel with the 32 field measurement patches described in section 2.1. Nodal values (average of 5 nodes per sub-patch) were averaged to represent the sub-patch flow depths and friction velocities.

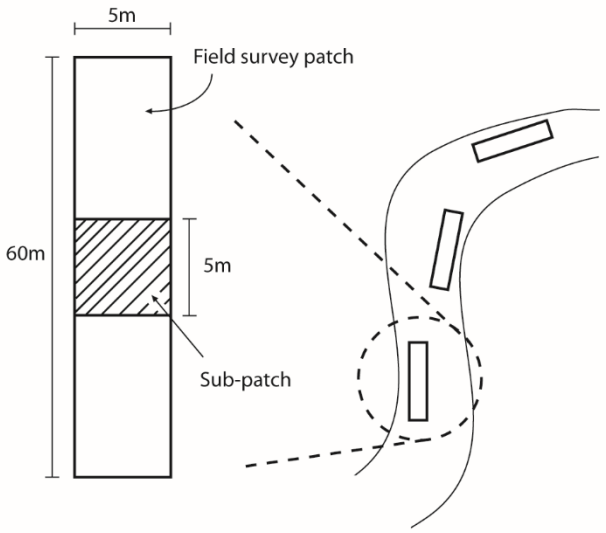

Figure 26. Example of a sub-patch configuration

3.4.2.1 Sensitivity of Initial Condition

The sensitivity of initial conditions was tested by fixing the mesh size and time step while varying the initial conditions. Two sets of runs were conducted, first set with dx=2m, dt=0.25s, second set with dx=1m, dt=0.25s. The detail results of the runs are tabulated in Appendix III. Looking at the flow depths for both sets, the standard deviations within sub-patches do not exceed orders of 1/10000 m. This is a value of standard deviation is equivalent to 1/100 of a percent of the mean sub-patch flow value. The friction velocities indicate comparable results. Looking at the friction velocities for both sets, the standard deviations within sub-patch do not exceed orders of 1/10000 m/s. This is equivalent to 1/10 of a percent of the mean sub-patch friction velocity. The results of the initial condition sensitivity clearly demonstrate that the numerical solution is independent of

the initial conditions. One of the major reason for the said independence is due to the long simulation time (10 hr), which diminishes the effect of initial condition on the convergent solution. The constant water surface elevation was chosen as the favourable initial condition solely based on the ease of application and minimal wall-clock time requirement to complete the 10 hr simulation.

3.4.2.2 Sensitivity of Spatial Discretization

The sensitivity of mesh size was tested by fixing the time step and initial condition while varying the mesh size. Two sets of runs were conducted, first set with dt=0.1s, IC=1, second set with dt=0.05s, IC=1. The detail results of the runs are tabulated in Appendix IV. The flow depths for both sets indicate that the standard deviations do not exceed orders of 1/100 m (equivalent to ~1/10 of percent of the mean sub-patch flow depth). The friction velocities for both sets indicate that the standard deviations do not exceed orders of 1/1000 m/s (equivalent to ~1 percent of the mean sub-patch friction velocity). The statistics indicate independence of the flow depth and, to a lesser degree, the friction velocity from the mesh size.

In addition, spatial convergence of the simulation was examined based on Roache's [61] approach. The approach requires a minimum of three mesh sizes with constant refinement ration r are used. We will use solutions ϕ_1, ϕ_2, ϕ_3 obtained form simulations with mesh size $dx_1 < dx_2 < dx_3$ respectively to demonstrate the approach. The solutions of mesh refinement must also be monotonic ($|\phi_2 - \phi_1| < |\phi_3 - \phi_2|$) and converging ($(\phi_2 - \phi_1)(\phi_3 - \phi_2) > 0$). Once these conditions are satisfied the spatial convergence is determined by first estimating the order of convergence as

$$po = \frac{\ln\left[\frac{(\phi_3 - \phi_2)}{(\phi_2 - \phi_1)}\right]}{\ln(r)} \quad (44)$$

The theoretical order of convergence is 2 but it is often lower due to mesh quality, non-linearity in the solution, and turbulence approximation. With the order of convergence computed, Richardson extrapolate can be computed. This is an extrapolation of the solutions from the two finest mesh size, which represents the solution if the mesh size was reduced to 0, i.e. the continuum value. It is evaluated as

$$(45)\quad \Pr_{h=0} = \phi_1 + \frac{\phi_1 - \phi_2}{2^p - 1}$$

Using a factor of safety of 1.25 for employing three mesh sizes, grid convergence index is computed from the two finest mesh size as

$$(46)\quad GCI_{12} = 1.25 \frac{\left| \frac{\phi_1 - \phi_2}{\phi_1} \right|}{2^p - 1} * 100\%$$

And for the two coarsest mesh size as

$$(47)\quad GCI_{23} = 1.25 \frac{\left| \frac{\phi_2 - \phi_3}{\phi_2} \right|}{2^p - 1} * 100\%$$

Based on this method, one may conclude that the solution is equal to $\Pr_{h=0}$ with an error band of GCI_{12}. The lower the grid convergence index, the closer the solution is to the estimated continuum value.

Finally, one may check if the solutions are within the asymptotic range of convergence by observing the grid convergence index values as

$$(48)\quad ConvergenceRange = \frac{GCI_{23}}{r^p GCI_{12}}$$

The closer the ratio is to unity, the closer the solutions are to the asymptotic range of convergence.

The spatial convergence results for flow depth (Appendix IV-a and Appendix IV-b) show that the solutions in 23/32 sub-patches satisfies the monotonically converging condition that are well within the asymptotic range of convergence. These solutions have errors in the order of 1/10 of percent, except for sub-patch 1 (in Appendix IV-b) and sub-patch 1 and 26 (in appendix IV-a) which have errors in the order of 1 percent.

The spatial convergence results for friction velocity (Appendix X and Appendix X) show that the solutions in 20/32 (in Appendix IV-c) and 21/32 (in Appendix IV-D) sub-patches satisfy the monotonically converging condition that are well within the asymptotic range of convergence. The errors range in ~10-~1/100 percent (in dt=0.1s) and ~1-1/1000 percent (in dt=0.05s). For the improvement in reducing the absolute value of errors, the smaller time step (dt=0.05s) was chosen as the suitable resolution for temporal discretization.

Although Roache's spatial convergence approach indicate that some of the sub-patch solutions have not reached spatial convergence (not monotonically converging), the small standard deviation amongst the solutions of mesh refinements have been considered as sufficient evidence to conclude that the satisfactory level of spatial independence of the numerical solution have been reached. Consequently, the largest mesh size (dx=2m) was chosen as the suitable mesh size given the minimal wall-clock time requirement to complete the simulation

3.4.2.3 Parallel Core Sensitivity and Scaling Analysis

The numerical computations were conducted on Briaree, a high-performance computer cluster at the University de Montreal. The simulations were run in parallel mode, which divide the model domain into subdomains to solve the governing equations in multiple nodes simultaneously to increase computational efficiency. Since the accuracy of the domain-scale solution is dependent on the method of domain division and locations of the domain divides, a sensitivity analysis of parallel computation was conducted by comparing serial and parallel computational solutions (dx = 2m, dt = 0.25s, IC = 1).

Six different runs were conducted using 1 (serial), 8, 24, 36, 60 and 120 cores. Flow depth, x-velocity, y-velocity, turbulent kinetic energy and rate of turbulent dissipation were analyzed node by node (total number of nodes: 286293) against the solutions of the serial run. The detail results of the parallel core sensitivity analysis may be found in Appendix VI. Here the serial run was considered to be the "true" solution in the sense that it was free of errors associated with sub-domain discretization and solution exchange algorithm. The results show that the mean absolute error and standard deviation are extremely small. The standard deviation for flow depth and turbulent kinetic energy decrease as the number of cores are increased. The standard deviation of the x and y velocities and rate of turbulent dissipation increase as the number of core increases. Nonetheless, these increase in the standard deviation is minute and should not be considered a significant source of error.

In addition, a scaling analysis was conducted to explore the effects of number of parallel processors used on the computational wall clock time. As illustrated in the Figure 27, the increase in computational speed decays exponentially. It was deemed that 120 parallel processors were the optimum set up for the present study, beyond which the increase in computational resources could not be justified by the increase in computational speed.

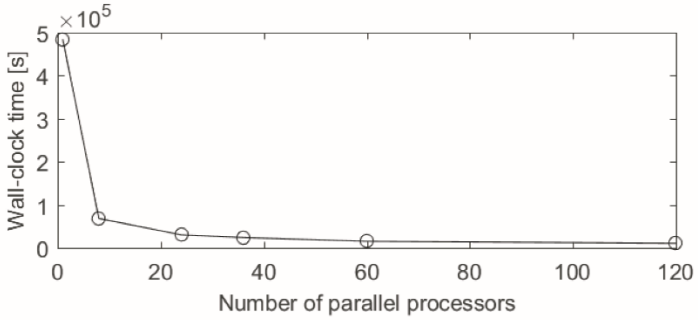

Parallel processors	Wall-clock time
	[hr:m:s]
1	134:30:04
8	18:55:58
24	8:20:16
36	6:37:36
60	4:11:47
120	2:54:07

Figure 27. Summary of the scaling analysis

3.4.3 Computational Mesh

The model domain is discretized into unstructured triangular elements. Initially, the entire extent of RTM is used as model domain to simulate the target flow event. Once the extent of wetted zone corresponding to the target flow is established, the model domain is reduced to the wetted zone plus buffer zones on both banks (Figure 28). A constant domain corridor width, B, of 110 m was used to produce domain corridor.

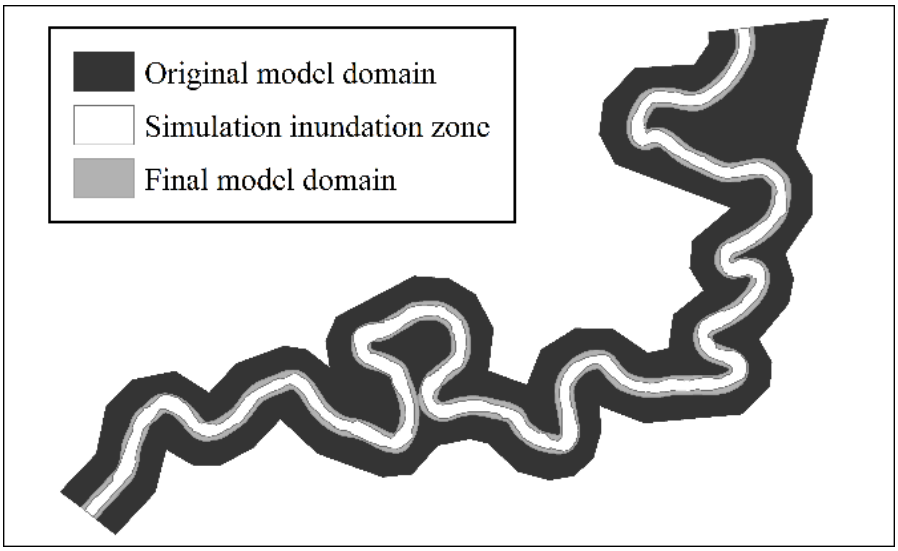

Figure 28. Evolution of model domain

The mesh was prepared in Blue-Kenue, a pre/post processing software developed by National Research Council. The mesh was generated by specifying the along channel edge length, l, and cross channel node number as

(49) $$N_{crosschannel} = \frac{B}{l} + 1$$

to produce nearly uniform, equilateral triangular mesh (Figure 29). Detail statistics of the computational meshes may be found in Appendix II.

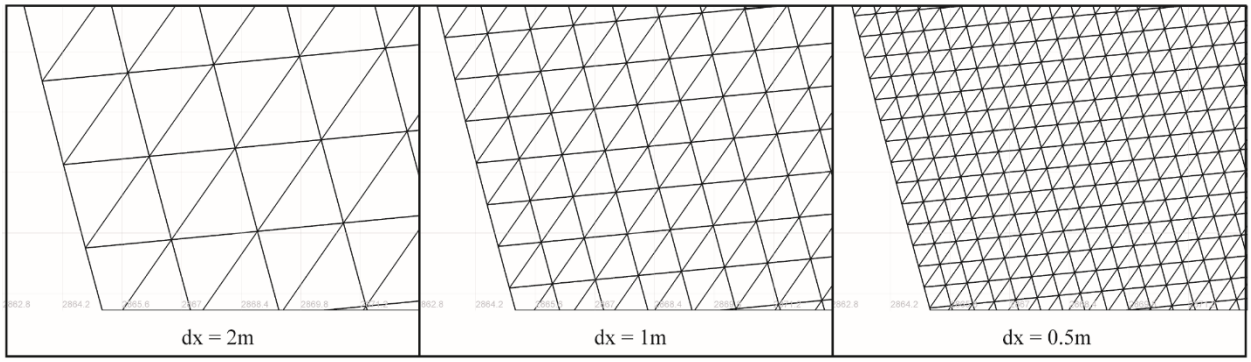

Figure 29. Sample triangular mesh used for the numerical study

3.4.4 Simulation Parameters

The simulation parameters are summarized in table 2.

Table 2. Simulation and numerical parameters

	Location	Type	Value
Boundary Condition	Inlet	Constant Discharge	102 m^3/s
	Outlet	Rating curve[a]	
	Lateral	Free Velocity	
	Channel Bottom	Constant Manning's n[b]	0.0425
Initial Condition	Entire Domain	Constant free surface elevation	223 m
		Constant velocity	(1 m/7 m above inlet/outlet)
	Inlet	Turbulent quantity gradients	$\frac{\partial k}{\partial h} = 0$, $\frac{\partial \varepsilon}{\partial h} = 0$
Time Step		Constant time step	0.05s
Simulation Time			10h
Wall-Clock Time			3h
Parallel Processors			120
Convergence		Minimum residual	<1E-6

[a] Constructed from low, high and bankfull stages. Higher flow stages estimated from normal flow Manning's equation

[b] Based on (Chow, 1959) for major streams with top width at flood stage > 100 ft

3.4.5 Determining steady-state solution

The objective of the numerical study was to determine the steady-state boundary shear stress corresponding to the bankfull event. Consequently, it was necessary to establish a criteria to determine if the convergent solutions had reached a steady-state. The cross sectional volume flux, Q, and the rate of cross sectional volume flux, $\partial Q / \partial t$, was monitored for five cross sections (Figure 30)spaced approximately evenly through the reach.

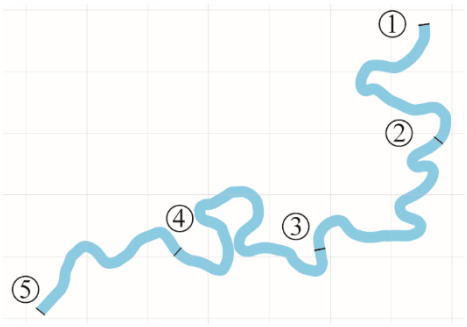

Figure 30. Locations of the discharge monitoring sections

The use of constant water-surface-elevation initial condition meant that volume of water in the system was maximum at the initial time step and gradually drained the fluid volume thereafter following an exponentially decay pattern. Since the river is sloped from upstream to downstream, the constant elevation initial condition causes initial water depth to be greater in the downstream reach compared to the upstream. This results in the upper most reach to reach a steady-state first, then the region of steady-state propagates in the downstream direction. This phenomenon is illustrated in the Figure 31 and the discharge time series.

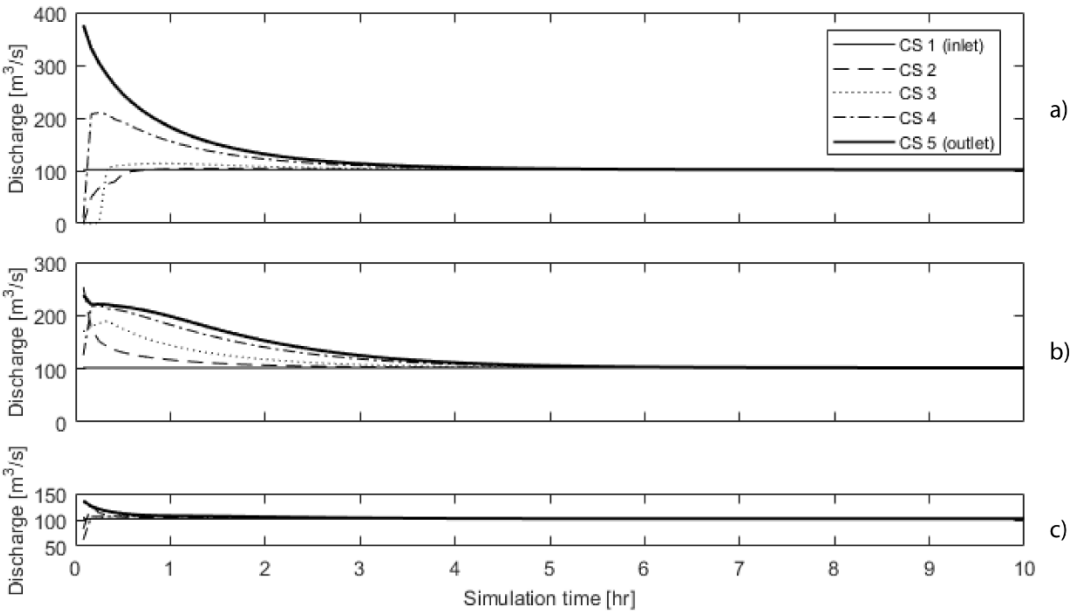

Figure 31. Discharge monitored at five control sections (locations corresponding to Figure 30) for simulations utilizing three different initial conditions a) constant elevation, b) constant depth, c) 1D-flow

4.0 RESULTS AND DISCUSSION

4.1 Bathymetry map

In this study, the accuracy of the image-derived bathymetry map was not verified against field survey data due to a lack of available data and resources to carry out a survey of such scale. However, the retrieved bathymetry (Figure 38) visually conforms to many of the prominent morphological features expected in a meandering river. Series of pool-riffle system can be seen throughout the reach, with an average wavelength of approximately ten channel widths. The majority of the thalweg shifts toward the outer bank of the bends and high gradient outer bank slopes are observed in the pools. On the contrary, the inner banks of the bends have a relatively a gradual slope that corresponds to gradual transition into the point bars (Figure 33). The pools are characterized by large flow depth and the riffles are characterized by shallow flow depth. Between two pools, a lateral shift in the location of the lowest bed elevation can be observed from one outer bank to another, where the centerline is crossed approximately at the entrance of the downstream bend.

Due to the complexity of resolving the stage gap, an attempt was made to retrieve bathymetry from the stereo images (same images used to produce the DEM). Unfortunately, this was unsuccessful due to a significant amount of specular reflection in the images. The sensors on Pleiades-A1 are oblique (to the nadir) which exaggerate the stereo parallax and improves triangulation-based altimetry. The oblique sensor angle, however increases the sun glint in the free surface and increases area where bathymetry must be interpolated.

4.2 The River Terrain Model

A comparison of RTM generated using constant Δh and variable Δh stage gap resolution technique yielded rivers with slightly variable slopes. The dependence of the choice of Δh on the longitudinal slope of RTM is alarming since the antecedent hydrodynamic simulation is based on this RTM (Figure 39). As the phenomenon to be modelled is open channel flow, which is dominated by gravitational acceleration, uncertainty in the slope of the river may result in significant errors. Due to a lack of field measurements to validate the stage gap resolution methods, it is not possible to comment on the accuracy of the RTM. In this author's opinion, further studies are required to assess the performance of the variable Δh resolution method.

Recent research in subaqueous LiDAR application has shown promising advancement in point cloud bathymetric retrieval. LiDAR was previously problematic due to a lack of penetration depth which limited its applications to very shallow rivers. However, recent studies [62, 63] have shown successful applications of green laser LiDAR bathymetry in rivers as deep as 4.5 m. In light of this recent advancement, the author urges future RTM generating endeavors to stir towards LiDAR point cloud data instead, which is able to collect subaqueous and terrestrial data simultaneously. This eliminates the necessity to resolve the stage gap, eliminating a source of error in generating the RTM among other advantages (higher spatial resolution, ability to differentiate tree canopies from land).

4.3 Hydrodynamics

4.3.1 Flow depth

The predicted flow depth captures the flow characteristics of the pool-rifle system. Figure 32 clearly illustrates the deepening of the flows in the transect sections (Figure 32) 5 to 8 and 22 to 26, coincident with the locations of pools. Transects 13 to 18 show shallow flow, coincident with the location of the riffle. The overall longitudinal trend of the flow depth contour (Figure 40) also suggests that alternating deep-shallow flow sections are aligned with the pool-riffle system.

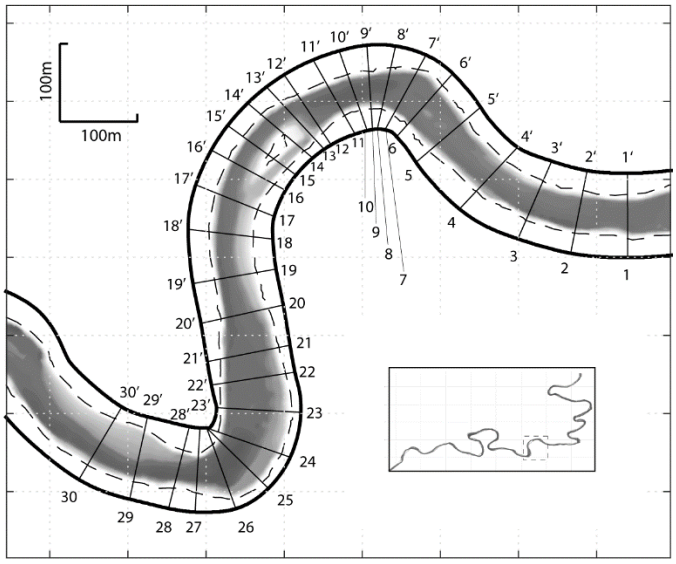

Figure 32. Section of the River examined in detail for cross-sectional flow depth

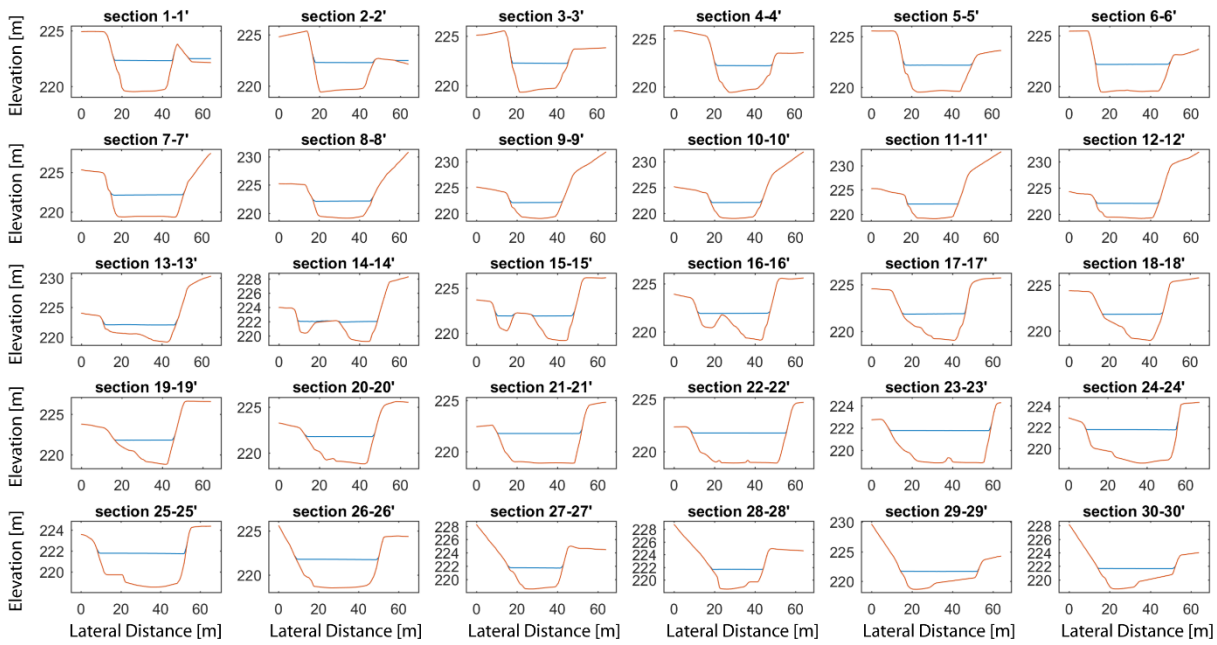

Figure 33. Cross-sectional flow depth, locations correspond to the map in Figure 31

The free surface elevation contour map confirms that super elevation of the free surface is being properly accounted for by the numerical model (Figure 34). The super elevation is correctly predicted in the meander bends, where the centripetal force acting on the fluid is significant.

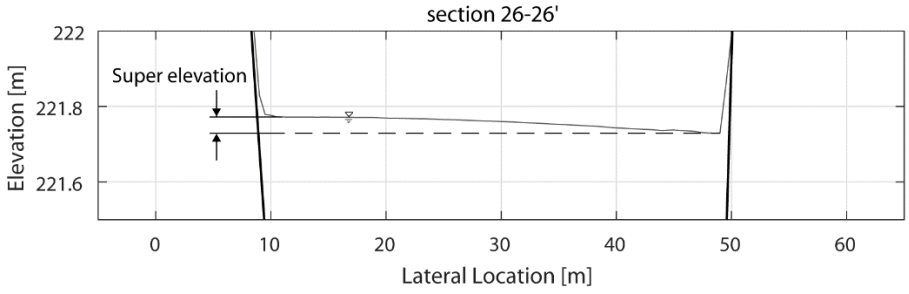

Figure 34. Predicted super elevation of free surface at section 26, location correspond to the map in Figure 32

Super elevation is an important hydrodynamic characteristic observed in meandering rivers and it is the main means through which helicoidal circulations are sustained. Although helicoidal circulations are not captured in the present 2-D simulation, evidence of super elevation suggests that the distribution of the static pressure on the river boundaries are properly accounted for.

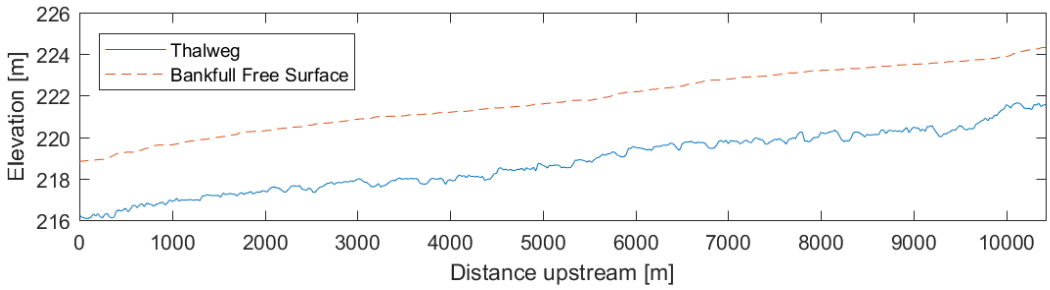

Figure 35. Long profile of the free surface profile corresponding to the bankfull event

4.3.2 Velocity

4.3.2.1 Locus of cross sectional velocity maxima and meander flow types

The simulation velocity patterns are illustrated in Figure 41 and Figure 42. The locus of local velocity maxima show that the core of the flow oscillates between the inner and outer banks (Figure 36*Figure* 1). The trajectory distinguishes two types of flows: transitional meander flow and developed meander flow (Figure 37). The approaching transitional flow spans from the riffle at Cross Section A-A to slightly after the midpoint of the bend at Cross Section B-B. In this region, the velocity core, which has been hugging the right bank, crosses the centerline approximately at 1/4 of the way into the bend, then gradually shifts towards the left bank (outer bank of the bend). Given sufficient distance from the bend entrance, at cross section B-B, the velocity core shifts even closer to the outer bank. Between this point (cross section B-B) and the bend exit (cross section C-C), the distance of velocity core to the outer bank is minimal and stays relatively constant, representing a region of developed meander flow where the possibility of erosion is highest (proximity of velocity core to the banks represent region of high velocity gradient and therefore high boundary shear stress)

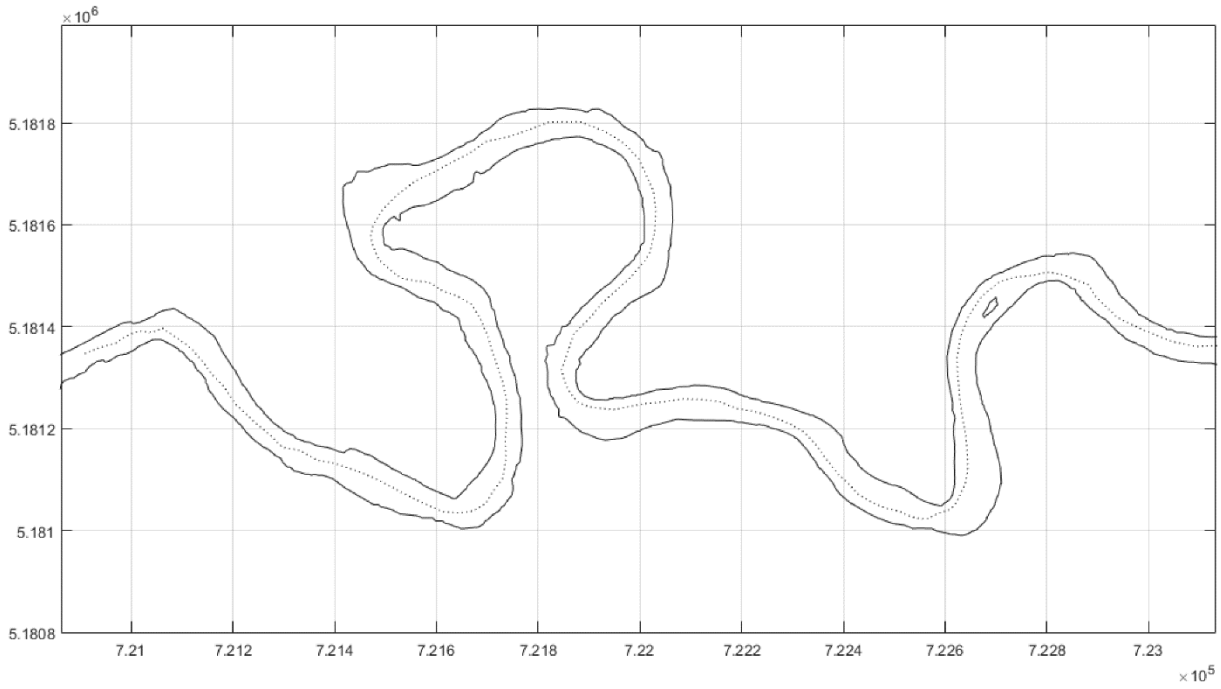

Figure 36. Locus of cross-sectional velocity maxima represented by the dotted line

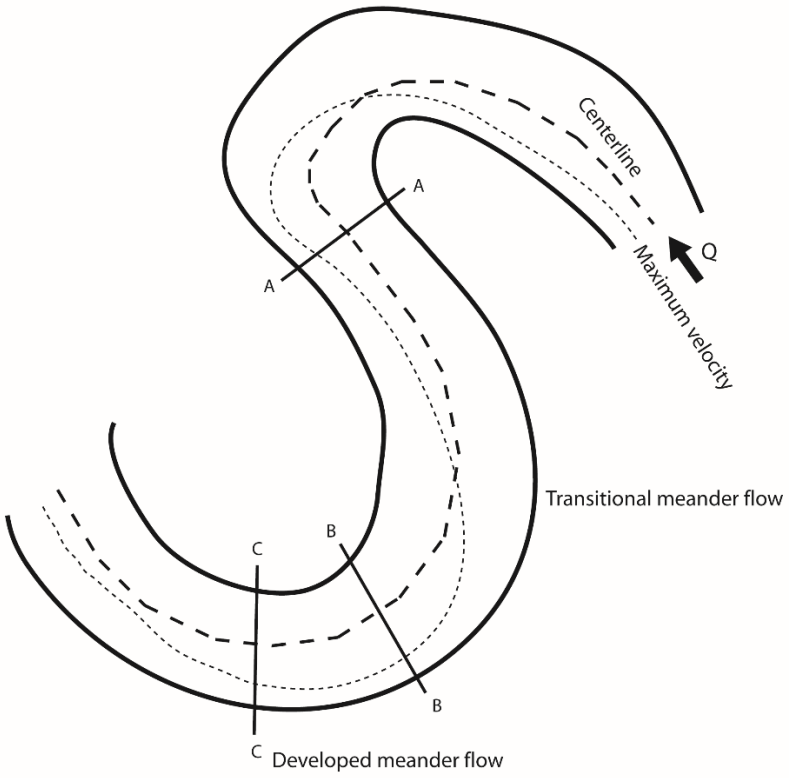

Figure 37. Schematic representation of the meander flow types

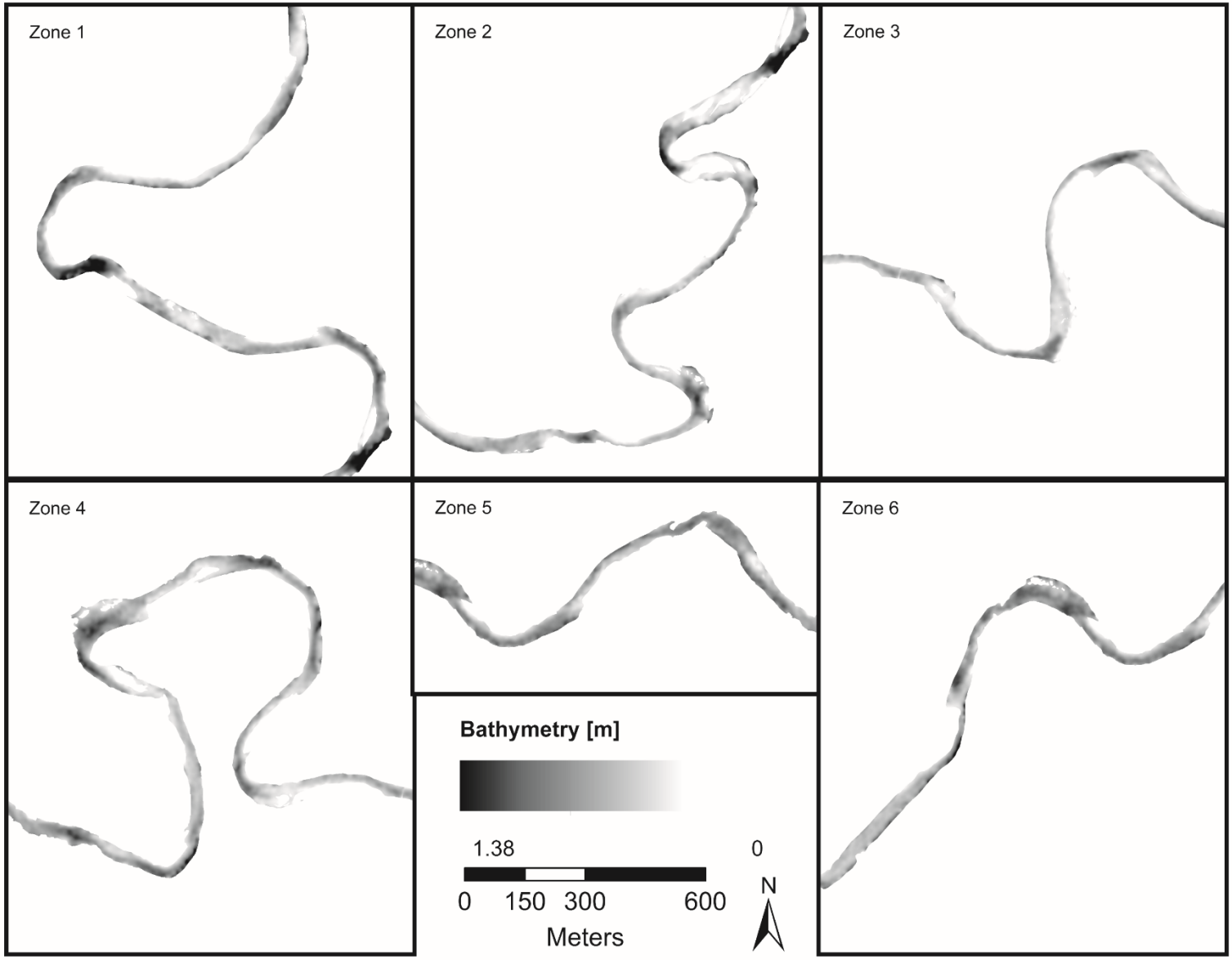

Figure 38. Bathymetry map derived from the Geoeye-1 multispectral image

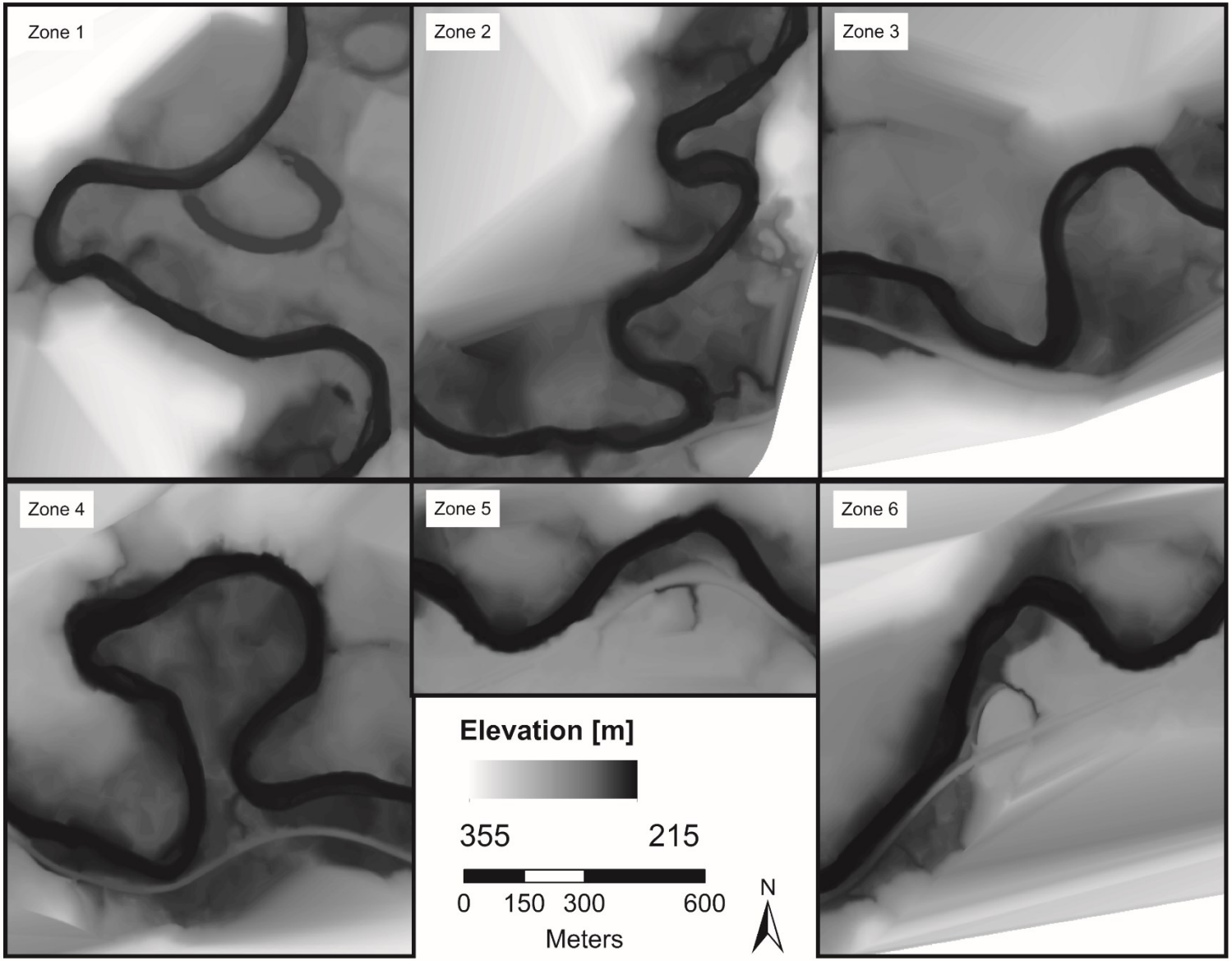

Figure 39. River Terrain Model (RTM)

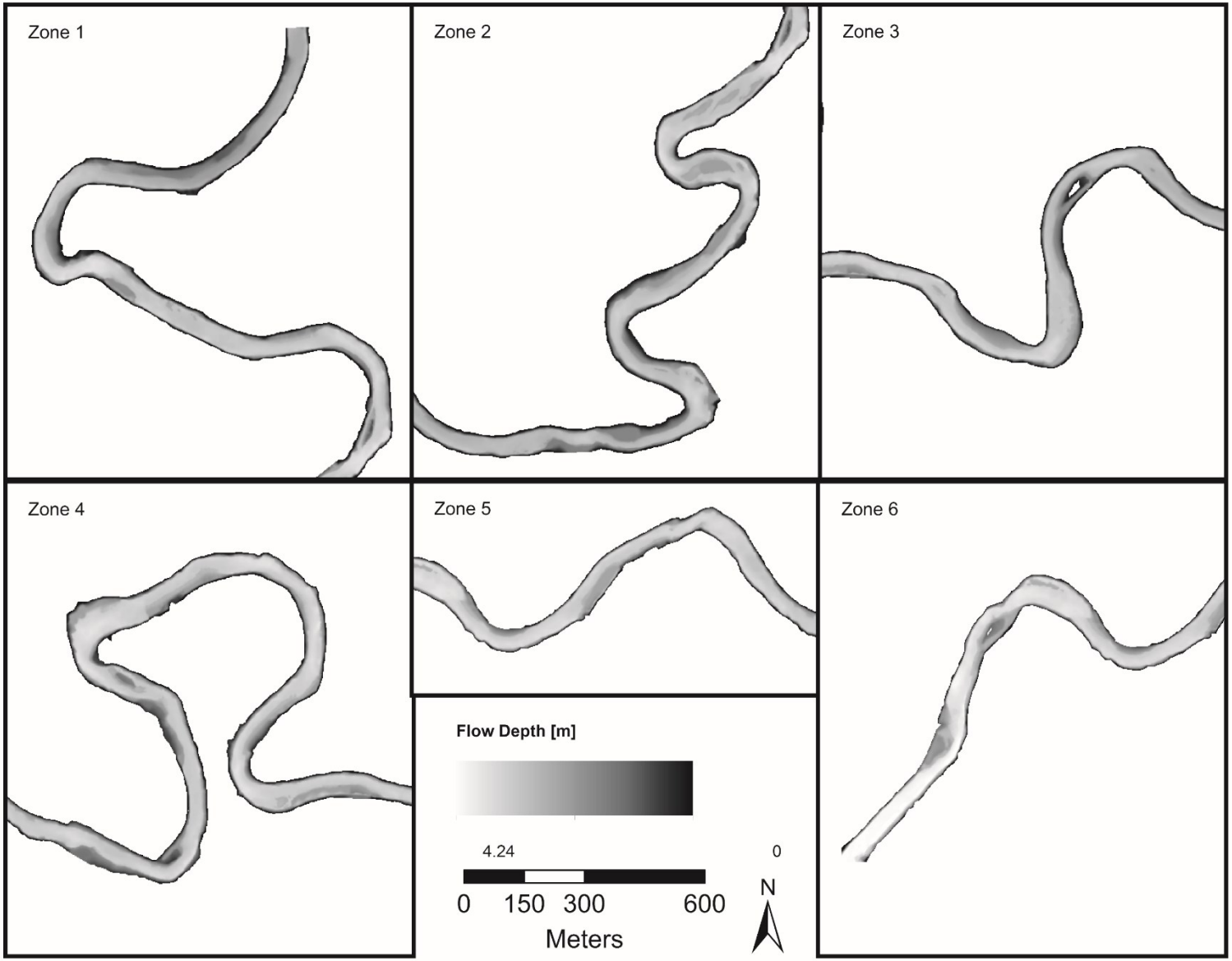

Figure 40. Predicted flow depth corresponding to bankfull event

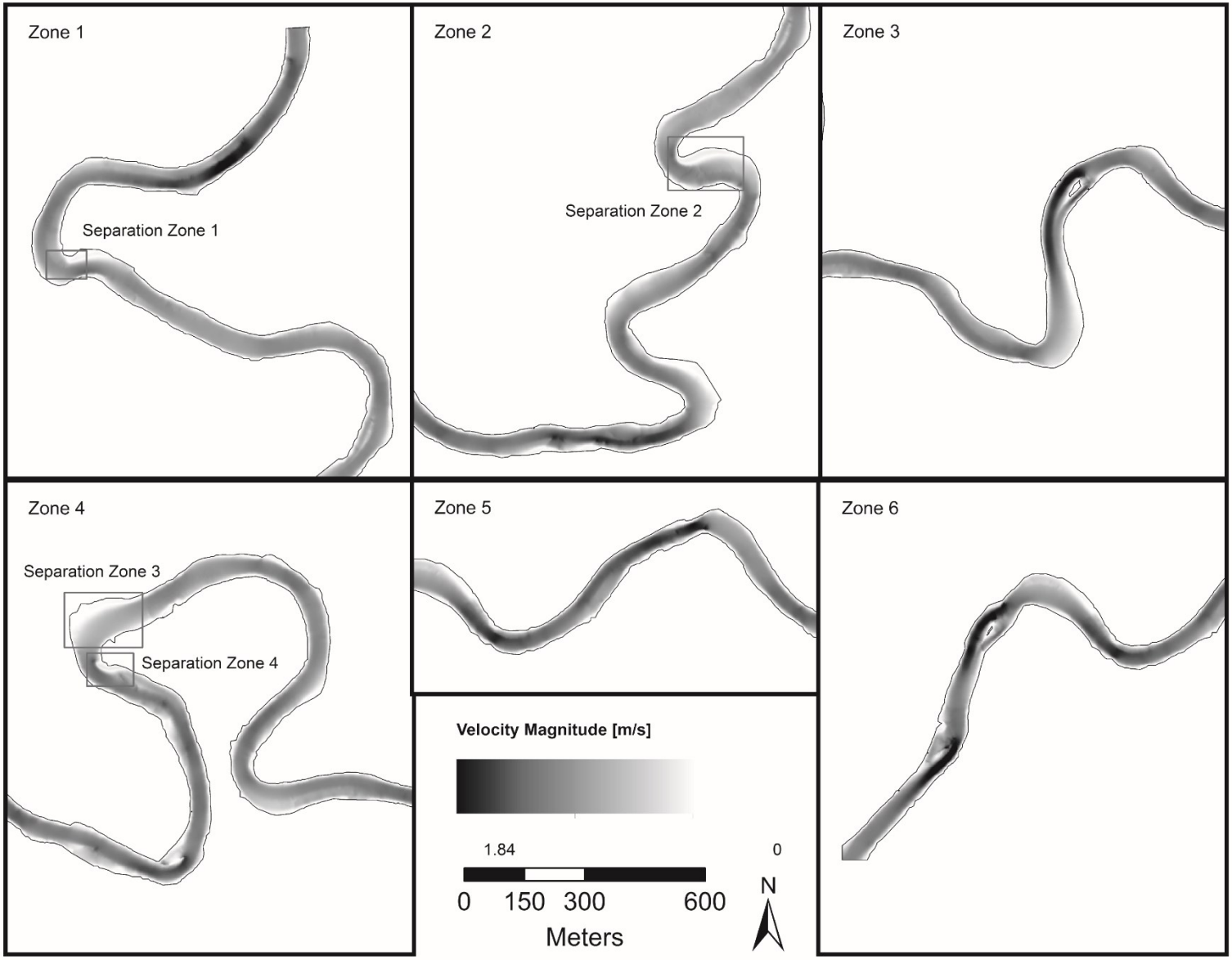

Figure 41. Predicted flow velocity magnitude corresponding to bankfull event

4.3.2.2 Cross sectional velocity profile

The cross sectional velocity profiles (Figure 42) are constructed by projecting the velocity vectors onto the vector normal of the cross sections. The flow characteristics of pools and riffles are clearly distinguishable and match the description of Dietrich and Smith [64] and Caamano et al. [65]. There is a significant lateral velocity variation in the pool flows, where slow-moving flow exists in the deep outer bank, and fast-moving flow exists in the shallow inner bank. The slow-moving flow acts as an obstruction, effectively constricting the flow which results in acceleration of the converging flow. This high velocity core results in localised boundary shear stress, and it is expected to serve as the primary pathway to move sediments through the pool [66]. On the contrary, the high-velocity flow is distributed through most of the cross sections in the riffles. Consequently, the boundary shear stress is distributed relatively evenly across the cross section and sediment transport is expected to take place throughout the cross section.

The lateral shift in cross sectional velocity maxima (described in Section 4.3.2.1) can be clearly seen in the velocity profiles. The relative lateral distribution of streamwise velocity at various locations in the meander matches previously reported field data [67, 68, 69, 70].

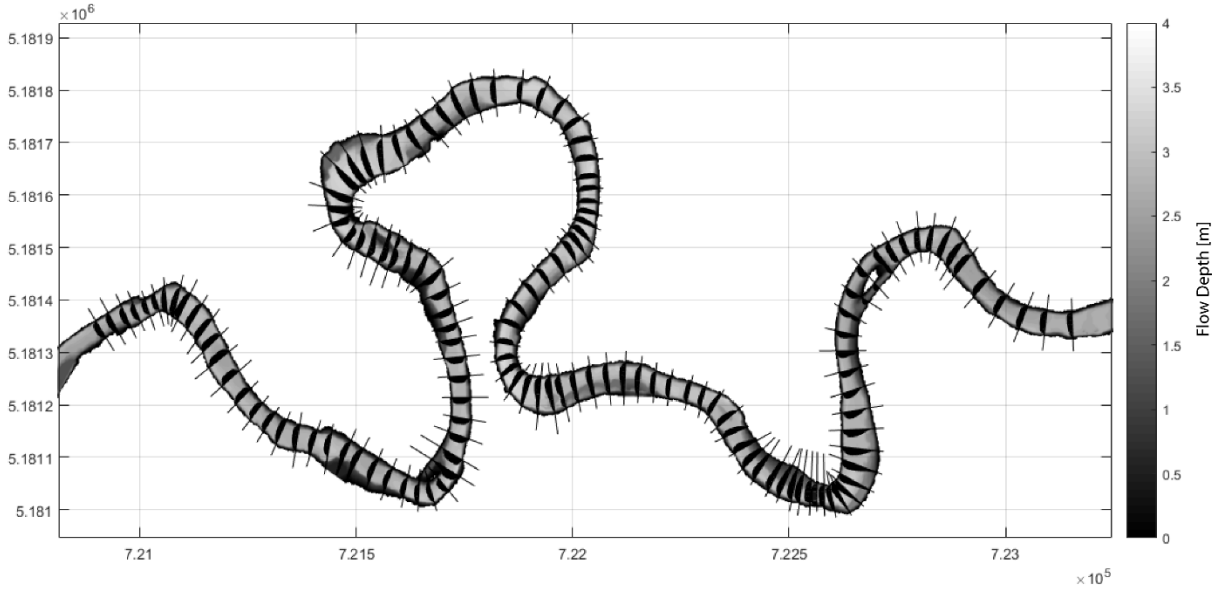

Figure 42. Cross sectional velocity profile generated from predicted velocity components

4.3.2.3 Flow separation

The velocity vectors show regions of flow separations within the study reach. A higher probability of flow separation is observed around tighter bends with low meander radius (Figure 43).

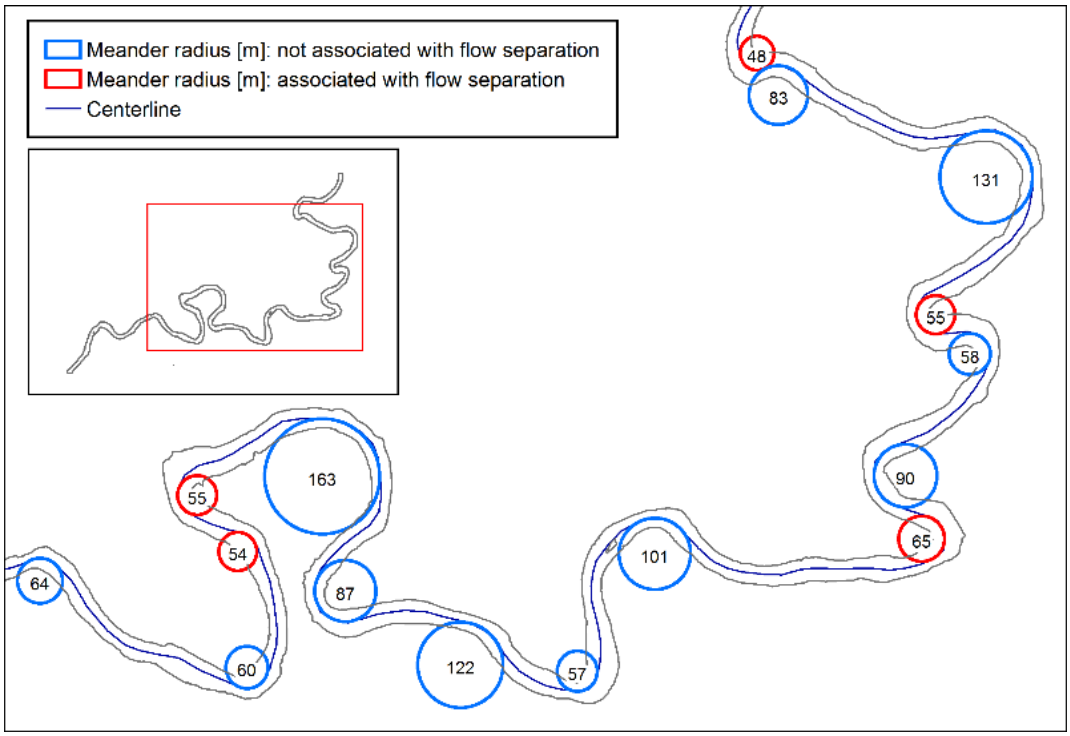

Figure 43. Meander radius

The recirculation eddies can be observed either on the midpoint of the outer bends (Figure 44c) or the trailing portion of the inner bends (Figure 44a,b,d).

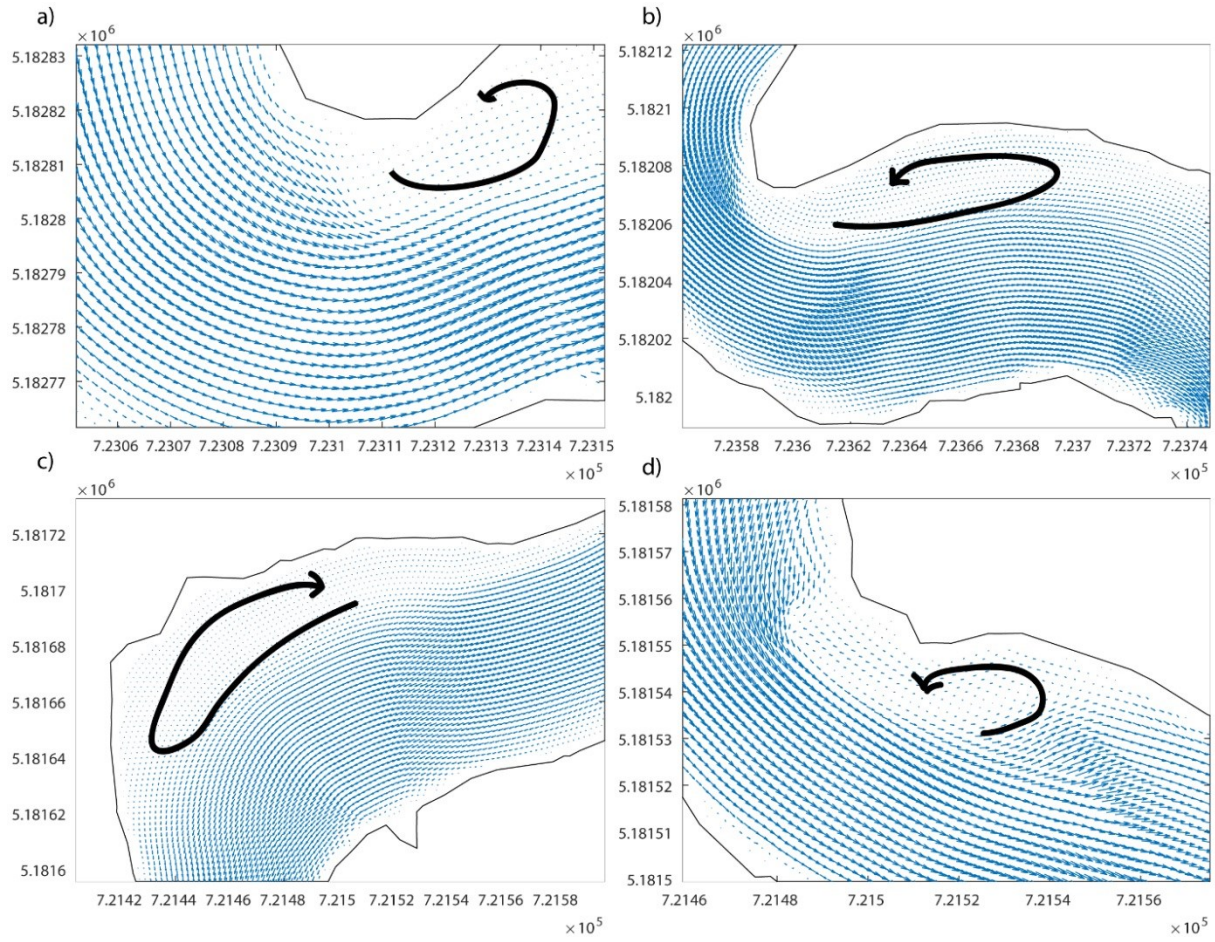

Figure 44. Predicted velocity vector field indicating the locations of flow separation. Locations corresponding to the separation zones a) 1, b) 2, c) 3, d) 4 (Figure 41)

The separation zones are morphologically significant because of their low velocities, which allow bed loads to deposit at the trailing edges of the point bars, leading to downstream migration of the bars. In addition, deep pools are observed laterally next to the recirculating eddies, which show that the separation zone effectively narrows the flow area. This effect is compensated by vertical scouring of the bed, which becomes the pools.

4.3.3 Turbulence

The predicted turbulence kinetic energy (TKE) contour (Figure 45) suggests that the TKE is generally concentrated around the velocity core (high TKE regions migrates from one bank to another in successive bends just as the velocity core). A comparison between the predicted TKE and the Reynolds number (RE), computed by taking the flow depths as the length scale, shows that

Re is a good predictor for TKE. The contour plot shows that high levels of TKE are predicted in both the riffles and the pools. In the riffles, high values of TKE are predicted in the mid channel, with an approximate thickness of 1/3 of the channel width. Elevated levels of TKE are also predicted in the regions leading and trailing the riffles. The leading regions are observed to originate from a point in the inner banks of the bends and the trailing regions are observed to terminate located in the outer bank of the bend exits/riffles. In the pools, a significant cross-channel variation is observed, where TKE increases towards the inner bank. There are distinct discontinuities in the TKE, about 1/4-1/2 of the way into the bends. This may be explained by the reduction in flow velocity due to the lateral and vertical expansion of the effective flow area in these leading-pool regions, as seen from the flow depth map (Figure 40). Engel and Rhoads [67] (meander loop in the Embarras River, IL, U.S.A.) and Nukhodolov [69] (meander bend in the Spree River, Germany) reported similar TKE discontinuity just before the tightest region of the bend. In addition, the lateral shift of the TKE from one bend to another is also reported in the field measurements of the aforementioned authors.

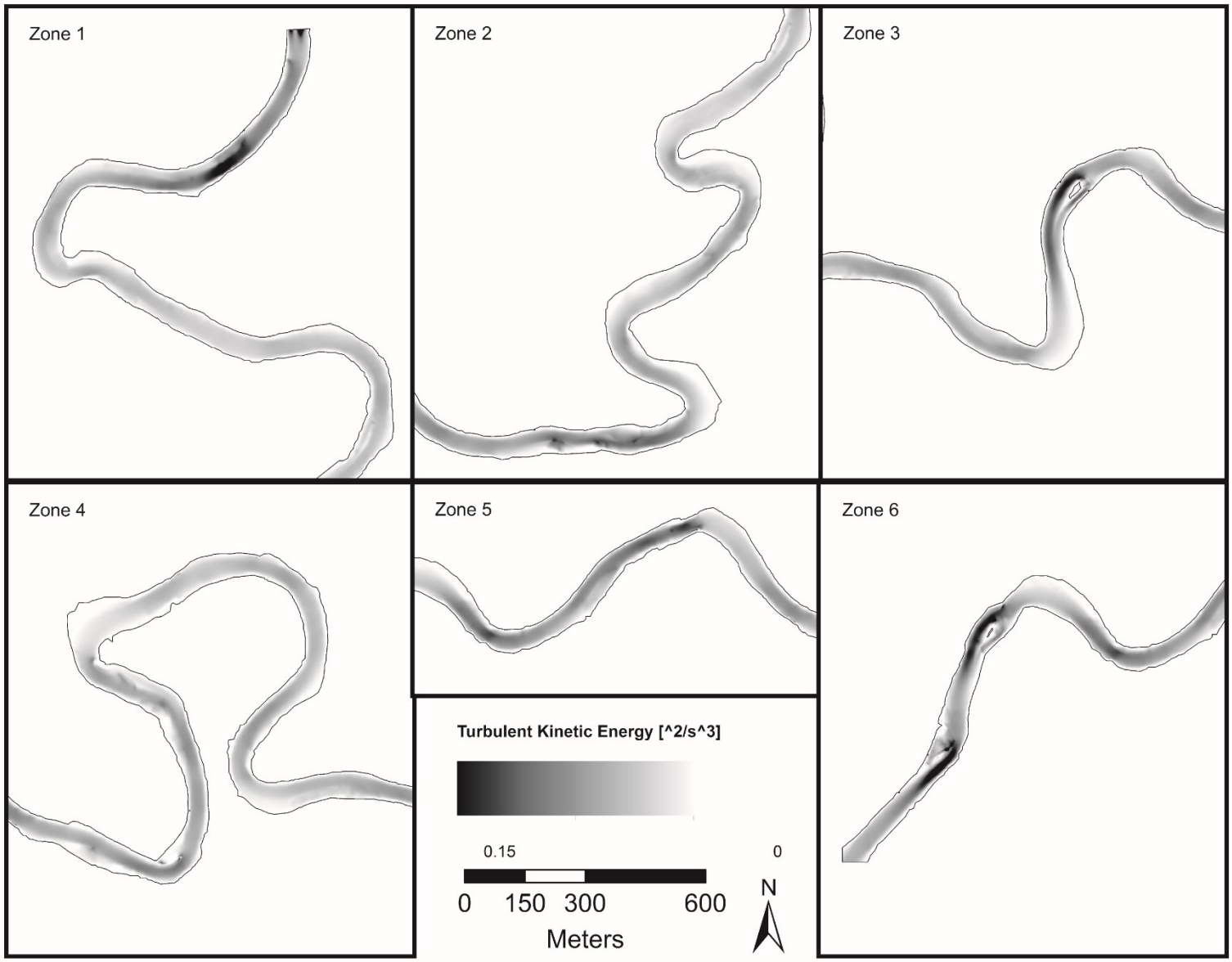

Figure 45. Predicted turbulent kinetic energy corresponding to bankfull event

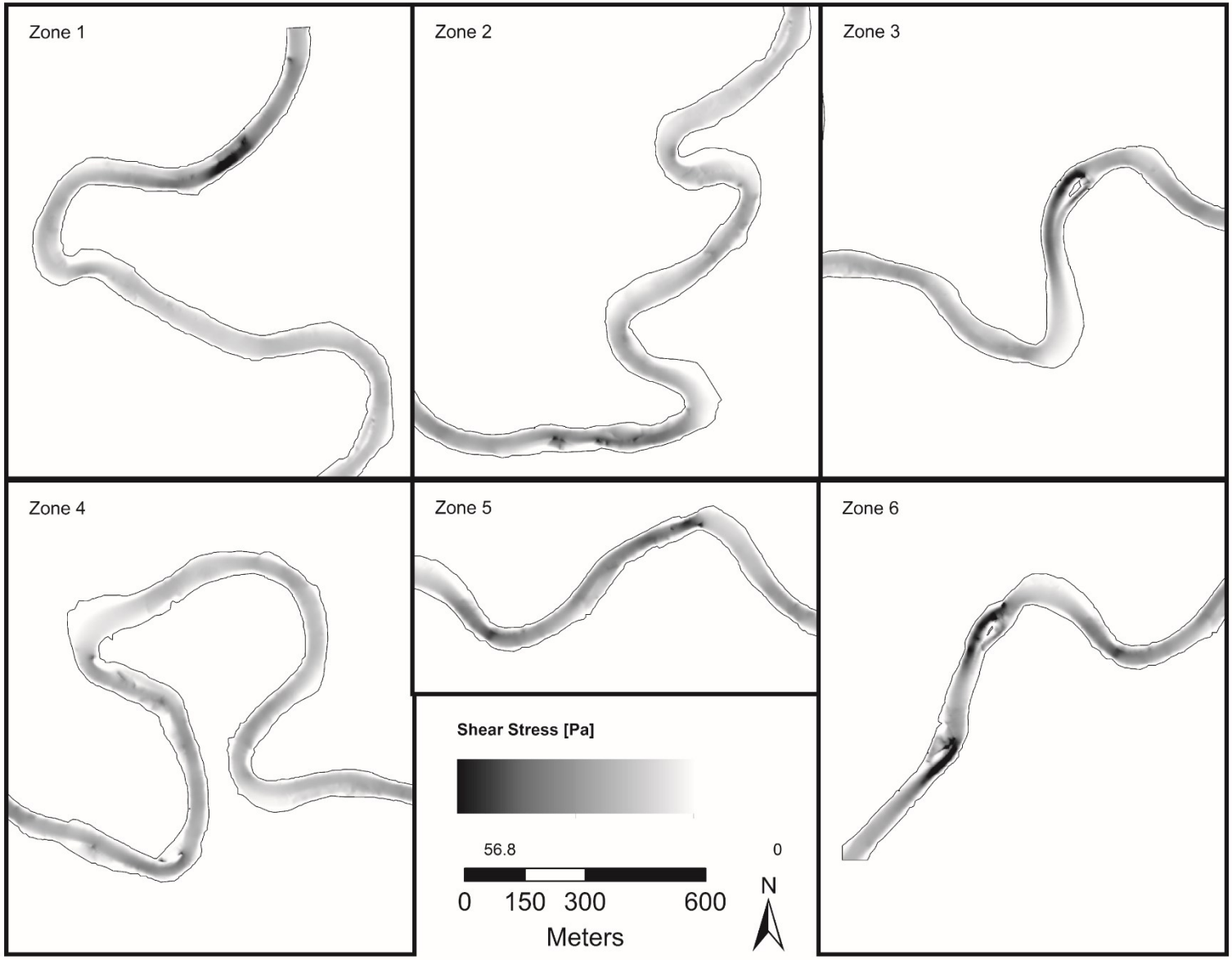

Figure 46. Predicted boundary shear stress corresponding to bankfull event

4.3.4 Boundary shear stress

The longitudinal distribution of boundary shear stress (Figure 46) generally follows the pool-riffle sequence. High boundary shear stresses are found in the riffle zones (high velocity low flow depth) and low boundary shear stresses are found in the pools (low velocity high flow depth). In the lateral direction, the boundary shear stress is concentrated at the inner half of the channel as the flow approaches the bend. As the flow enters the bend, the boundary shear stress in the outer half of the channel reaches local minima due to the presence of pool (deep and slow flow). On laterally opposite side of the pool (inner bank), there is a concentration of high boundary shear stress. At about the ¼ of the way into the bend, the region of high boundary shear stress grows from the inner bank towards the outer bank, corresponding to the location where the locus of cross-sectional velocity maxima crosses the centerline. This growing region of shear front propagates past the centerline at approximately the midpoint of the bend.

Extreme boundary shear stresses are observed in regions where the channels narrow, such as the split flows at mid-channel bars. In both cases of the mid-channel bars (Figure 46, zone 3 and 6), one of the two branches carries the majority of the flow as indicated by the velocity profile and the flow depth contour. The flow depth also decreases in the mid-channel bar branches, decreasing the conveyance in these branches. In order to conserve mass, the decrease in conveyance is compensated by an increase in slope of the channel through aggradation of the branches. The increased slope increases the velocity in these branches, which ultimately results in high boundary shear stresses.

4.4 Sediment dynamics

4.4.1 Estimation of sediment caliber from shear stress

The sediment caliber in riffle zones was predicted with an r^2 value of 0.36 (Figure 47, Figure 48). Although the coefficient of determination is low, the positive trend of the regression indicates that the method is able to provide a rough estimate of the grain size. On the contrary, the majority of the predictions in the pools and regions leading/trailing the pools were overestimated. The author argues that this is the case because the bed shear stress in the riffle zone remain relatively high even at discharge lower than the bankfull discharge. As bankfull discharge events, by definition, occur approximately every 1-2 years, the interim lower flows bring about sediment transport that causes the sediment caliber distribution to deviate from the distribution just after the bankfull

event. This effect is most prominent in the pools, and to a lesser degree in the riffles, due to the reduced velocity (reduced bed shear stress) during low flows, leading to deposition of finer sediments (sand and silt). This causes the previously mobilized larger sediments during the bankfull event to be covered by the finer sediments. In addition, one to one relationship is not expected to hold between sediment caliber and bankfull shear stress in the non-riffle zone due to the complex 3-D flow patterns of helicoidal flow, which cannot be accounted for in 2-D simulation. The cork-screw like secondary flow acts as a mechanism to sort sediments in the lateral plane.

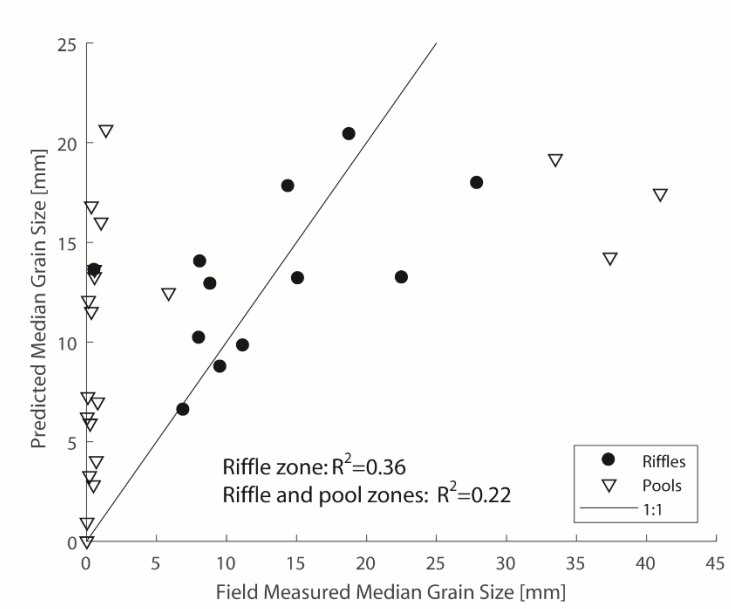

Figure 47. Comparison of field measured against predicted median grain size

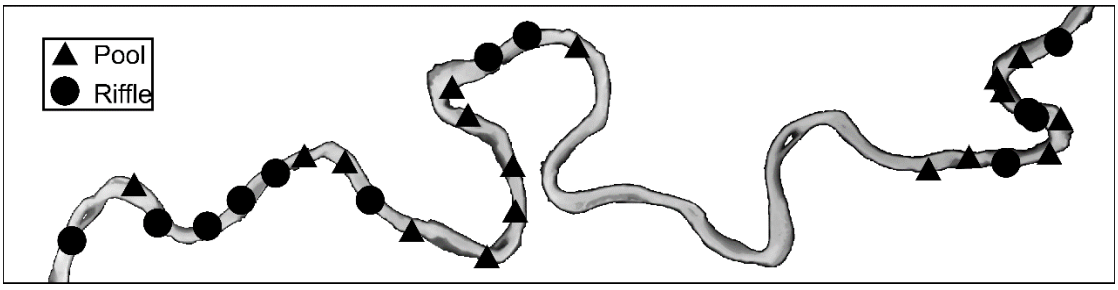

Figure 48. Location of field survey patches categorized by pools and riffles

The underprediction of the sediment caliber is most likely due to misrepresentation of colluvium (sediments transported to a location independent of the river flow, i.e. rainwash, sediments falling from side banks, etc.) as alluvium (sediments transported to a location by fluvial

transport) during the field survey described in Section 3.1. Colluvium is supply limited, meaning its loading on the river is independent of the hydrodynamics of the river. Since the biologists did not discern the two types of sediments, it is hard to conclude with certainty. For the underestimated patches in the left bank, particularly in those situated adjacent to the road, measurements may have coincided with locations of riprap, where larger boulders were introduced artificially to prevent lateral erosion. A lack of field notes and obervational notes by the surveyors make it difficult to confirm this theory.

5.0 CONCLUSION

5.1 Concluding remarks

This study reports the generation of river topography from satellite images and numerical model predictions of grain size in the Goulais River. The bathymetry is extracted from a high-resolution multispectral image by correlating the field measured depths and band ratio of the digital numbers. The dry terrain is reconstructed from pair of stereo images. The bathymetry map and the DEM are combined using conservation equations to consider the gap in the stages of the source images. 2-D depth-averaged, turbulent simulation was conducted with a finite element solver. Numerical solution has been evaluated for initial condition, mesh size, time step, and parallelization independence. The following conclusions have been reached:

- There is a need to appropriately account for the stage discrepancy between the bathymetry map and the DEM. The analysis of two methods (constant Δh and Manning's ratio) shows that the choice of the stage gap has an important influence on the slope of the river in the RTM, and consequently on the hydrodynamic simulation. Although the constant gap method presents a quick and easy solution, the author recommends the Manning's ratio method as it is site-independent and can be applied with minimal knowledge about the geography of the study site.
- The bathymetry map generated from correlation technique based on 32 field measurement and ratio of red and green bands qualitatively matches with many of the characteristics (shifting of thalweg, steep outer banks, gradual inner banks) observed in meandering rivers. The longitudinal and lateral location of pools and riffles are also in accord with theory.
- The optimum and simplest initial condition for 2-D hydrodynamic modelling of rivers was found to be constant free surface elevation. Constant flow depth initial condition took longest to reach steady state solution due to the sloshing of flow back and forth in the model domain. Although 1-D flow depth initial condition was the fastest to reach steady-state, it required additional geoprocessing and model set-up (HEC-RAS) which increased the pre-processing time.
- The model prediction has captured the essence of hydrodynamics (flow depth, x- and y-velocity components, turbulence kinetic energy). Super elevation of the free surface was properly accounted for and the cross-sectional velocity profile qualitatively matches with previously reported field measurements. The key to success in predicting the velocity vectors

around the meanders is to sufficiently refine the mesh so that the key flow features can be identified and so the numerical solution is independent of the spatial discretization.

- The proposed grain size prediction method achieved a R2= 0.36 in the riffle zones and R2= 0.22 overall. The improved predictive ability in the riffle zone is most likely due to the boundary shear stress in the riffle remaining relatively high during the interim low flow seasons between the bankfull events. The majority of the grain size outside of riffles are overpredicted, most likely due to deposition of fine sediments in the interim low flows.

5.2 Suggestions for future studies

For future application of remote sensing technology to generating river topography and grain size, the author suggests:

- using LiDAR point cloud, instead of multispectral images, to generate the bathymetry and DEM simultaneously from one dataset to avoid the need to resolve the stage gap and potential errors. If the depth of the river is too large for LiDAR application, it is recommended that the stage in the image used for bathymetric retrieval be higher than the image used for generating the DEM. This will leave a section of overlapping channel topography that should improve the bathymetry-DEM combining procedure.
- collecting detail bathymetric data in the field and using them to calibrate and validate the accuracy of remote sensing bathymetry retrieval technique. This should also allow assessment of effectiveness of the bathymetric retrieval based on the number of field surveyed calibration points.
- choosing a study site which has sediment bed load records (monitoring station nearby) so that sediment transport modelling may be conducted to predict time dependent grain size distribution (grain size not limited to that corresponding to the bankfull event). In addition, sediment transport modelling will allow prediction of channel evolution (vertically as aggradation/degradation, laterally as meander sinuosity increases, and longitudinally as the meanders migrate down the valley. The author recognizes that the sediment recording program has been terminated in most parts of Canada. Consequently, it is recommended that future studies are conducted in rivers in the U.S.A. where sediment records are regularly recorded.

REFERENCES

[1] M. Church, "Geomorphic thresholds in riverinee landscapes," *Freshwater Biology,* pp. 541-557, 2002.

[2] C. Davey and M. Lapointe, "Sedimentary links and stapial organization of Atlantic salmon (Salmo salar) spawmomg habitat in a Canadian Shield river," *Geomorphology,* pp. 82-96, 2007.

[3] S. Bunn and A. Arthington, "Basic principles and ecological consequences of altered flow regimes for aquatic biodiversity," *Environmental Management,* pp. 492-507, 2002.

[4] "Prof. Michel Lapointe," McGill University Department of Geography, 30 04 2008. [Online]. Available: http://www.geog.mcgill.ca/faculty/lapointe/.

[5] J. B. Campbell, Introduction to Remote Sensing, New York: Gilford Press, 2002, pp. 113-114.

[6] A. P. Cracknell and L. Hayes, Introduction to Remote Sensing, Boca Baton: Taylor & Francis Group, 2007.

[7] R. G. Congalton, "Selecting the Best Imagery," Vermont Center for Geographic Information, University of New Hampshire, 2014.

[8] P. E. Cabonneau and H. Piegay, Fluvial Remote Sensing for Science and Management, Singapore: Wiley-Blackwelll, 2012.

[9] J. R. Schott, Remote Sensing: The Image Chain Approach, New York: Oxford University Press, 1997.

[10] R. P. Bukata, "Optical Properties and Remote Sensing of Inland and Coastal Waters," Boca Raton, FL, CRC Press, 1995, p. 54.

[11] C. J. Legleiter, D. A. Roberts, W. A. Marcus and M. A. Fonstad, "Passive optical remote sesing of river channel morphology and in-stream habitat: Physical basis and feasibility," *Remote Sensing of Environment,* pp. 493-510, 2004.

[12] C. D. Mobley and L. K. Sundman, "Hydrolight 4.2 User's Guide," Sequoia Scientific, Redmond, WA, 2003.

[13] C. J. Legleiter, D. A. Roberts and R. L. Lawrence, "Spectrally based remote sensing of river bathymetry," *Earth Surface Processes and Landforms,* pp. 1039-1059, 2009.

[14] W. A. Marcus, "Remote sensing of hydraulic environment in grave-bed rivers," in *Gravel-bed Rivers: Processes, Tools, Environments*, Singapore, Wiley-Blackwell, 2012, p. 269.

[15] D. J. Gilvear, T. M. Waters and A. M. Milner, "Image analysis of aerial photograph to quantiify changes in channel morphology and instream habitat following placer mining in interior Alaska," *Freshwater Biology,* pp. 389-398, 1995.

[16] S. J. Winterbottom and D. J. Gilvear, "Quantification of channel bed morphology in gravel-bed rivers using airborne multispectral imagery and aerial photograph," *Regulated Rivers: Research & Management,* pp. 489-499, 1997.

[17] D. R. Lyzenga, "Remote sensing of bottom reflecrance and water attenuation parameters in shallow water using aircraft and LANDSAD data," *International Journal of Remote Sensing,* pp. 71-82, 1981.

[18] M. A. Fonstad and W. A. Marcus, "Remotesensing of stream depths with hydraulically assisted bathymetry (HAB) models," *Geomorphology,* pp. 320-339, 2005.

[19] C. J. Legleiter, "Calibrating remotely sensed river bathymetry in the absence of field measurements: Flow REsistance Equation-Based Imaging of River Depths (FREEBIRD)," *Water Resouces Research,* vol. 51, pp. 2865-2884, 2015.

[20] D. J. Gilvear, P. Hunter and T. Higgins, "An experimental approach to the measurement of the effect of water depth and substrate on optical and near infra-red reflectance: a field-based assessment of the feasibility of mapping submerged instream habitat," *International Journal of Remote Sensing,* pp. 2241-2256, 2007.

[21] R. D. Williams, J. Brasington, D. Vericat and D. M. Hicks, "Hyperscale terrain modelling of braided rivers: fusing mobile terrestrial laser scanning and optical bathymetric mapping," *Earth Surface Processes and Landforms,* vol. 39, no. 2, pp. 167-183, 2014.

[22] J. Lejot, H. Piégay, M.-L. Trémélo and P. Allemand, "Very high spatial resolution imagery for channelbathymetry and topography from an unmannedmapping controlled platform," *Earth Surface Processes and Landforms,* vol. 32, p. 1705–1725, 2007.

[23] W. A. Marcus, C. J. Legleiter, R. J. Aspinall, J. W. Boardman and R. L. Crabtree, "High spatial resolution hyperspectral mapping of in-stream habitats, depths, and woody debris in mountain streams," *Geomorphology,* vol. 55, no. 1-4, pp. 363-380, 2003.

[24] C. J. Legleiter, B. T. Overstreet, C. L. Glennie, Z. Pan, J. C. Fernandez-Diaz and A. Singhania, "Evaluating the capabilities of the CASI hyperspectral imaging system and Aquarius bathymetric LiDAR for measuring channel morphology in two distinct river environments," *Earth Surface Processes and Landforms,* vol. 41, no. 3, pp. 334-363, 2015.

[25] R. M. Westaway, S. N. Lane and D. M. Hick, "Remote sensing of clear-water, shallow, grave-bed rivers using digital photogrammetry," *Photogrammetric Engineering & Remote Sensing,* pp. 1271-1281, 2001.

[26] S. N. Lane, P. E. Widdison, R. E. Thomas, P. J. Ashworth, J. L. Best, I. A. Lunt, G. H. Samrook Smith and C. J. Simpson, "Quantification of braided river channel change using archival digital image analysis," *Earth Surface Processes and Landforms,* 2010.

[27] A. Tamminga, C. Hugenholtz, B. Eaton and M. Lapointe, "Hyperspectral remote sensing of channel reach morphology and hydraulic fish habitat using an unmanned aerial vehicle (UAV): A first assessment in the context of river research and management," *River Research and Applications,* vol. 31, no. 3, pp. 379-391, 2014.

[28] A. S. Woodget, F. Carbonneau, F. Visser and I. P. Maddock, "Quantifying submerged fluvial topography using hyperspatial resolution UAS imagery and structure from motion photogrammetry," *Earth Surface Processes and Landforms,* vol. 40, no. 1, pp. 47-64, 2015.

[29] L. Javernick, J. Brasington and B. Caruso, "Modeling the topography of shallow braided rivers using Structure-from-Motion photogrammetry," *Geomorphology,* vol. 213, pp. 166-182, 2014.

[30] C. Shintani and M. A. Fonstad, "Comparing remote-sensing techniques collecting bathymetric data from a gravel-bed river," *International Journal of Remote Sensing,* vol. 38, no. 8-10, 2017.

[31] M. R. James and S. Robson, "Straightforward reconstruction of 3D surfaces and topography with a camera: Accuracy and geoscience application," *Journal of Geophysical Research,* vol. 117, no. F3, 2012.

[32] M. J. Westoby, J. Brasington, N. F. Glasser, M. J. Hambrey and J. M. Reynolds, "'Structure-from-Motion' photogrammetry: A low-cost, effective tool for geoscience applications," *Geomorphology,* vol. 179, pp. 300-314, 2012.

[33] L.-L. Fu, D. Alsdorf, R. Morrow and E. Rodriguez, "SWOT: Surface Water and Ocean Topography Mission: Wide-Swath Altimetric Measurement of Water Elevation on Earth," Jet Propulsion Laboratory, 2012.

[34] Jet Propulsion Laboratory: California Institude of Technology, "Mission to Earth: Surface Water and Ocean Topography," [Online]. Available: https://www.jpl.nasa.gov/missions/surface-water-and-ocean-topography-swot/. [Accessed 30 8 2017].

[35] S. Biancamaria, D. P. Letternmaier and T. M. Pavelsky, "The SWOT Mission and Its Capabilities for Land Hydrology," *Surveys in Geophysics,* vol. 37, no. 2, pp. 307-337, 2016.

[36] E. Rodriquez, "Surface Water and Ocean Topography Mission (SWOT) Project," Jet Propulsion Laboratory, 2015.

[37] S. Biancamaria, K. M. Andreadis, M. Dunard, E. A. Clark, E. Rodoriguez, N. M. Mognard, D. E. Alsdorf, D. P. Letternmaier and Y. Oudin, "Preliminary Characterization of SWOT Hydrology Error Budget and Global Capabilities," *IEEE Joutnal of Selected Topics in Applied Earth Observation and Remote Sensing,* vol. 3, no. 1, pp. 6-29, 2010.

[38] D. C. Wilcox, Turbulence Modeling for CFD, La canada: DCW Industries, 2006.

[39] A. Shields, "Application of similarity principles and turbulence research to bed-load movement," *Hydrodynamics Laboratory publication,* 1936.

[40] M. F. Lapointe, Running Water Environments, Harvard Business School Publishing, 2016.

[41] J. M. Buffington, D. R. Montgomery and H. M. Greenberg, "Basin-scale availability of salmonid spawning gravel as influenced by channel type and hydraulic roughness in mountain catchments," *Canadian Journal of Fisheries and Aquatic Sciences,* pp. 2085-2096, 2004.

[42] J. M. Buffington and D. R. Montgomery, "Effects of hydraulic roughness on surface textures of gravel-bed rivers," *Water Resources Research,* vol. 35, no. 11, pp. 3501-3521, 1999.

[43] A. M. Gorman, P. J. Whiting, T. M. Neeson and J. K. Koonce, "Channel substrate prediction from GIS for habitat estimation in Lake Erie tributaries," *Journal of Great Lakes Research,* vol. 37, no. 4, pp. 725-731, 2011.

[44] P. J. Whiting, J. F. Stamm, D. B. Moog and R. L. Orndorff, "Sediment-transporting fl ows in headwater," *Geological Society of America Bulletin,* vol. 111, no. 3, pp. 450-466, 1999.

[45] N. P. Snyder, A. O. Neshemi, B. C. Wilkins and D. A. Edmonds, "Predicting grain size in gravel-bedded rivers using digital elevation models: Application to three Maine watersheds," *Geological Survey of America Bulletin,* vol. 125, pp. 148-163, 2012.

[46] N. P. Snyder, "Studying Stream Morphology With Airborne Laser Elevation Data," *Earth & Space Science News,* vol. 90, no. 6, p. 45–46, 2009.

[47] H. H. Barnes, "Roughness Characteristics of Natural Channels," *U.S. Gelogical Survey Water Supply Paper,* vol. Report 1849, pp. 0-213, 1967.

[48] A. M. Pfeiffer and N. J. Finnegan, "Basin-scale methods for predicting salmonidspawning habitat via grain size and riffle spacing, tested in a California coastal drainage," *Earth Surface Processes and Landform,* vol. 42, no. 6, p. 941–955, 2016.

[49] M. P. Lamb, W. E. Dietritch and J. G. Venditti, "Is the critical Shields stress for incipient sediment motion dependent on channel-bed slope?," *Journal of Geophysical Research,* vol. 113, no. F2, 2008.

[50] Astrium an EADS Company, *Pleiades Imagery User Guide,* 2012.

[51] V. T. Chow, Open-channel hydraulics, New York: McGraw-Hill, 1959.

[52] M. G. Wolman and J. P. Miller, "Magnitude & Frequency of Forces in Geomorphic Processes," *The Journal of Geology,* vol. 68, no. 1, pp. 54-74, 1960.

[53] G. Parker, "Self-formed straight rivers with equilibrium banks and mobile bed. Part 1. The sand-silt river," *Journal of Fluid Mechanics,* vol. 89, no. 1, pp. 109-125, 1978.

[54] E. D. Andrews, "Bed-material entrainment and hydraulic geometry of gravel-bed rivers in Colorado," *Geological Society of America Bulletin,* vol. 95, no. 3, 1984.

[55] E. D. Andrews and J. M. Nankervis, "Effective Discharge and the Design of Channel Maintenance Flows for Gravel-Bed Rivers," in *Natural and Anthropogenic Influences in Fluvial Geomorphology*, Washington, D.C., 1995, pp. 151-164.

[56] F. Petit and A. Pauquet, "Bankfull discharge reccurence interval in gravel-bed rivers," *Earth Surface Processes and Landforms,* pp. 685-693, 1997.

[57] W. W. Emmett and M. G. Wolman, "Effective discharge and gravel-bed rivers," *Earth Surface Processes and Landforms,* pp. 1369-1380, 2001.

[58] J. M. Castro and P. L. Jackson, "Bankfull discharge reccurence intervals and regional hydraulic geometry relationships: patters in the Pacific Northwest, USA," *Journal of American Water Resources Assiciation,* pp. 1249-1262, 2001.

[59] Water Resources Council (U.S.). Hydrology Committee, "Guidelines for determining flood flow frequency," U.S. Water Resources Council, University of California, 1976.

[60] J.-M. Hervouet, Hydrodynamics of Free Surface Flows: Modelling with the Finite Element Method, John Wiley & Sons, 2007.

[61] P. J. Roache, Verification and Validation in Computational Science and Engineering, Albuquerque, New Mexico: Hermosa Publishers, 1998.

[62] J.-S. Bailly, Y. L. Coarer, P. Languille, C.-J. Stigermark and T. Allouis, *Geostatistical estimations of bathymetric LiDAR errors on rivers,* vol. 35, pp. 1199-1210, 2010.

[63] J. A. McKean, D. J. Isaak and C. W. Wright, "Geomorphic controls on salmon nestingpatterns described by a new, narrow-beamterrestrial–aquatic lidar," *Frontiers in Ecology and Environments,* vol. 6, no. 3, pp. 125-130, 2008.

[64] W. E. Dietrich and J. D. Smith, "Influence of the point bar on flow through curved channels," *Water Reseources Research,* vol. 19, no. 5, pp. 1173-1192, 1983.

[65] D. Caamano, P. Goodwin and J. M. Buffington, "Flow Structure Through Pool-Riffle Sequences and a Conceptual Model for Their Sustainability In Gravel-Bed Rivers," *River Research and Applications,* vol. 28, pp. 377-389, 2010.

[66] M. L. MacWilliams, J. M. Wheaton, G. B. Pasternack, R. L. Street and P. K. Kitanidis, "Flow convergence routing hypothesis for pool-riffle maintenance in," *Water Resources Research,* vol. 43, no. 10, 2005.

[67] F. L. Engel and B. L. Rhoads, "Interaction among mean flow, turbulence, bed morphology, bank failures and," *Geomorphology,* vol. 163, pp. 70-83, 2012.

[68] I. Mera, M. J. Franca, J. Anta and E. Pefia, "Turbulence anisotropy in a compound meandering channel with different submergence," *Advances in Water Resource,* vol. 81, pp. 142-151, 2015.

[69] A. N. Sukhodolov, "Structure of turbulent flow in a meander bend of a lowland river," *Water Resources Research,* vol. 48, no. 1, 2012.

[70] R. G. Jackson, "Velocity-bed-form-texture pattern of meander bends in the lower Wabash River of Illinois and Indiana," *Geological Society of America Bulletin,* vol. 86, pp. 1511-1522, 1975.

APPENDIX I a

Sensitivity of flow depth to constant stage gaps: h=variable

Sub-patch #	Sub-patch Flow Depth					Monotonic	dh/d(Δh)
	Δh= 0m	Δh= 0.1m	Δh= 0.25m	Δh= 0.40m	Δh= 0.75m		
	[m/s]	[m/s]	[m/s]	[m/s]	[m/s]		
1	2.8714	2.9087	2.9662	3.0305	3.1742	1	-
2	2.6289	2.666	2.7235	2.7883	2.9328	1	-
3	2.8203	2.8578	2.916	2.9819	3.1288	1	-
4	2.7281	2.7652	2.8226	2.8881	3.033	1	-
5	2.6619	2.6989	2.7564	2.8229	2.9705	1	-
6	2.7116	2.7489	2.8066	2.8736	3.0219	1	-
7	2.53	2.5366	2.5484	2.5692	2.6099	1	-
8	2.6953	2.7323	2.7899	2.8576	3.0068	1	-
9	2.5553	2.5893	2.6428	2.708	2.8492	1	-
10	2.7069	2.7391	2.7901	2.8551	2.994	1	-
11	2.4434	2.4762	2.5282	2.5947	2.7354	1	-
12	3.2082	3.2395	3.3006	3.3936	3.5628	1	-
13	3.269	3.3006	3.3624	3.4569	3.6283	1	-
14	3.2602	3.2915	3.3536	3.4496	3.6226	1	-
15	3.4541	3.4856	3.548	3.6448	3.8191	1	-
16	3.2338	3.2646	3.3271	3.4251	3.5998	1	-
17	3.3548	3.3841	3.4453	3.5446	3.7183	1	-
18	3.3164	3.3469	3.4105	3.5134	3.693	1	-
19	3.6101	3.6395	3.7024	3.8067	3.9859	1	-
20	3.3211	3.3497	3.4127	3.5194	3.7017	1	-
21	3.532	3.5617	3.6273	3.7377	3.9254	1	-
22	3.6302	3.6603	3.7265	3.8381	4.0274	1	-
23	3.3385	3.3666	3.431	3.5429	3.7293	1	-
24	3.3302	3.3605	3.4286	3.5454	3.7408	1	-
25	3.553	3.5832	3.6533	3.7712	3.9675	1	-
26	3.579	3.6097	3.6809	3.8015	4.0014	1	-
27	3.8498	3.88	3.9509	4.0726	4.273	1	-
28	3.7521	3.7774	3.841	3.9555	4.139	1	-
29	3.9448	3.9748	4.0468	4.1711	4.374	1	-
30	4.4601	4.49	4.5624	4.688	4.8922	1	-
31	4.5655	4.5954	4.668	4.7941	4.9988	1	-
32	4.5458	4.5758	4.6483	4.7745	4.9795	1	-

APPENDIX I b

Sensitivity of friction velocity to constant stage gaps: Δh=variable

Sub-patch #	Sub-patch Friction Velocity					Monotonic	$du_*/d(\Delta h)$
	Δh= 0m	Δh= 0.1m	Δh= 0.25m	Δh= 0.40m	Δh= 0.75m		
	[m/s]	[m/s]	[m/s]	[m/s]	[m/s]		
1	0.096632	0.096177	0.09566	0.094723	0.092978	1	-
2	0.074156	0.074414	0.074572	0.074535	0.074463	0	+/-
3	0.083587	0.083051	0.082085	0.080607	0.077688	1	-
4	0.11045	0.11106	0.11201	0.1125	0.11465	1	+
5	0.11001	0.11035	0.11092	0.11078	0.11062	0	+/-
6	0.11102	0.11118	0.1115	0.11108	0.11028	0	+/-
7	0.019239	0.0169	0.013285	0.010082	0.0042733	1	-
8	0.10956	0.11009	0.11082	0.11066	0.11059	0	+/-
9	0.11027	0.11293	0.11678	0.11984	0.12794	1	+
10	0.11072	0.11188	0.11337	0.11365	0.11517	1	+
11	0.081118	0.078315	0.074042	0.068985	0.057061	1	-
12	0.091359	0.090896	0.089849	0.088566	0.08569	1	-
13	0.066067	0.065963	0.065393	0.064049	0.062117	1	-
14	0.075805	0.076209	0.076183	0.074795	0.073392	0	+/-
15	0.056305	0.056286	0.055829	0.05473	0.052629	1	-
16	0.034608	0.034337	0.034208	0.032877	0.031767	1	-
17	0.080746	0.081943	0.082937	0.082252	0.082919	0	+/-
18	0.085284	0.084483	0.082728	0.079771	0.075082	1	-
19	0.085013	0.086071	0.086787	0.085714	0.085756	0	+/-
20	0.065709	0.065738	0.065006	0.062921	0.059586	0	+/-
21	0.08623	0.086028	0.084796	0.082356	0.078787	1	-
22	0.060913	0.060722	0.060087	0.058714	0.056762	1	-
23	0.097661	0.097589	0.096589	0.094123	0.090507	1	-
24	0.0841	0.08401	0.083183	0.08087	0.077772	1	-
25	0.071061	0.071422	0.069651	0.068371	0.067484	0	+/-
26	0.077797	0.076959	0.075448	0.072799	0.069184	1	-
27	0.066517	0.066216	0.065251	0.063326	0.060337	1	-
28	0.013892	0.013302	0.011908	0.010012	0.0074781	1	-
29	0.061355	0.061119	0.060331	0.058521	0.056028	1	-
30	0.058424	0.058307	0.057649	0.056199	0.054251	1	-
31	0.044244	0.044122	0.043483	0.04214	0.040316	1	-
32	0.049184	0.049232	0.048985	0.047881	0.046538	0	+/-

APPENDIX II a

Mesh Analysis Results for COARSE (dx=2m)

NodeCount: 286293
Edge Nodes: 10517
Interior Nodes: 275776

Edge Node Connectivity:
Minimum number of neighbours: 2
Maximum number of neighbours: 5
< 4 neighbours: 66
4-6 neighbours: 10451

Interior Node Connectivity:
Minimum number of neighbours: 5
Maximum number of neighbours: 7
5-7 neighbours: 275776

ElementCount: 562067
Interior Elements: 551553
Normal Edge Elements: 10511
Over constrained Elements: 3

Element Node ordering:
Counter-Clockwise Elements: 562067
Clockwise Elements: 0

Minimum Element Area: 1.342638
Maximum Element Area: 2.642221
Mean Element Area: 2.000864
Area Distribution:
10 Percentile: 38
20 Percentile: 33
30 Percentile: 22
40 Percentile: 13
50 Percentile: 4849
60 Percentile: 557063
70 Percentile: 25
80 Percentile: 8
90 Percentile: 8
100 Percentile: 8

Element Shape Characterization:
Elements with Angle 90-135 : 79
Elements with Angle 30-90 : 561988

Number of Exterior Element Edges: 10517
Minimum Exterior Edge Length: 1.545013
Maximum Exterior Edge Length: 2.004635
Mean Exterior Edge Length: 1.999661

Exterior Edge Length Distribution:
10 Percentile: 3
20 Percentile: 0
30 Percentile: 1
40 Percentile: 3
50 Percentile: 1
60 Percentile: 1
70 Percentile: 0
80 Percentile: 2
90 Percentile: 3
100 Percentile: 10503

Number of Interior Element Edges: 837842
Minimum Interior Edge Length: 1.342643
Maximum Interior Edge Length: 3.051587
Mean Interior Edge Length: 2.202529
Interior Edge Length Distribution:
10 Percentile: 24
20 Percentile: 20
30 Percentile: 5
40 Percentile: 379182
50 Percentile: 155014
60 Percentile: 85316
70 Percentile: 76261
80 Percentile: 91395
90 Percentile: 50617
100 Percentile: 8

APPENDIX II b

Mesh Analysis Results for MEDIUM (dx=1m)

NodeCount: 1134639
Edge Nodes: 21033
Interior Nodes: 1113606

Edge Node Connectivity:
Minimum number of neighbours: 2
Maximum number of neighbours: 5
< 4 neighbours: 82
4-6 neighbours: 20951

Interior Node Connectivity:
Minimum number of neighbours: 4
Maximum number of neighbours: 7
= 4 neighbours: 1
5-7 neighbours: 1113605

ElementCount: 2248243
Interior Elements: 2227211
Normal Edge Elements: 21031
Over constrained Elements: 1

Element Node ordering:
Counter-Clockwise Elements: 2248243
Clockwise Elements: 0

Minimum Element Area: 0.333939
Maximum Element Area: 0.663117
Mean Element Area: 0.500222
Area Distribution:
10 Percentile: 66
20 Percentile: 74
30 Percentile: 42
40 Percentile: 52
50 Percentile: 8821
60 Percentile: 2239115
70 Percentile: 26
80 Percentile: 17
90 Percentile: 12
100 Percentile: 18

Element Shape Characterization:
Elements with Angle 90-135 : 295
Elements with Angle 30-90 : 2247948

Number of Exterior Element Edges: 21033
Minimum Exterior Edge Length: 0.766025
Maximum Exterior Edge Length: 1.169114

Mean Exterior Edge Length: 0.999948
Exterior Edge Length Distribution:
10 Percentile: 4
20 Percentile: 0
30 Percentile: 0
40 Percentile: 0
50 Percentile: 8
60 Percentile: 21020
70 Percentile: 0
80 Percentile: 0
90 Percentile: 0
100 Percentile: 1

Number of Interior Element Edges: 3361848
Minimum Interior Edge Length: 0.667879
Maximum Interior Edge Length: 1.529530
Mean Interior Edge Length: 1.100950
Interior Edge Length Distribution:
10 Percentile: 44
20 Percentile: 43
30 Percentile: 8

APPENDIX II b

Mesh Analysis Results for FINE (dx=0.5m)

NodeCount: 4517503
Edge Nodes: 42066
Interior Nodes: 4475437

Edge Node Connectivity:
Minimum number of neighbours: 2
Maximum number of neighbours: 5
< 4 neighbours: 107
4-6 neighbours: 41959

Interior Node Connectivity:
Minimum number of neighbours: 5
Maximum number of neighbours: 7
5-7 neighbours: 4475437

ElementCount: 8992938
Interior Elements: 8950874
Normal Edge Elements: 42062
Over constrained Elements: 2

Element Node ordering:
Counter-Clockwise Elements: 8992938
Clockwise Elements: 0

Minimum Element Area: 0.083709
Maximum Element Area: 0.165030
Mean Element Area: 0.125056
Area Distribution:
10 Percentile: 142
20 Percentile: 142
30 Percentile: 98
40 Percentile: 169
50 Percentile: 6297
60 Percentile: 8985955
70 Percentile: 42
80 Percentile: 36
90 Percentile: 23
100 Percentile: 34

Element Shape Characterization:
Elements with Angle 90-135 : 1099
Elements with Angle 30-90 : 8991839

Number of Exterior Element Edges: 42066
Minimum Exterior Edge Length: 0.347636
Maximum Exterior Edge Length: 0.620887
Mean Exterior Edge Length: 0.499990

Exterior Edge Length Distribution:
10 Percentile: 2
20 Percentile: 1
30 Percentile: 0
40 Percentile: 1
50 Percentile: 6
60 Percentile: 42055
70 Percentile: 0
80 Percentile: 0
90 Percentile: 0
100 Percentile: 1

Number of Interior Element Edges: 13468374
Minimum Interior Edge Length: 0.334836
Maximum Interior Edge Length: 0.762456
Mean Interior Edge Length: 0.550397
Interior Edge Length Distribution:
10 Percentile: 98
20 Percentile: 84
30 Percentile: 21
40 Percentile: 5996738
50 Percentile: 2595112
60 Percentile: 1368293
70 Percentile: 1224799
80 Percentile: 1455039
90 Percentile: 828161
100 Percentile: 29

APPENDIX III a

Sensitivity of flow depth to mesh size: dx=2m, dt=0.25s, IC=variable

Sub-patch #	Sub-patch Flow Depth			MAEN	VAR	STD
	IC1	IC2	IC3			
	[m]	[m]	[m]			
1	3.0825	3.0824	3.0825	3.082467	1.75E-09	4.18E-05
2	2.8524	2.8523	2.8523	2.852333	2.01E-09	4.48E-05
3	3.0404	3.0403	3.0403	3.040333	2.33E-09	4.82E-05
4	2.941	2.9408	2.9409	2.9409	2.78E-09	5.27E-05
5	2.8716	2.8714	2.8715	2.8715	3.42E-09	5.85E-05
6	2.9209	2.9207	2.9208	2.9208	3.55E-09	5.95E-05
7	2.522	2.5218	2.5219	2.5219	3.48E-09	5.90E-05
8	2.8899	2.8897	2.8898	2.8898	4.68E-09	6.84E-05
9	2.7122	2.712	2.7121	2.7121	1.19E-08	0.000109
10	2.7983	2.7979	2.7981	2.7981	2.17E-08	0.000147
11	2.4998	2.4994	2.4997	2.499633	3.37E-08	0.000184
12	2.9485	2.947	2.9483	2.947933	4.29E-07	0.000655
13	2.9903	2.9892	2.9901	2.989867	2.16E-07	0.000464
14	2.9598	2.9591	2.9596	2.9595	9.97E-08	0.000316
15	3.1703	3.1695	3.1701	3.169967	1.12E-07	0.000335
16	2.8723	2.8716	2.8721	2.872	8.89E-08	0.000298
17	2.9512	2.9504	2.951	2.950867	1.24E-07	0.000352
18	2.8981	2.8971	2.8979	2.8977	1.70E-07	0.000413
19	3.0799	3.0786	3.0797	3.0794	3.18E-07	0.000564
20	2.7342	2.7326	2.734	2.7336	5.15E-07	0.000718
21	2.8532	2.8512	2.8529	2.852433	7.92E-07	0.00089
22	2.94	2.938	2.9397	2.939233	8.01E-07	0.000895
23	2.506	2.5033	2.5057	2.505	1.37E-06	0.001172
24	2.5458	2.543	2.5455	2.544767	1.50E-06	0.001226
25	2.5964	2.5947	2.5963	2.5958	5.72E-07	0.000756
26	2.613	2.6119	2.6128	2.612567	2.42E-07	0.000492
27	2.724	2.7242	2.7238	2.724	2.89E-08	0.00017
28	2.5522	2.5525	2.5521	2.552267	3.24E-08	0.00018
29	2.4338	2.4342	2.4337	2.4339	4.87E-08	0.000221
30	2.5712	2.5717	2.571	2.5713	9.05E-08	0.000301
31	2.6029	2.6035	2.6028	2.603067	8.59E-08	0.000293
32	2.5805	2.581	2.5804	2.580633	8.97E-08	0.0003

APPENDIX III b

Sensitivity of flow depth to mesh size: dx=1m, dt=0.25s, IC=variable

Sub-patch #	Sub-patch Flow Depth			MAEN	VAR	STD
	IC1	IC2	IC3			
	[m]	[m]	[m]			
1	3.0826	3.0827	3.0825	3.0826	1.18E-08	1.08E-04
2	2.8524	2.8526	2.8523	2.852433	1.22E-08	1.10E-04
3	3.0404	3.0406	3.0403	3.040433	1.29E-08	1.14E-04
4	2.9409	2.9411	2.9409	2.940967	8.53E-09	9.24E-05
5	2.8717	2.8719	2.8715	2.8717	2.68E-08	1.64E-04
6	2.9211	2.9213	2.9208	2.921067	4.53E-08	2.13E-04
7	2.5221	2.5223	2.5219	2.5221	2.52E-08	1.59E-04
8	2.8898	2.89	2.8898	2.889867	8.54E-09	9.24E-05
9	2.7124	2.7125	2.7121	2.712333	3.28E-08	0.000181
10	2.7988	2.799	2.7981	2.798633	1.44E-07	0.00038
11	2.4998	2.5	2.4997	2.499833	1.44E-08	0.00012
12	2.9484	2.9488	2.9483	2.9485	3.81E-08	0.000195
13	2.9902	2.9906	2.9901	2.9903	4.31E-08	0.000208
14	2.9599	2.9602	2.9596	2.9599	5.78E-08	0.00024
15	3.1702	3.1705	3.1701	3.170267	3.08E-08	0.000176
16	2.8721	2.8725	2.8721	2.872233	3.10E-08	0.000176
17	2.9513	2.9517	2.951	2.951333	8.24E-08	0.000287
18	2.8982	2.8986	2.8979	2.898233	8.05E-08	0.000284
19	3.08	3.0804	3.0797	3.080033	8.47E-08	0.000291
20	2.734	2.7344	2.734	2.734133	3.54E-08	0.000188
21	2.8528	2.8532	2.8529	2.852967	2.96E-08	0.000172
22	2.9397	2.9401	2.9397	2.939833	3.16E-08	0.000178
23	2.5071	2.5075	2.5057	2.506767	6.08E-07	0.000779
24	2.5461	2.5465	2.5455	2.546033	1.88E-07	0.000433
25	2.5967	2.5971	2.5963	2.5967	1.16E-07	0.000341
26	2.6135	2.6138	2.6128	2.613367	1.71E-07	0.000414
27	2.7247	2.7251	2.7238	2.724533	2.70E-07	0.00052
28	2.5531	2.5535	2.5521	2.5529	3.59E-07	0.000599
29	2.4344	2.4348	2.4337	2.4343	2.18E-07	0.000467
30	2.5711	2.5716	2.571	2.571233	5.37E-08	0.000232
31	2.6029	2.6034	2.6028	2.603033	6.24E-08	0.00025
32	2.5805	2.581	2.5804	2.580633	8.04E-08	0.000284

APPENDIX III c

Sensitivity of friction velocity to mesh size: dx=2m, dt=0.25s, IC=variable

Sub-patch #	Sub-patch Friction Velocity			MEAN	VAR	STD
	IC1	IC2	IC3			
	[m/s]	[m/s]	[m/s]			
1	0.095872	0.095948	0.095882	0.095901	1.13E-09	3.36E-05
2	0.077787	0.077786	0.07779	0.077788	2.57E-12	1.60E-06
3	0.081326	0.081334	0.08133	0.08133	9.53E-12	3.09E-06
4	0.12172	0.12174	0.12173	0.12173	3.81E-11	6.18E-06
5	0.1168	0.11682	0.11681	0.11681	3.45E-11	5.87E-06
6	0.1158	0.11581	0.1158	0.115803	2.96E-11	5.44E-06
7	0.005172	0.005174	0.005173	0.005173	7.66E-13	8.75E-07
8	0.1177	0.11772	0.1177	0.117707	6.35E-11	7.97E-06
9	0.14298	0.14302	0.14299	0.142997	3.32E-10	1.82E-05
10	0.12725	0.12729	0.12726	0.127267	3.05E-10	1.75E-05
11	0.060849	0.060861	0.060896	0.060869	3.90E-10	1.98E-05
12	0.10936	0.10961	0.10936	0.109443	1.34E-08	0.000116
13	0.081949	0.082939	0.081951	0.08228	2.17E-07	0.000466
14	0.10264	0.10337	0.10265	0.102887	1.18E-07	0.000343
15	0.06104	0.061067	0.061039	0.061049	1.71E-10	1.31E-05
16	0.060769	0.060608	0.060779	0.060719	6.17E-09	7.86E-05
17	0.12938	0.12947	0.12939	0.129413	1.48E-09	3.84E-05
18	0.10759	0.10767	0.10759	0.107617	1.32E-09	3.63E-05
19	0.1353	0.13543	0.13531	0.135347	3.48E-09	5.90E-05
20	0.087093	0.087173	0.087094	0.08712	1.39E-09	3.73E-05
21	0.12488	0.12504	0.12488	0.124933	5.85E-09	7.65E-05
22	0.082579	0.082621	0.082572	0.082591	4.68E-10	2.16E-05
23	0.14868	0.14894	0.14869	0.14877	1.53E-08	0.000124
24	0.13111	0.13101	0.13107	0.131063	1.47E-09	3.83E-05
25	0.13389	0.13379	0.13383	0.133837	1.55E-09	3.93E-05
26	0.11398	0.11505	0.11398	0.114337	2.57E-07	0.000507
27	0.11535	0.11771	0.11535	0.116137	1.24E-06	0.001112
28	0.035265	0.034722	0.035264	0.035084	6.53E-08	0.000256
29	0.11433	0.11406	0.11433	0.11424	1.63E-08	0.000128
30	0.1434	0.14339	0.14338	0.14339	5.49E-11	7.41E-06
31	0.10219	0.10221	0.10221	0.102203	1.01E-10	1.01E-05
32	0.11056	0.11057	0.11058	0.11057	9.41E-11	9.70E-06

APPENDIX III d

Sensitivity of friction velocity to mesh size: dx=1m, dt=0.25s, IC=variable

Sub-patch #	Sub-patch Friction Velocity			MEAN	VAR	STD
	IC1	IC2	IC3			
	[m/s]	[m/s]	[m/s]			
1	0.095854	0.09585	0.095882	0.095862	2.03E-10	1.42E-05
2	0.077793	0.077792	0.07779	0.077792	1.91E-12	1.38E-06
3	0.081363	0.081358	0.08133	0.08135	2.07E-10	1.44E-05
4	0.12173	0.12173	0.12173	0.12173	1.21E-11	3.48E-06
5	0.11678	0.11678	0.11681	0.11679	1.83E-10	1.35E-05
6	0.11577	0.11576	0.1158	0.115777	2.49E-10	1.58E-05
7	0.005112	0.005109	0.005173	0.005131	8.75E-10	2.96E-05
8	0.11775	0.11774	0.1177	0.11773	3.09E-10	1.76E-05
9	0.143	0.143	0.14299	0.142997	3.74E-11	6.12E-06
10	0.12709	0.12708	0.12726	0.127143	7.06E-09	8.40E-05
11	0.060988	0.060992	0.060896	0.060959	1.98E-09	4.45E-05
12	0.10939	0.10939	0.10936	0.10938	1.84E-10	1.36E-05
13	0.081978	0.081979	0.081951	0.081969	1.70E-10	1.30E-05
14	0.10264	0.10264	0.10265	0.102643	5.17E-12	2.27E-06
15	0.060989	0.060995	0.061039	0.061008	4.99E-10	2.23E-05
16	0.060833	0.060819	0.060779	0.06081	5.21E-10	2.28E-05
17	0.1294	0.1294	0.12939	0.129397	1.36E-11	3.69E-06
18	0.10749	0.1075	0.10759	0.107527	2.01E-09	4.48E-05
19	0.13534	0.13534	0.13531	0.13533	1.80E-10	1.34E-05
20	0.087132	0.08714	0.087094	0.087122	4.00E-10	2.00E-05
21	0.12489	0.1249	0.12488	0.12489	2.91E-11	5.39E-06
22	0.082627	0.082636	0.082572	0.082612	8.03E-10	2.83E-05
23	0.14823	0.14824	0.14869	0.148387	4.57E-08	0.000214
24	0.13109	0.1311	0.13107	0.131087	1.78E-10	1.33E-05
25	0.1339	0.13391	0.13383	0.13388	1.27E-09	3.56E-05
26	0.11391	0.11393	0.11398	0.11394	7.81E-10	2.79E-05
27	0.11525	0.11526	0.11535	0.115287	2.03E-09	4.51E-05
28	0.035213	0.035213	0.035264	0.03523	5.84E-10	2.42E-05
29	0.11455	0.11456	0.11433	0.11448	1.17E-08	0.000108
30	0.14353	0.14354	0.14338	0.143483	5.33E-09	7.30E-05
31	0.10206	0.10208	0.10221	0.102117	4.40E-09	6.63E-05
32	0.11056	0.11057	0.11058	0.11057	5.61E-11	7.49E-06

APPENDIX IV a

Sensitivity of flow depth to mesh size: dx=variable, dt=0.1s, IC=1

Sub-patch #	Sub-patch Flow Depth			MEAN	VAR	STD	Monotonic AND Converging	Richardson Extrapolate	Error	Convergence Range
	Coarse	Medium	Fine							
	[m]	[m]	[m]						[%]	
1	3.0826	3.0697	3.059	3.0704	9.3E-05	0.009643	1	3.0082	2.0764	0.99652
2	2.8524	2.8304	2.8208	2.8345	0.000176	0.013248	1	2.8134	0.32741	0.99661
3	3.0404	3.0173	3.0093	3.0224	0.000174	0.013174	1	3.0051	0.17618	0.99735
4	2.9409	2.9149	2.9064	2.9208	0.000216	0.014695	1	2.9022	0.17994	0.99707
5	2.8717	2.848	2.8379	2.8526	0.0002	0.014156	1	2.8305	0.32922	0.99646
6	2.9211	2.8962	2.887	2.9014	0.000208	0.014416	1	2.8817	0.2312	0.99683
7	2.5221	2.4142	2.4155	2.4506	0.002556	0.050556	0	-	-	-
8	2.8898	2.8666	2.858	2.8715	0.000181	0.013437	1	2.8528	0.226	0.99698
9	2.7124	2.684	2.68	2.6921	0.000207	0.014392	1	2.6794	0.030666	0.99851
10	2.7988	2.7795	2.773	2.7838	0.00012	0.010965	1	2.7696	0.15144	0.99765
11	2.4998	2.4857	2.4967	2.494	3.64E-05	0.006035	0	-	-	-
12	2.9484	2.9239	2.9172	2.9298	0.000181	0.013445	1	2.9147	0.10708	0.99771
13	2.9902	2.9668	2.9563	2.9711	0.000201	0.014172	1	2.9479	0.35842	0.99647
14	2.9599	2.9372	2.928	2.9417	0.00018	0.013406	1	2.9216	0.26963	0.99686
15	3.1702	3.1492	3.1456	3.155	0.000117	0.010827	1	3.1448	0.030442	0.99884
16	2.8721	2.8483	2.8413	2.8539	0.000175	0.013217	1	2.8383	0.12821	0.99754
17	2.9513	2.9268	2.9185	2.9322	0.000194	0.013926	1	2.9143	0.1806	0.99717
18	2.8982	2.872	2.8639	2.878	0.000214	0.014644	1	2.8604	0.15502	0.9972
19	3.08	3.0549	3.0464	3.0604	0.000204	0.014267	1	3.042	0.17932	0.99721
20	2.734	2.7001	2.6861	2.7067	0.000404	0.020111	1	2.6761	0.4636	0.9948
21	2.8528	2.8302	2.8226	2.8352	0.000164	0.012811	1	2.8189	0.16571	0.99734
22	2.9397	2.9165	2.9078	2.9213	0.000181	0.013453	1	2.9026	0.22498	0.99702
23	2.5071	2.4713	2.4808	2.4864	0.000229	0.015125	0	-	-	-
24	2.5461	2.4831	2.4901	2.5064	0.000797	0.028227	0	-	-	-
25	2.5967	2.5796	2.5772	2.5845	7.51E-05	0.008668	1	2.5769	0.018798	0.99907
26	2.6135	2.6023	2.5917	2.6025	7.89E-05	0.008884	1	2.3967	9.4067	0.99593
27	2.7247	2.7034	2.6981	2.7087	0.000132	0.011489	1	2.6964	0.081494	0.99804
28	2.5531	2.5596	2.5166	2.5431	0.000358	0.018911	0	-	-	-
29	2.4344	2.4154	2.4164	2.422	7.62E-05	0.008729	0	-	-	-
30	2.5711	2.57	2.5696	2.5702	3.78E-07	0.000615	1	2.5693	0.013004	0.99984
31	2.6029	2.6057	2.6088	2.6058	5.64E-06	0.002376	0	-	-	-
32	2.5805	2.5828	2.5821	2.5818	9.01E-07	0.000949	0	-	-	-

APPENDIX IV b

Sensitivity of flow depth to mesh size: dx=variable, dt=0.05s, IC=1

Sub-patch #	Sub-patch Flow Depth			MEAN	VAR	STD	Monotonic AND Converging	Richardson Extrapolate	Error	Convergence Range
	Coarse	Medium	Fine							
	[m]	[m]	[m]						[%]	
1	3.0827	3.07	3.0591	3.0706	9.31E-05	0.009647	1	2.9889	2.8664	0.99643
2	2.8525	2.8307	2.8209	2.8347	0.000175	0.013224	1	2.8129	0.3528	0.99654
3	3.0405	3.0176	3.0094	3.0225	0.000174	0.013182	1	3.0048	0.18891	0.99728
4	2.941	2.9152	2.9064	2.9209	0.000215	0.01466	1	2.9019	0.19419	0.99699
5	2.8718	2.8483	2.838	2.8527	0.000201	0.014168	1	2.83	0.35055	0.99639
6	2.9213	2.8965	2.8871	2.9016	0.000209	0.014446	1	2.8813	0.24822	0.99675
7	2.5222	2.4145	2.4156	2.4507	0.002553	0.050532	0	-	-	-
8	2.8898	2.867	2.858	2.8716	0.000179	0.013388	1	2.8523	0.25144	0.99688
9	2.7125	2.6843	2.6801	2.6923	0.000207	0.014387	1	2.6793	0.034589	0.99843
10	2.7991	2.7798	2.773	2.784	0.000122	0.011042	1	2.7694	0.16411	0.99757
11	2.4998	2.486	2.4967	2.4942	3.53E-05	0.005939	0	-	-	-
12	2.9485	2.9243	2.9173	2.93	0.000179	0.013378	1	2.9144	0.12382	0.99759
13	2.9903	2.9673	2.9565	2.9714	0.0002	0.014129	1	2.9469	0.40329	0.99636
14	2.96	2.9377	2.928	2.9419	0.00018	0.013408	1	2.9208	0.30892	0.99673
15	3.1702	3.1497	3.1457	3.1552	0.000115	0.010717	1	3.1447	0.038481	0.99873
16	2.872	2.8487	2.8414	2.854	0.00017	0.013043	1	2.838	0.15004	0.99742
17	2.9514	2.9273	2.9187	2.9325	0.000192	0.013868	1	2.9138	0.20712	0.99704
18	2.8984	2.8723	2.864	2.8782	0.000214	0.014642	1	2.8601	0.17078	0.9971
19	3.0802	3.0555	3.0466	3.0608	0.000202	0.014198	1	3.0416	0.20752	0.99708
20	2.7339	2.7007	2.6863	2.707	0.000398	0.019954	1	2.6752	0.51529	0.99466
21	2.8527	2.8308	2.8229	2.8354	0.000159	0.012594	1	2.8184	0.19632	0.99722
22	2.9396	2.9171	2.908	2.9216	0.000176	0.013277	1	2.9019	0.26245	0.99689
23	2.5078	2.4718	2.481	2.4869	0.000233	0.015273	0	-	-	-
24	2.5462	2.4836	2.4903	2.5067	0.000789	0.028087	0	-	-	-
25	2.5968	2.5802	2.5774	2.5848	7.29E-05	0.008539	1	2.5769	0.027322	0.99892
26	2.6136	2.603	2.5919	2.6028	7.88E-05	0.008878	0	-	-	-
27	2.725	2.704	2.6983	2.7091	0.000131	0.011464	1	2.6962	0.09749	0.9979
28	2.5534	2.56	2.5168	2.5434	0.000362	0.019016	0	-	-	-
29	2.4346	2.4157	2.4166	2.4223	7.57E-05	0.0087	0	-	-	-
30	2.5711	2.5701	2.5697	2.5703	3.78E-07	0.000614	1	2.5695	0.010668	0.99985
31	2.603	2.6059	2.6088	2.6059	5.59E-06	0.002364	0	-	-	-
32	2.5806	2.5827	2.5821	2.5818	8.05E-07	0.000897	0	-	-	-

APPENDIX IV c

Sensitivity of friction velocity to mesh size: dx=variable, dt=0.1s, IC=1

Sub-patch #	Sub-patch Friction Velocity			MEAN	VAR	STD	Monotonic AND Converging	Richardson Extrapolate	Error	Convergence Range
	Coarse	Medium	Fine							
	[m/s]	[m/s]	[m/s]						[%]	
1	0.095854	0.098391	0.097971	0.097405	1.23E-06	0.00111	0	-	-	-
2	0.077793	0.077617	0.07746	0.077623	1.85E-08	0.000136	1	0.076177	2.0708	0.99798
3	0.081363	0.0817	0.082303	0.081789	1.51E-07	0.000389	0	-	-	-
4	0.12173	0.12296	0.12346	0.12272	5.27E-07	0.000726	1	0.1238	0.34277	1.004
5	0.11678	0.11798	0.11844	0.11773	4.86E-07	0.000697	1	0.11872	0.30009	1.0039
6	0.11577	0.1182	0.11925	0.11774	2.13E-06	0.00146	1	0.12007	0.84982	1.0089
7	0.005112	0.004116	0.00355	0.004259	4.17E-07	0.000646	1	0.0028016	26.351	0.86238
8	0.11775	0.11959	0.12044	0.11926	1.27E-06	0.001125	1	0.12116	0.74559	1.0071
9	0.143	0.14528	0.14579	0.14469	1.46E-06	0.00121	1	0.14594	0.12742	1.0035
10	0.12709	0.12905	0.12965	0.12859	1.2E-06	0.001095	1	0.12992	0.25879	1.0047
11	0.060988	0.061204	0.060086	0.060759	2.35E-07	0.000485	0	-	-	-
12	0.10939	0.11041	0.11097	0.11026	4.25E-07	0.000652	1	0.11163	0.74269	1.005
13	0.081978	0.083192	0.083919	0.08303	6.41E-07	0.000801	1	0.085006	1.6185	1.0087
14	0.10264	0.10437	0.10547	0.10416	1.35E-06	0.001164	1	0.10742	2.3122	1.0106
15	0.060989	0.06261	0.063832	0.062477	1.36E-06	0.001165	1	0.067575	7.3283	1.0195
16	0.060833	0.061617	0.062635	0.061695	5.44E-07	0.000738	0	-	-	-
17	0.1294	0.13075	0.13113	0.13043	5.55E-07	0.000745	1	0.13128	0.13843	1.0029
18	0.10749	0.10727	0.10695	0.10724	4.91E-08	0.000222	0	0	0	0
19	0.13534	0.13795	0.13851	0.13726	1.91E-06	0.001383	1	0.13867	0.14111	1.0041
20	0.087132	0.088122	0.087982	0.087745	1.91E-07	0.000437	0	-	-	-
21	0.12489	0.12563	0.12639	0.12564	3.76E-07	0.000613	0	-	-	-
22	0.082627	0.081855	0.08184	0.082107	1.35E-07	0.000367	1	0.08184	0.000453	0.99982
23	0.14823	0.15246	0.15512	0.15194	8.05E-06	0.002837	1	0.15956	3.5785	1.0174
24	0.13109	0.1306	0.13135	0.13102	9.76E-08	0.000312	0	-	-	-
25	0.1339	0.13416	0.13501	0.13436	2.25E-07	0.000474	0	-	-	-
26	0.11391	0.11709	0.11751	0.11617	2.58E-06	0.001608	1	0.11758	0.070147	1.0036
27	0.11525	0.11899	0.12042	0.11822	4.75E-06	0.002179	1	0.1213	0.92207	1.012
28	0.035213	0.036702	0.03754	0.036485	9.26E-07	0.000962	1	0.038615	3.5811	1.0228
29	0.11455	0.11524	0.1152	0.115	9.99E-08	0.000316	0	-	-	-
30	0.14353	0.14322	0.14262	0.14312	1.41E-07	0.000376	0	-	-	-
31	0.10206	0.10151	0.10025	0.10127	5.76E-07	0.000759	0	-	-	-
32	0.11056	0.11095	0.11117	0.11089	6.27E-08	0.00025	1	0.11148	0.34775	1.002

APPENDIX IV d

Sensitivity of friction velocity to mesh size: dx=variable, dt=0.05s, IC=1

Sub-patch #	Sub-patch Friction Velocity			MEAN	VAR	STD	Monotonic AND Converging	Richardson Extrapolate	Error	Convergence Range
	Coarse [m/s]	Medium [m/s]	Fine [m/s]						[%]	
1	0.095798	0.098302	0.09796	0.097353	1.23E-06	0.001108	0	-	-	-
2	0.077797	0.077625	0.077465	0.077629	1.84E-08	0.000136	1	0.075283	3.5213	0.99794
3	0.08138	0.081685	0.082305	0.08179	1.48E-07	0.000385	0	-	-	-
4	0.12173	0.12296	0.12347	0.12272	5.34E-07	0.000731	1	0.12382	0.35592	1.0041
5	0.11678	0.11798	0.11844	0.11773	4.92E-07	0.000702	1	0.11873	0.30548	1.0039
6	0.11576	0.11817	0.11924	0.11773	2.12E-06	0.001455	1	0.1201	0.89337	1.009
7	0.005077	0.004122	0.003556	0.004251	3.94E-07	0.000628	1	0.0027352	28.853	0.8628
8	0.11775	0.11957	0.12045	0.11926	1.26E-06	0.001123	1	0.12127	0.84937	1.0073
9	0.14301	0.1453	0.14579	0.1447	1.47E-06	0.001211	1	0.14593	0.11991	1.0034
10	0.12701	0.12902	0.12965	0.12856	1.26E-06	0.001125	1	0.12994	0.27805	1.0049
11	0.0611	0.061211	0.060096	0.060802	2.51E-07	0.000501	0	-	-	-
12	0.10939	0.11037	0.11096	0.11024	4.16E-07	0.000645	1	0.11185	1.0025	1.0053
13	0.081987	0.083187	0.083924	0.083033	6.37E-07	0.000798	1	0.0851	1.7524	1.0089
14	0.10263	0.10435	0.10548	0.10415	1.38E-06	0.001173	1	0.10762	2.533	1.0108
15	0.060953	0.062573	0.063825	0.06245	1.38E-06	0.001176	1	0.068057	8.2883	1.02
16	0.060847	0.061631	0.062692	0.061724	5.72E-07	0.000756	0	-	-	-
17	0.1294	0.13074	0.13112	0.13042	5.46E-07	0.000739	1	0.13128	0.14747	1.0029
18	0.10745	0.10716	0.10688	0.10717	5.44E-08	0.000233	1	0.099493	8.6427	0.99738
19	0.13536	0.13788	0.1385	0.13724	1.85E-06	0.001359	1	0.13869	0.17942	1.0045
20	0.087114	0.088055	0.087984	0.087718	1.83E-07	0.000428	0	-	-	-
21	0.12489	0.12563	0.12638	0.12563	3.71E-07	0.000609	0	-	-	-
22	0.082652	0.081856	0.081847	0.082118	1.42E-07	0.000377	1	0.081847	0.000169	0.99989
23	0.148	0.15244	0.15512	0.15185	8.63E-06	0.002937	1	0.15927	3.3423	1.0176
24	0.13108	0.13057	0.13137	0.13101	1.11E-07	0.000333	0	-	-	-
25	0.13391	0.13412	0.13502	0.13435	2.31E-07	0.000481	0	-	-	-
26	0.11386	0.11703	0.11739	0.11609	2.52E-06	0.001588	1	0.11744	0.050872	1.0031
27	0.11519	0.11882	0.12038	0.11813	4.72E-06	0.002174	1	0.12157	1.2293	1.0132
28	0.03518	0.036638	0.037542	0.036453	9.47E-07	0.000973	1	0.039016	4.9103	1.0247
29	0.11466	0.11531	0.11522	0.11506	8.36E-08	0.000289	0	-	-	-
30	0.14353	0.14328	0.14264	0.14315	1.39E-07	0.000373	0	-	-	-
31	0.10201	0.10154	0.10023	0.10126	5.73E-07	0.000757	0	-	-	-
32	0.11056	0.11098	0.11121	0.11092	7.33E-08	0.000271	1	0.11151	0.3316	1.0021

APPENDIX VI

Sensitivity of flow depth, x-velocity, y-velocity, turbulent kinetic energy and rate of turbulent dissipation to number of parallel processing cores

Processing Cores	Flow Depth			X-Velocity			Y-Velocity			Turbulent Kinetic Energy			Rate of Turbulent Dissipation		
	M.E.	VAR	STD	M.E.	VAR	STD	M.E.	VAR	STD	M.E.	VAR	STD	M.E.	VAR	STD
	[m]	[m]	[m]	[m/s]	[m/s]	[m/s]	[m/s]	[m/s]	[m/s]	[m^2/s^2]	[m^2/s^2]	[m^2/s^2]	[m^2/s^3]	[m^2/s^3]	[m^2/s^3]
1	0	0	0	0	0	0	0	0	0	0	0	0	0	0	0
8	1.67E-06	6.26E-07	0.000792	-6.00E-06	2.96E-06	0.001721	-1.52E-05	5.29E-06	0.0023	1.67E-06	6.26E-07	0.000792	6.66E-07	4.35E-08	0.000209
24	2.16E-06	2.37E-07	0.000487	-1.05E-05	2.72E-06	0.00165	-1.18E-05	2.95E-06	0.001718	2.16E-06	2.37E-07	0.000487	-1.46E-07	2.63E-08	0.000162
36	7.17E-07	9.82E-08	0.000313	2.62E-06	1.86E-06	0.001364	3.87E-06	2.04E-06	0.001427	7.17E-07	9.82E-08	0.000313	-2.22E-07	2.22E-08	0.000149
60	1.68E-07	6.02E-08	0.000245	8.10E-07	2.50E-06	0.001582	2.92E-06	2.60E-06	0.001612	1.68E-07	6.02E-08	0.000245	-1.98E-07	1.50E-08	0.000122
120	2.73E-06	3.84E-07	0.00062	-1.17E-05	3.23E-06	0.001798	-1.62E-05	4.16E-06	0.002038	2.73E-06	3.84E-07	0.00062	2.08E-07	2.43E-08	0.000156